ISTANBUL TECHNICAL UNIVERSITY ★ GRADUATE SCHOOL

QUATERNARY TECTONIC AND CLIMATIC INTERACTIONS IN CENTRAL PONTIDES, TURKEY; INFERENCES FROM OSL AND COSMOGENIC APPLICATIONS ON FLUVIAL DEPOSITS

Ph.D. THESIS

Kevin P. MCCLAIN

Department of Climate and Marine Sciences

Earth System Sciences Programme

MARCH 2021

ISTANBUL TECHNICAL UNIVERSITY ★ GRADUATE SCHOOL

QUATERNARY TECTONIC AND CLIMATIC INTERACTIONS IN CENTRAL PONTIDES, TURKEY; INFERENCES FROM OSL AND COSMOGENIC APPLICATIONS ON FLUVIAL DEPOSITS

Ph.D. THESIS

Kevin P. MCCLAIN
(601142003)

Department of Climate and Marine Sciences

Earth System Sciences Programme

Thesis Advisor: Prof. Dr. Cengiz YILDIRIM
Thesis co-Advisor: Prof. Dr. Attila ÇİNER

MARCH 2021

İSTANBUL TEKNİK ÜNİVERSİTESİ ★ LİSANSÜSTÜ EĞİTİM ENSTİTÜSÜ

ORTA PONTİDLERDE KUVATERNER TEKTONİK VE İKLİMSEL ETKİLEŞİMİ: AKARSU ÇÖKELLERİNİN KOZMOJENİK VE OSL UYGULAMALARINDAN ÇIKARIMLAR

DOKTORA TEZİ

Kevin P. MCCLAIN
(601142003)

İklim ve Deniz Bilimleri Anabilim Dalı

Yer Sistem Bilimi Programı

Tez Danışmanı: Prof. Dr. Cengiz YILDIRIM
Eş Danışmanı: Prof. Dr. Attila ÇİNER

MART 2021

Kevin P. MCCLAIN, a Ph.D. student of ITÜ Graduate School, student ID 601142003, successfully defended the dissertation entitled "QUATERNARY TECTONIC AND CLIMATIC INTERACTIONS IN CENTRAL PONTIDES, TURKEY; INFERENCES FROM OSL AND COSMOGENIC APPLICATIONS ON FLUVIAL DEPOSITS", which he prepared after fulfilling the requirements specified in the associated legislations, before the jury whose signatures are below.

Thesis Advisor : **Prof. Dr. Cengiz YILDIRIM**
İstanbul Technical University

Thesis co-Advisor : **Prof. Dr. Tahsin Attila ÇİNER**
Istanbul Technical University

Jury Members : **Doç. Dr. Tolga GÖRÜM**
Istanbul Technical University

Prof. Dr. Tuncer DEMİR
Akdeniz University

Dr. Öğr. Üyesi Cengiz ZABCI
Istanbul Technical University

Prof. Dr. Faruk OCAKOĞLU
Osmangazi University

Prof. Dr. Hüseyin TUROĞLU
Istanbul University

Date of Submission : 12 January 2021
Date of Defense : 11 March 2021

To the technical, the talented, and those who seek truth, if you dare write a thesis, good luck to you,

FOREWORD

Thank you to my parents, Peggy MCCLAIN and James MCCLAIN, for their encouragement and forced homework before fun as a child. Thank you to my wife Nuray MCCLAIN for her support during this time-consuming endeavor. Thank you to her family, Hikmet UZUN and Mehmet Akif UZUN, for their continuous support here in Turkey.

From my many former colleagues to the ambitious people I met in Uppsala, I have been lucky to be surrounded by thought-provoking and encouraging people. I do not know whether thanking them for their encouragement or blaming them for sending me down a path of uncertainty is appropriate. "If *he* can do a PhD, you can do a PhD" are words that echo in my head to this day. I will be nice and say thanks. Writing a doctoral thesis is a luxury in a world where most cannot step foot in a university lecture hall and I am sure many people I have known and worked with in the past would have enjoyed such an opportunity.

Thank you to my supervisors Cengiz YILDIRIM and Attila ÇİNER for their guidance and patience. Older dogs learn new tricks eventually and I see landscapes and the scientific writing process much differently compared to when I arrived. Thank you to my friends at the Eurasia Institute of Earth Science for their good company and support navigating this adventure.

December 2020 Kevin P. MCCLAIN

TABLE OF CONTENTS

Page

ABBREVIATIONS

ALOS : Advanced Land Observing Satellite
AF : Alluvial Fan (on outcrop photos)
AF : Araç Fault (on maps)
BF : Bartın Fault
BLK : Bolkuş
B.R. : Bartın River
BsF : Black Sea Fault
CAP : Central Anatolian Plateau
CF : Cide Fault System
dGPS : Differential Global Positioning System
DEM : Digital Elevation Model
De.R. : Devrek River
DF : Devrek Fault
DSM : Digital Surface Model
EF : Ekinveren Fault
ENE : East-Northeast
ESE : East-Southeast
GPS : Global Positioning System
HF : Hydrofluoric Acid
IB : Ilgaz Basin
IR : Infrared Radiation
Kc.R. : Kozcağız River
KF : Karabük Fault
KaF : Karagöl Fault
LA : Landslide A
LB : Landslide B
LED : Light-Emitting Diodes
MTA : Turkish Directorate of Mineral Research and Exploration
NAF : North Anatolian Fault
OSL : Optically Stimulated Luminescence
R. : River
SAR : Single-Aliquot Regenerative Dose
SfM : Structure from Motion
T1-T7 : Terrace Level 1 through Terrace Level 7
TL : Thermoluminescence
ToB : Tosya Basin
WG : Wind Gap
WNW : West-Northwest
WSW : West-Southwest
UAV : Unmanned Aerial Vehicle
UTM : Universal Transverse Mercator
YF : Yığılca Fault

SYMBOLS

µm	: Micrometer
^{10}Be	: Beryllium-10
^{36}Cl	: Chlorine-36
^{90}Sr	: Strontium-90
^{90}Y	: Yttrium-90
cm	: Centimeters
De	: Equivalent Dose
Gy	: Absorbed Dose (joules) of Ionizing Radiation per Kilogram of Matter
Gy/ka	: Absorbed Dose of Ionizing Radiation per Thousand Years
Gy/s	: Gy per Second
H_2O_2	: Hydrogen Peroxide
HCl	: Hydrochloric Acid
i	: Dose
i = n	: Natural Dose
K	: Potassium
ka	: Thousand Years
km	: Kilometer
Li	: Luminescence Signal
m a.s.l.	: Meters above Sea Level
mm/a	: Millimeters per Year
Mw	: Moment Magnitude
mW cm^{-2}	: Metric Watts per Square Centimeter
nm	: Nanometer
ppm	: Parts per Million
Th	: Thorium
Ti	: OSL Signal
U	: Uranium
U	: Uplift Rate (in equation)
◦C	: Degrees Celcius
%	: Percentage
~	: Around/on the order of
±	: Plus and Minus

LIST OF TABLES

Page

LIST OF FIGURES

Page

QUATERNARY TECTONIC AND CLIMATIC INTERACTIONS IN CENTRAL PONTIDES, TURKEY; INFERENCES FROM OSL AND COSMOGENIC APPLICATIONS ON FLUVIAL DEPOSITS

SUMMARY

The fluvial incisional response to Cenozoic uplift has been widely studied, yielding insights on timing, patterns, and/or rates of rock uplift. Absolute dating of Quaternary landforms in actively uplifting regions can provide accurate rock uplift rates that after careful interpretation can be used to explain the processes that developed the landscape.

The Mediterranean region, or western half of the Alpine-Himalayan orogenic belt, is comprised of complex environments resulting from the convergence of the African and Arabian plates with Eurasia, subsequent trench retreats, and mantle processes (Wortel and Spakman, 2000). One of these environments is the Central Anatolian Plateau, which is an orogenic plateau between the contractional Eastern Anatolian Plateau and the Western Anatolian Extensional Province. While the uplift of the southern margin of the plateau has complex relationships with the lithospheric mantle and subduction along the Cyprus Trench, the northern margin is suggested to be decoupled from mantle processes of the plateau interior and southern margin. Instead, its uplift and lateral growth are mostly attributed to the development of the broad restraining bend of the North Anatolian Fault, a transform fault between the Anatolian microplate and Eurasian Plate. The environment between the restraining bend and Black Sea is also referred to as the Central Pontides and has been interpreted as a growing orogenic wedge with a positive flower structure geometry. However, the faults north of the restraining bend show weak modern seismicity, and their Quaternary activity is not fully understood at this time. Over the last decade marine terraces, delta terraces, and fluvial terraces have been used to calculate rock uplift rates in the eastern and central flanks of the Central Pontides, revealing a possible uplift rate increase with proximity to the North Anatolian Fault restraining bend. Marine terraces as far north as the Sinop Peninsula and a Mw 6.6 earthquake offshore on the western flank show a compressional tectonic regime extending into the Black Sea shelf.

On the western flank of the Central Pontides there are several main rivers incising the topography of the plateau margin en route to the Black Sea. The Filyos River is the largest of these and has the best known fluvial terrace record preserved, including a strath terrace staircase of seven levels on the hanging wall block of the Karabük Fault, a reverse fault verging towards the restraining bend. Here, the Filyos River incises through the Karabük Range, creating ~1700 m of relief in the Filyos River Gorge. The first part of the thesis focused on calculating rock uplift rates at this terrace staircase using the OSL method to date the deposition age of fluvial terraces. The bedrock incision rates revealed a glimpse of the highest uplift rates recorded in the Central Pontides, with uplift rates of 1.15 mm/a before 366 ± 19 ka. However, the younger terraces revealed a suspiciously low bedrock incision rate of just 0.12 mm/a during the

last 366 ka. The high incision rate period experienced two lateral channel migrations and an epigenetic gorge formation, suggesting the Filyos River is capable of eroding and transporting thick local aggradation. This means something other than local coseismic landslides would be required to prevent the river from reaching equilibrium and incising bedrock for long periods.

In the second part of the thesis, the environment downstream from the Filyos River Gorge was investigated. The areas with clastic bedrock tend to laterally erode enough to accommodate more aggradation and form fluvial terraces. With the exception of the terraces staircase upstream, the Filyos River Gorge has lithologies that restrict lateral mobility of the channel. Clastic lithologies reappear on the windward side of the Karabük Range, downstream from the Filyos River Gorge. Here, the remnants of three fill terrace levels are preserved, but mostly with poor conditions for OSL sampling. Luckily, at a main river-tributary junction stronger alluvial fan layers overly the lowest fill terrace level, helping to preserve it. OSL dating of a longitudinal bar layer revealed a fill terrace age of 275 ± 12.8 ka. Three well-rooted limestone boulders were sampled on the surface of the landform, revealing a maximum abandonment age of 39.5 ± 3.5 ka. Geomorphic interpretations of the main river valley and tributary catchments identified a large, previously unmapped landslide upstream from a limestone tributary canyon that the tributary incises through in its final kilometers. This landslide would have provided a sudden influx of sediment into the tributary, resulting in transport through the canyon and onto the main valley. This was confirmed in the alluvial fan layers on the opposite side of the valley. There is evidence of outburst floods in elevated fluvial ~35 m above the tributary channel between the landslide and tributary canyon.

The most recent fill terrace level at 275 ka formed during a hiatus of fluvial terrace formation upstream. Therefore, it is assumed that the aggragation during that period was not local to this valley segment and is instead the result of conditions in the larger catchment. The Filyos River may not have the ability to efficiently remove such catchment-wide aggradation, especially in cooler climatic periods when precipitation rates are reduced. With the local environment occurring in the more landslide-prone windward side of the Central Pontides, it is also possible that new base levels form due to fill terrace formation, disturbing preventing continuous bedrock incision upstream. The main river-tributary junction fan would have formed such a base level but is less likely to interrupt incision on significant scales. Therefore, the results show the importance of comparing rock uplift rates of fluvial terraces to rates and interpretations of downstream fill terraces. Upstream in the Filyos River Valley strath terrace staircase, the lower 0.12 mm/a bedrock incision rates since 366 ± 19 most likely significantly underestimate the rock uplift rates, meaning the rock uplift rates of the Karabük Range are on the order of 1.15 mm/a.

Collectively, the results show that the strain directed at the western flank of the Central Pontides by the North Anatolian Fault restraining bend produces the highest measured Central Pontides rock uplift rates. These first rock uplift rates on the western flank support the model of a growing orogenic wedge with a positive flower structure. The results also show the sensitivity of the hillslopes to fail and produce catastrophic landslides that form landslide dams, alluvial fans at river junctions, and cause channels to migrate to new positions through the formation of epigenetic gorges. This could have consequences for populations living near the Filyos River and other main rivers incising clastic bedrock.

ORTA PONTİDLERDE KUVATERNER TEKTONİK VE İKLİMSEL ETKİLEŞİMİ: AKARSU ÇÖKELLERİNİN KOZMOJENİK VE OSL UYGULAMALARINDAN ÇIKARIMLAR

ÖZET

Senozoyik dönem yükselimine karşı akarsuların derine kazma tepkileri yaygın bir şekilde çalışmış ve kaya yükseliminin zamanlaması, deseni ve/veya hızları ile ilgili bilgi sağlanmıştır. Aktif olarak yükselen bölgelerdeki Kuvaterner yerşekillerinin mutlak yaşlandırılması dikkatli değerlendirmelerden sonra doğru kaya yükselim hızlarını hesaplamaya katkı sağlar ve sahanın topoğrafyasın oluşturan süreçleri açıklamada kullanılabilir.

Akdeniz bölgesi, ya da Alp-Himalaya Dağ Kuşağının batı yarısı, Avrasya ile Afrika ve Arab levhaları arasındaki yaklaşımı takip eden hendek gerilemesi ve manto süreçleri gibi karışık ortamların oluşmasıyla sonlanmıştır (Wortel ve Spakman, 2000). Bu ortamlardan biri Doğu Anadolu Daralma Bölgesi ile Batı Anadolu Genişleme Bölgesi arasında bir orojenik İç Anadolu Platosudur. Platonun güney kenarının yükselimi litosferik manto ve Kıbrıs Yayı arasındaki karmaşık ilişkinin bir sonucu olarak olurken kuzey kenarı plato içindeki ve güney kenardaki manto süreçlerinden bağımsızdır.

Bunun yerine, kuzey kenarın yükselimi ve gelişimi Anadolu mikro levhası ile Avrasya levhası arasında bir transform faya karşılık gelen Kuzey Anadolu Fayı'nın geniş sıkışmalı büklümü ile ilişkilendirilmiştir. Bu sıkışmalı büklüm ve Karadeniz arasında kalan bölge Orta Pontidler olarak adlandırılmış ve pozitif çiçek yapısı şeklinde gelişen bir orjenik kama yapısı olarak değerlendirilmiştir. Bununla beraber, sıkışmalı büklümün kuzeyindeki faylar düşük bir güncel depremsellik göstermekte ve bunların Kuvaterner aktivitesi tam olarak anlaşılmış değildir. Son on yılda, denizel sekiler, delta sekileri ve akarsu sekileri Orta Pontidlerin doğu ve orta kanatlarının kaya yükselim hızlarını hesaplamak için kullanılmış ve Kuzey Anadolu Fayı'na yakınlığına bağlı olarak yükselim hızlarının arttığı ortaya konmuştur. Sinop Yarımadası'ndaki yükselmiş denizel taraçalar ve Orta Pontidlerin batı kanadında gerçekleşen büyüklüğü Mw:6.6. olan Bartın Depremi dışmerkezinin deniz içinde olması sıkışma rejiminin Karadeniz'in kıta sahanlığına kadar ulaştığını göstermektedir.

Orta Pontidlerin batı kanadında bir çok akarsu plato kenarını aşarak Karadenize akmaktadır. Filyos Nehri bunların en büyükleridir ve çok iyi korunmuş ana sekilerinin varlığı ile bilinmektedir. Bu sekiler ters bir fay olan Karabük Fayı'nın yükselen bloğunda yedi seviye şeklinde gözlenir. Filyos Nehri Karabük Dağlarını keserek yaklaşık 1700 m derinliğinde bir rölyef oluşturur. Bu tezin ilk bölümü bu seki seviyelerinin OSL yöntemi ile yaşlandırılarak kaya yükselim hızlarını hesaplamaya yöneliktir. Elde ettiğimiz akarsuyun derine kazma hızları 1.15 mm/yıl (366±19 binyıl öncesinde) Orta Pontidler'de elde edilen en yüksek yükselim hızları olarak karşımıza çıkmaktadır. Bununla beraber genç sekiler son 366 bin yılda kuşku uyandıracak seviyede düşük 0.12 mm/yıl gibi derine kazma hızları vermektedir. Yüksek derine kayma hızlarına karşılık gelen dönem akarsu kanalının yana göç ettiği ve epijenetik

boğaz oluşumuna karşılık gelmekte ve Filyos Nehri'nin yerel ve kalın akarsu çökellerini taşıma ve aşındırma kabiliyetini göstermektedir. Bu durum yerel kosismik heyelanlardan başka nehrin dengeye ulaşmasını ve anakayayı uzun dönemler derine kazmasını engellemesini gerektirmektedir.

Tezin ikinci bölümünde, Filyos Nehri boğazının aşağı çığırı çalışılmıştır. Burada klastik anakayadan oluşan yamaçlar akarsu sekilerinin ve birikimin oluşmasına imkan veren yana doğru aşınmaya müsait ortam oluşturmaktadır. Yukarı çığırdaki sekiler dışında, Filyos Nehri Boğazı akarsu kanalının yanal hareketini sınırlayan litolojilerden oluşur. Klastik kayaçlar, Karabük Dağları'nın nemli tarafında Filyos Nehri Boğazı'nın aşağı çığırında tekrar ortaya çıkar. Bu kesimde, üç dolgu sekisi seviyesinin kalıntıları iyi korunmuş ancak OSL örneklemesi için oldukça zayıftır. Filyos Nehri'nin ana kollarından birinden kaynaklanan birikinti yelpazesi katmanları en alt dolgu sekisi seviyesinin korunmasına imkan vermiştir.

OSL yaşları bu dolgu sekisinin yaşını 275±12.8 bin yıl oarak vermiştir. Bununla beraber bu sekinin yüzeyine iyice yerleşmiş üç büyük kireçtaşı bloğundan aldığımız kozmojenik yaşlandırma örnekleri bu yüzeyin 39.5 ± 3.5 bin yıl önce terkedildiğini göstermektedir. Ana akarsu vadisinin ve kollarının havzalarının jeomorfik değerlendirmesi sonucu daha önce haritalanmamış bir heyelan kütlesinin belirlenmesime imkan vermiştir. Bu heyelan yan kolda hızlı bir çökel girdisine sebeb olmuş ve bu çökel ana vadiye kadar taşınmıştır. Ana vadinin karşı yamacındaki birikinti yelpazeleri katmanları içinde bunların bulunması bu sürecin bir kanıtıdır. Heyelanın gerisinde biriken suların oluşturduğu taşkının kanıtları yan kolun ~35 m yukarısında heyelan ve yan kol kanyonu arasında görülmektedir.

En genç dolgu sekisi seviyesi yaklaşık 275 bin yıl önce yukarı çığırda akarsu sekisi oluşumu sırasındaki bir zaman aralığında oluşmuştur. Bu yüzden bu dönemdeki birikimin sonucu yerel değil daha geniş alanları etkilemiştir. Filyos Nehri bu tarz havza boyutundaki birikimi özellikle iklimin soğuk ancak yağışın az olduğu iklim dönemlerinde biriken malzemeyi etkili birşekilde ortadan kaldırak güçte olmayabilir. Orta Pontidler'in nemli tarafındaki heyelan yoğun alanların bulunduğu ortamlarla birlikte dolgu sekisi oluşumları özellikle yukarı çığırdaki akasuların yataklarındaki anakayanın devamlı olarak derine kazılmasını yavaşlatır ya da engeller. Özellikle ana akarsu ile yan kolların çatakları bir çeşit yere taban seviyesi oluşturması derine kazmayı büyük ölçeklerde kesintiye uğratması düşük olasılıklıdır. Bu yüzden sonuçlar kaya yükselim hızlarının aşağı çığırdaki dolgu sekilerinin oluşum zamanları ile karşılaştırılmasının önemini göstermektedir. Filyos Nehri'nin Karabük Dağları içindeki boğazda son 366±19 bin yıl için hesapladığımız 0.12 mm/yıl gibi düşük derine kazma hızı aslında büyük oranda gerçeği yansıtmamakta buradaki yükselimi hızı daha 1.15 mm/yıl gibi bir seviyede olmalıdır.

Tüm bu sonuçlara baktığımızda Kuzey Anadolu Fayı'nın sıkışmalı büklümünün Orta Pontidlerin batı kanadına yüklediği yamulma Orta Pontidler'deki en yüksek kaya yükselim hızlarının oluşmasına sebep olmaktadır. Batı kanattaki bu kaya yükselim hızları Orta Pontidler'in bir pozitif çiçek yapısı ile orojenik kama şeklinde gelişimi ile uyumludur. Sonuçlar aynı zamanda yamaçların kütle harekelerine duyarlılığını ve heyelan sed gölleri oluşturmak için katastrofik heyelan oluşumlarının, akarsu çataklarındaki birikinti yelpazelerinin akarsu kanallarının yerinin değişmesine ve epijenetik boğaz oluşumuna neden olmaktadır. Bu durum Filyos Nehri boyunca yaşayan insanların hayatlarında sonuçları olacaktır.

1. INTRODUCTION

The western flank of the North Anatolian Fault's restraining bend coincides with one of the most enigmatic parts of the northern margin of the Central Anatolian Plateau (CAP) in terms of mode, mechanism, timing, and rate of the neotectonic deformations. Yıldırım et al. (2011) demonstrated that the large ~250-km-long restraining bend of the North Anatolian Fault (NAF) has generated regional transpression and offers a unique tectonic setting to investigate how strain is partitioned along a transform boundary and growing plateau margin. The northern margin of the CAP is interpreted as an active transpressional orogenic wedge with a positive flower structure between the NAF's restraining bend and the Black Sea Basin (Yıldırım et al., 2011). Here, the activity of the NAF, local tectonics, and lateral growth of the plateau margin appear closely related in the central and eastern flank of the northern margin (Berndt et al., 2018; Yıldırım et al., 2011).

Nevertheless, the only instrumental large earthquake with surface deformation occurred at the offshore part of the western flank. The Bartın Earthquake in 1968 (Mw 6.6) coseismically uplifted the shoreline between 0.3 and 0.4 m (Ketin & Abdüsselamoğlu, 1969; Wedding, 1969) as a result of offshore thrust faulting (Alptekin et al., 1986; McKenzie, 1972) indicating active deformation away from the NAF and invokes the necessity of region-wide tectonogeomorphic investigations along the western flank. However, our knowledge about the onshore western flank is very limited because of the erosional characteristic of the landscape and dearth of the Late Cenozoic units that do not help to quantify regional deformations. Fortunately, in terrestrial areas of tectonically active regions, fluvial strath terraces are common landforms. These thin layers of sediment overlying planar bedrock represent paleo-floodplains or paleo-base levels (Bull, 1991; Merritts et al., 1994). When the base levels are lowered due to vertical tectonic deformation, terrace abandonment ages and their incision rates can be used as precise proxies for regional rock uplift rates or slip rates of individual faults on time scales spanning the Quaternary (Maddy et al., 2008; Pazzaglia, 2013; Schildgen et al., 2012a; Whittaker et al., 2008).

In actively deforming orogenic plateau margins, the occurrence of higher humidity and lithologies prone to landslides can complicate the responses of rivers to tectonically driven processes (e.g. rock uplift). Landslides occurring along the trunks or tributaries of river networks provide extra sediment inputs into the rivers that may form constrictions or dams, changing the upstream river behavior from incision to deposition (Hewitt, 1998, 2006). In tributaries, landslides of sufficient size may also contribute material into the fluvial system that is transported downstream and deposited as an alluvial fan (Leopold et al., 1964). Alluvial fans at tributary-main river junctions are common in mountainous areas with high sediment supply and are often associated with V-shaped, non-glaciated valleys in regions of active tectonic uplift (Stokes and Mather, 2015). The dynamics of tributary-junction alluvial fans are an added complexity for the main channel that is not fully understood, possibly due to a wide range of outcomes possible in nature, limited laboratory experiment outcomes, and the erosional response of main rivers to sedimentary layers associated with such alluvial fans (Savi et al., 2020). These phenomena (landslide dams and alluvial fans) create a temporary local base level. In the case of tributary junction alluvial fans, if the fan progrades to block the main channel, the new local base level of the main river experiences a decrease in sediment mobility and deposition upstream from the fan, while a prolonged blockage may cause channel slope adjustments that propagate upstream (Savi et al., 2020). The spatial scale of this kind of intervention might be very local, but if prolonged it may influence the rate of incision and/or deposition of rivers at greater distances along the channel's reach. Lowering of base levels following the incisional response of rivers to uplift allow dated fluvial terraces (usually strath terraces) to estimate a bedrock incision rate that may be used as a proxy for regional rock uplift rates (Maddy et al., 2008; Schildgen et al., 2012a; Pazzaglia, 2013; Stokes et al., 2017). Therefore, it is crucial to exclude the influence of such surface processes on river incision for accurate quantification of the amount and rate of regional rock uplift. This region is one of the most landslide-prone areas of Turkey (Duman et al., 2005; Görüm, 2019; http://yerbilimleri.mta.gov.tr/anasayfa.aspx) and has numerous deeply incised bedrock-walled gorges in main valleys and tributaries. The combination of higher humidity, intense landslide activity, deep incision, and higher strain accumulation make this area a natural laboratory to investigate the interactions between surface and tectonic processes across a growing margin of an orogenic plateau.

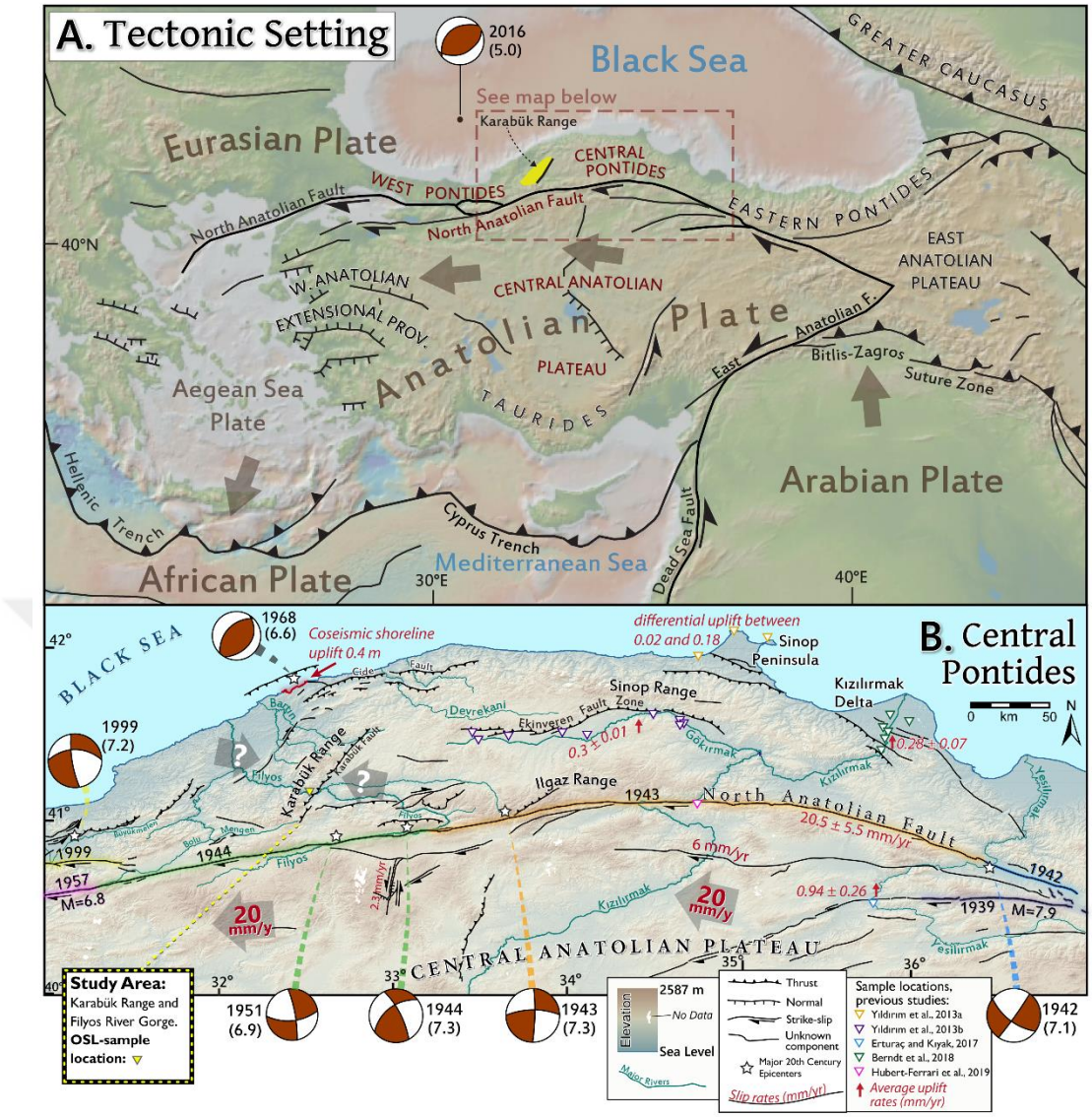

Figure 1.1 : (a.) The tectonic setting of Anatolia, with the study area shaded in yellow. Map was modified from the GeoMapApp. The Black Sea focal mechanism is based on Önal and Demirbağ (2019). (b.) A shaded topographic map illustrating the tectonics of the Central Pontides. The location of the OSL-dating site in the Karabük Range is marked by a yellow triangle. Study sites from previous studies using Quaternary dating to infer rock uplift rates are marked with triangles. North Anatolian Fault focal mechanisms and magnitudes are based on Şengör et al. (2005). The 1968 Black Sea earthquake focal mechanism is based on Tari et al. (2000).

1.1 Literature Review

Much of Anatolia's geologic history occurred during the closure of the Tethys oceans between the Cretaceous and Cenozoic (Şengör and Yılmaz, 1981; Yılmaz et al., 1997; Okay and Tüysüz, 1999; Dilek, 2006; Sosson et al, 2010). A major Tethyan ocean subducted northward under the Pontides during late Cretaceous, leading to a back-arc basin that formed the Black Sea, eventually separating the Pontides from Eurasia

(Şengör and Yılmaz, 1981; Okay et al., 1994; Yılmaz et al., 1997; Okay et al., 2006). The northward convex-shaped geometry of the Central Pontides may originate from oroclinal bending caused by closure of the Neo-Tethys Ocean between the Pontides and Anatolide-Tauride Block from the Cretaceous through the start of Paleocene (Meijers et al., 2010). Subsequent post-collisional deformation resulted in a thin-skinned fold and thrust belt (Okay and Tüysüz, 1999). The major compressive deformation in the Pontides occurred through the Eocene, which uplifted the region and formed a continental area persisting through the present (Hippolyte et al., 2016).

The Central Anatolian Plateau is an orogenic plateau between the contractional Eastern Anatolian Plateau and the Western Anatolian Extensional Province (Figure 1.1) (McKenzie, 1972, 1978; Dewey and Şengör, 1979; Jackson and McKenzie, 1984; Dewey et al.,1986; Barka and Reilinger, 1997; Reilinger et al., 1997, 2006; Platzman et al., 1998; Schildgen et al., 2012b; Schildgen et al., 2014; Göğüş et al., 2017). To the east, contraction, and uplift of the Eastern Anatolian Plateau is the result of subduction of the Arabian plate with average surface elevations of ~2 km enabled by a hot mantle and absence of mantle lithosphere (Şengör and Yılmaz, 1981; Şengör et al., 2003; Allen et al., 2004). To the west, the Western Anatolian Extensional Province is part of the backarc extension of mainland Greece and the Aegean Sea, driven by the southwestward trench retreat of the subducting African slab (Le Pichon and Angelier, 1979; Jolivet et al., 2013). The Central Anatolian Plateau's complexity results from its development in connection with these neighboring environments.

The Central Anatolian Plateau began uplifting and experiencing volcanism no earlier than ~11 Ma (Aydar et al., 2013; Meijers et al., 2018). Many models have been proposed to explain how the plateau uplifted and sustained its elevation, including crustal thickening (Piper et al., 2006), delamination (Bartol and Govers, 2014), lithospheric drip (Göğüş et al., 2017), and slab tear (Schildgen et al., 2014, Abgarmi et al., 2017). Nevertheless, underlying the present-day Central Anatolia Plateau surface there are generally slow uppermost mantle seismic velocities and high heat flow (Reid et al., 2017 and references therein). The interior of the plateau is mostly low-relief, semiarid highlands, with a mean elevation of ~1 km and increased topographic relief at the northern and southern margins (Cosentino et al., 2012; Schildgen et al., 2014; Çiner et al., 2015). In the plateau interior, 100 m of uplift since 2 Ma yielded a mean uplift rate of 0.05 ± 0.01 mm/a since 2 Ma (Çiner et al., 2015).

This was preceded by a more rapid long-term uplift rate of 0.12 mm/yr between 5 and 2.5 Ma (Aydar et al., 2012). The southern plateau margin, or Taurides, has conflicting data explaining the timing and mechanisms of uplift. Longitudinal profiles and ages of fluvial terraces and marine layers suggest a late Miocene to present uplift. A ~2 km record of uplift since ~8 Ma yielded uplift rates of ~0.25 mm/a (Cosentino et al., 2012). A 1.2 to 1.5 km uplift starting between 8 and 5.45 Ma yielded uplift rates of 0.1 to 0.2 mm/a before 1.6 Myr, followed by an acceleration to 0.6 to 0.7 mm/a (Schildgen et al., 2012a). Öğretmen et al., (2018) also found rapid Pleistocene uplift, with 1.5 km uplifted in the last 0.45 Ma at a rate of 3.2 to 3.4 mm/a. Sub-horizontal bedding observed in the southern margin may be a result of an ephirogenic uplift pattern, meaning this multiphased late Miocene uplift followed by more rapid Pleistocene to present uplift could result from slab breakoff and an ensuing asthenospheric mantle upwelling (Cosentino et al., 2012; Schildgen et al., 2012a, 2012b, 2014; Abgarmi et al., 2017; Öğretmen et al., 2018) However, before the Pliocene, the southern margin may have been uplifted by shortening and thickening from Eurasian-African compression (Koç et al., 2017; Meijers et al., 2018; Fernandez-Blanco et al., 2019), while a rain shadow inferring uplift was detected by Pliocene (Meijers et al., 2018).

Along the northern margin of the Central Anatolian Plateau, which will mostly be referred to as the Central Pontides, the neotectonic environment is much different. The Central Pontides are the convex-shaped landmass of mostly mountainous topography and high local relief between the Black Sea and the North Anatolian Fault (Okay & Tüysüz, 1999). To its north is the Black Sea, an oceanic basin that developed as a result of back-arc extension related to the subduction of the Tethyan plate during the Mesozoic (Okay et al., 1994). The central and eastern parts of the southern margin of the Black Sea are currently under the compression (Barka & Reilinger, 1997; Finetti et al., 1988; Şengör & Kidd, 1979). The North Anatolian Fault, a 1,200-km-long transform fault stretching from eastern Turkey to the northern Aegean Sea, is the major active structure within the Central Pontides (Ketin, 1948; Şengör et al., 2005). It defines the northern boundary of the Anatolian microplate and accommodates its westward motion between the collision in the east and subduction in the west (Andrieux et al., 1995; Dewey & Şengör, 1979; Kaymakçı et al., 2003; Şengör & Yılmaz, 1981; Şengör et al., 2012). The convex-shaped restraining bend of the North Anatolian Fault strikes nearly parallel to the convex-shaped Black Sea coastline.

Modern strain was quantified along the North Anatolian Fault, with a geodetic fault parallel slip rate of 24 ± 1 m/a (Figure 1.1) (Reilinger et al., 2006). Plate kinematic analyses revealed that the fault-parallel slip rate varies minimally but fault-normal velocities increase up to 7 mm/a starting from the apex of the restraining bend (Yıldırımet al., 2011).

Within the Central Pontides three mountain subranges were formed; the Ilgaz Range, a push-up structure running east-west along the north side of the NAF; the Sinop Range, another push-up structure running mostly parallel to the Ilgaz Range and the Black Sea coast (Yıldırım et al., 2013a); and the Karabük Range, a more linear SSW-NNE running range on the western flank of the Central Pontides (Figures 1.1 and 1.2). The Ilgaz and Sinop Ranges trend nearly parallel to the direction of compressional strain from the restraining bend of the NAF and are likely a result of a growing detached positive flower structure (Yıldırım et al., 2011).

Shortening structures and shortening as a mechanism for uplift were reported at the Sinop Peninsula, in the Görkırmak Basin, and along the NAF and Kızılırmak Delta (Berndt et al., 2018; Ellero et al., 2015; Hippolyte et al., 2016; Yıldırım et al., 2011; Yıldırım et al., 2013b; Yıldırım et al., 2013a). Thrust faults occur dipping away from the Black Sea Basin (Finetti et al., 1988; Yıldırım et al., 2011; Yıldırım, et al., 2013b), and several other active thrust faults are present dipping away from the NAF restraining bend, such as the Ekinveren and Karabük faults (Yıldırım, et al., 2013b) (Figure 1.1b).

Quaternary uplift rates, topography, and fault geometry on the eastern flank between the Ilgaz Range and Sinop Peninsula support the large-scale detached positive flower structure model. However, the same model for the western flank is less easily discernable by neotectonic surface features, with the exceptions of the Karabük Fault, Cide Fault System, and Bartın Fault. The Cide Faults are inherited low-angle thrusts and reverse faults with Late Eocene to Early Miocene deformation and unknown Quaternary activity (Sunal & Tüysüz, 2002). Ellero et al. (2015) examined the neotectonics and history of deformation along the NAF near the southeast of the Karabük Fault (Figure 1.1b). They concluded the present-day NAF formed within the southern parts of a 30-km-wide shear zone, where many parallel to subparallel transpressional structures formed, including the active Araç Fault (dextral). A recent study (Bengü, 2017) produced a model from immediately west of the Ellero et al.

(2015) study area, identifying the Karagöl Fault along the northern part of the NAF shear zone. The model was developed between the NAF and Black Sea based on paleostress analyses of several faults, including the Karabük Fault and Bartın Fault, which is a dextral strike-slip fault with a reverse component located on the windward side of the Karabük Range (Bengü, 2017).

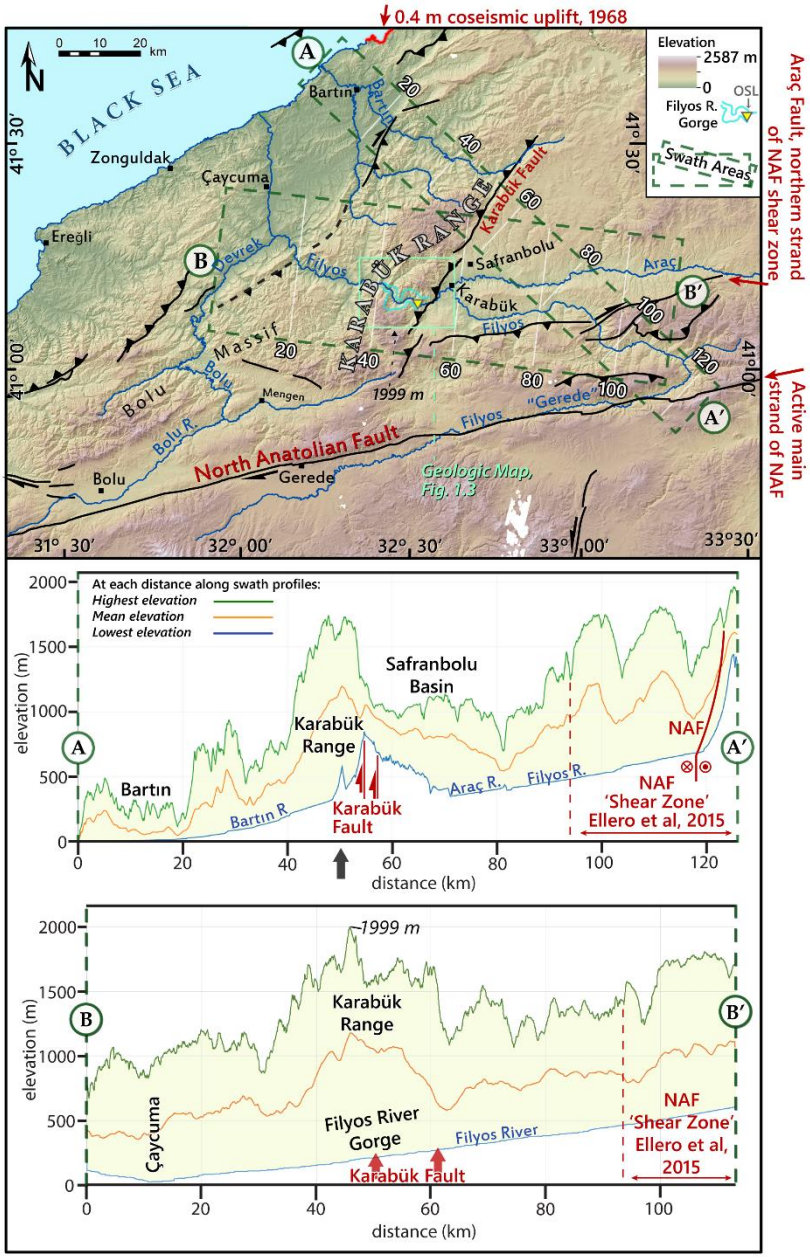

Figure 1.2 : Topographic map illustrating the location of the Karabük Range, faults, and main rivers of the western flank of the Central Pontides. Dashed rectangles outline the swath profiles illustrated below the map. Topography was generated from the ALOS-2 DSM.

A majority of the modern seismicity of the Central Pontides occurs along the NAF. The 1943 Tosya Earthquake (Mw 7.6) and the 1944 Bolu-Gerede Earthquake (Mw

7.5) are the largest two events that occurred on the NAF within the study area. The epicenter of these earthquakes are both located on the western flank of the restraining bend. More seismic evidence of compression on the western flank was observed 6 km off the Black Sea coast in 1968 when a shallow (4-km depth) Mw 6.6 earthquake occurred with a thrust focal mechanism (Figure 1.1b) (Alptekin et al., 1986). Coastal areas near the town of Amasra initially recorded 35 to 40 cm of coseismic uplift (Ketin & Abdüsselamoğlu, 1969; Kuşçu et al., 2004). Seismic profiles offshore from Amasra and the Filyos River were performed by the Turkish Directorate of Mineral Research and Exploration (Turkish MTA) in 1998 and interpreted by Damcı et al. (2004). The location of an imbricate structure interpreted as reverse faults, aligned with the hypocenter of the Bartın 1968 earthquake (Damcı et al., 2004). Farther offshore to the WNW, a magnitude 5.0 earthquake with a thrust focal mechanism (Önal & Demirbağ, 2019) occurred in 2016 as a result of ongoing regional deformation (Figure 1.1a).

The Karabük Range is one of the three major subranges within the Central Pontides. All three Central Pontides subranges have an asymmetric topography, tilted toward the Black Sea (Yıldırım et al., 2011). The crests of the ranges are closer to the NAF-facing flanks, which are steeper than the Black Sea-facing flanks. On the Central Pontides' western flank, the relief generated at the steepened front of the Karabük Range along the Karabük Fault is the greatest onshore evidence of vertical tectonic deformation north of the NAF Zone (Figures 1.2 and 1.3). The Karabük Fault is an inherited system of reverse faults from Late Eocene to Early Miocene, which were reactivated as an oblique-slip reverse fault during the Pliocene (Ayhan & Koçyiğit, 2010; Koçyiğit, 1987). The uplift rates on either side of the fault are unknown while unpublished GPS records suggest a ~4 mm/a slip rate (as cited in Ayhan & Koçyiğit, 2010). The range front includes a gentler-sloping pediment surface in the first 2 km of the footwall, where tilted bedrock is warped near the fault. The pediment bedrock surface is composed of Eocene clastics and carbonate units, which are overlain by loosely consolidated Plio-Quaternary alluvium (Figure 1.3) (Koçyiğit, 1987; Timur & Aksay, 2002). The hanging wall of the Karabük Fault is composed of a Neoproterozoic basement of granitoid and metamorphic units in the southwest (Okay et al., 1996; Akdoğan et al., 2017).

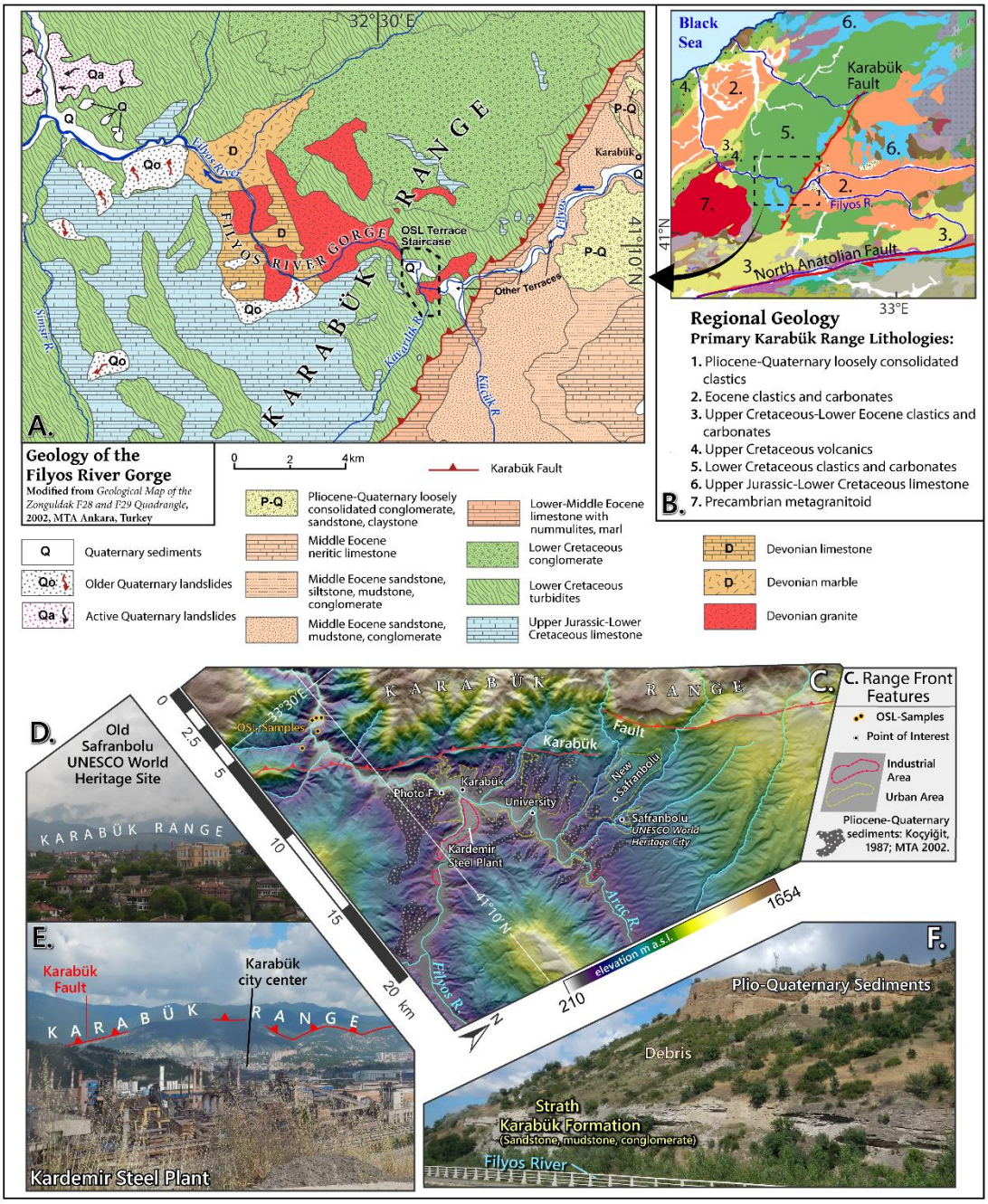

Figure 1.3 : (a.) Modified geologic map of the study area. (b.) Simplified geologic map of the western flank of the Central Pontides. (c.) Topographic map of the range front of the Karabük Range. (d.) and (e.) Photos of key cultural and economic sites facing towards the range front, with locations marked on map C. (f.) Pliocene-Quaternary alluvial sediments supplied by the range front and deposited on the footwall of the Karabük Fault.

The remaining main hanging wall units are Paleozoic. Late Jurassic-early Cretaceous platform carbonates are exposed near the fault in two locations (Akdoğan et al., 2017; Ellero et al., 2015; Tüysüz, 1999). These carbonates are unconformably overlain by a large late Cretaceous turbidites fan complex, which comprises a majority of the

hanging wall. This unit is primarily intercalations of sandstone and shale. Our study area has an increased percentage of shale compared to other sections of this unit in the east (Akdoğan et al., 2017). Because these units are turbidity currents composed of debris flows, Akdoğan et al. (2017) denoted that the turbidite clasts originating primarily from late Jurassic to early Cretaceous sometimes occur as limestone blocks that measure up to several kilometers wide.

The Karabük Range has a humid maritime climate with annual precipitation greater than 1200 mm/a in high elevations, while areas immediately ESE of the range are more continental and experience precipitation rates less than 760 mm/a (Göktürk et al., 2011). This combination of precipitation, tectonic activity, and topographic relief causes valleys to be prone to major hillslope failures and flood events. A study by Ercanoğlu and Gökçeoğlu (2002) created a medium-scale map of the clastic units of the study area and classified 53% of the land area as highly and very highly susceptible to landslides, whilst a later study demonstrated that precipitation is the primary trigger of modern landslides (Ercanoğlu et al., 2016).

The Filyos River, the main river of the study area, has headwaters ~20 km south of the NAF. Before the development of the NAF, the river flowed northward across the fault, then towards the Black Sea. However, over time the valley has been offset 70 km by the NAF (Yıldırım et al., 2011), causing it to flow eastward and increasing the catchment size. After reaching the eastern offset, the Filyos River turns northward then flows generally WNW for 90 km, after which it transverses the Karabük Fault and the uplifting Karabük Range by incising the Filyos River Gorge.

On the Karabük Fault footwall, the Filyos and Araç Rivers converge on Eocene clastic and carbonate units before flowing across the Karabük Fault and through the Karabük Range via the deeply incised, 19-km-long Filyos River Gorge (Figure 1.3). In this mostly bedrock-walled gorge, ~1,700 m of relief is generated between the highest peak of the Karabük Range and the Filyos River (Figure 1.2). It is here the Filyos River laterally erodes an area of turbidite units and forms a staircase of fluvial terraces, which are the focus of this study. Beginning 2 km upstream from Karabük's city center and continuing downstream until near proposed fault locations in Figure 1.2's map, fluvial strath terraces formed along most stretches of the Filyos River Valley. However, the start of the Filyos River Gorge on the hanging wall block of a reverse fault is where the largest vertical record of terraces is preserved. The first part of the thesis (cite the

sections here) uses this terrace staircase in the Filyos River Gore to calculate Quaternary rock uplift rates.

Downstream from the Filyos River Gorge, the valley experiences increased aggradation. These next 34 km of the Filyos River can be defined by a highly variable floodplain width that appears lithologically controlled due to the wider valley floor over clastic bedrock and narrower valley floor over or near bedrock of granitoid or limestones. Areas of wide floodplains are on the order of 100 to 1000 m in width and accommodate depositional features, including multiple fluvial terrace levels. These wider floodplain segments are interrupted by narrow valley floor segments that range between 30 to 100 m in width. The floodplains in these narrow segments are either restricted in size or non-existent, and fluvial terraces never form.

The second part of this thesis (cite the sections here) focuses on the first 6 km-long widened segment of the Filyos River Valley, downstream from the main gorge on the humid windward side of the Karabük Range. Here, the Şimşir River tributary flows northward and connects with the main river 5 km downstream from the main gorge and 71 km from the mouth in the Black Sea. This tributary catchment covers 122 km2, with its headwaters in the southern part of the Karabük Range on the uplifting hanging wall block of the Karabük Fault (Figure 1.3). The tributary catchment is densely vegetated and has relatively higher stream power compared to nearby catchments of similar size. Although the tributary catchment is comprised of primarily turbidites and limestone, it ends with a 2 km-long limestone-walled canyon (Şeker Canyon) before meeting the main river. The valley segment between the main gorge and the tributary junction has preserved fluvial terraces and alluvial fan layers of local sources that result from being the first depositional area downstream from areas of deepest incision and relief in the western flank of the Central Pontides. Hillslope processes in the tributary catchment appear to cause sediment flux increases into the main valley and the formation of temporary tributary junction alluvial fans. Glaciations are absent in the greater Filyos River catchment, including all tributaries, and there is no recent volcanism in the Central Pontides. This means hillslope processes and flooding are dominant controls on aggradation, terrace formation, and landforms that may block channels while base-level changes are limited to sea level variation and the local

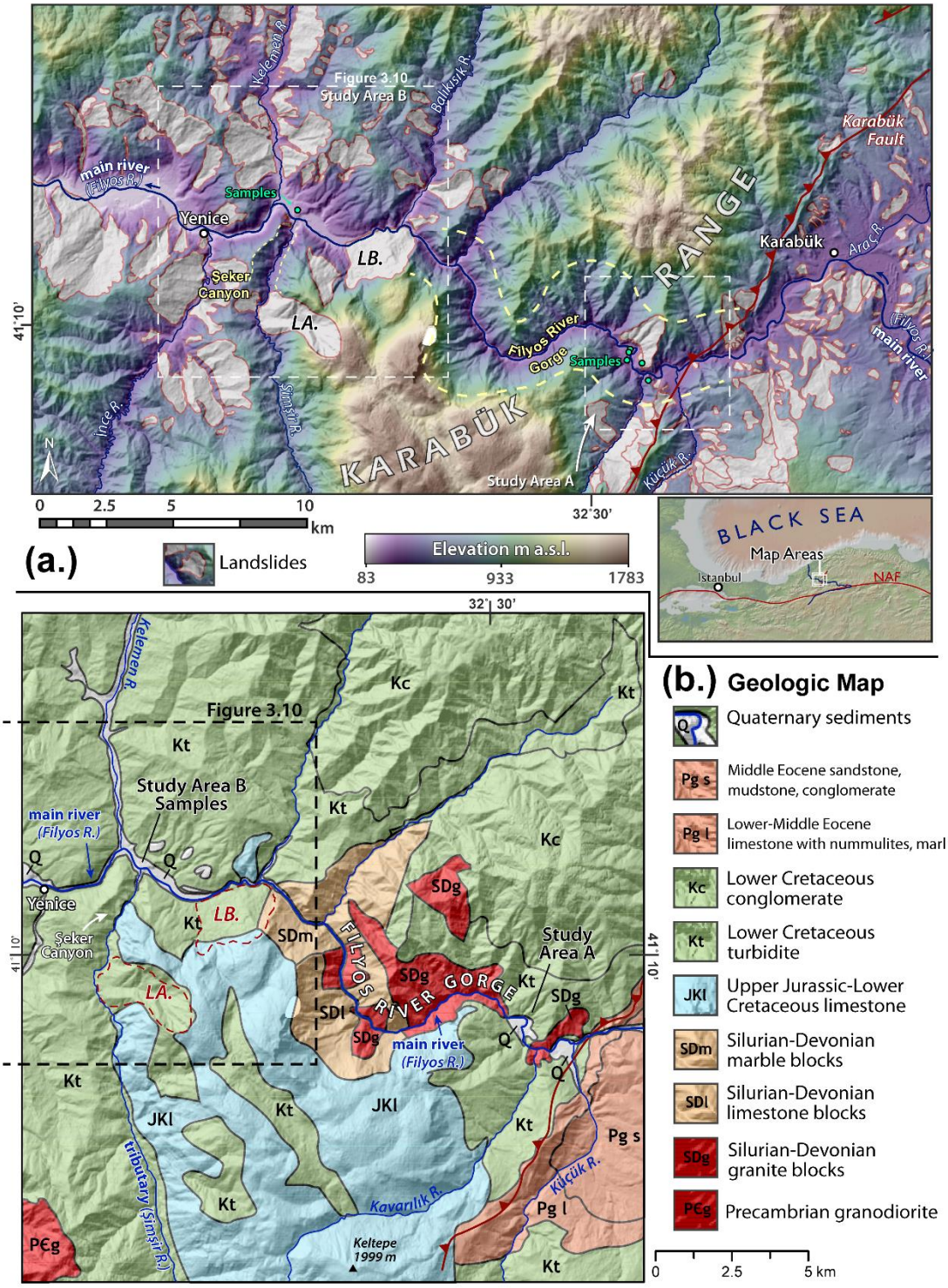

Figure 1.4 : (a.) Topographic map showing the downstream area of the Filyos River and Study Area B. The main river flows westward onto the Karabük Fault hanging wall, through the Filyos River Gorge, then through the windward side of the topography. Labels LA and LB are locations of landslides that potentially supplied sediment overlying the valley's fill terrace layers. Landslides were digitized from Duman et al. (2011). (b.) A modified geologic map including downstream areas of Study Area B based on Timur and Aksay (2002) and Aslan and Aksay (2002).

effects of aggradation. From here forward the Filyos River and Şimşir River will be referred to as the main river and tributary respectively, as much of the study will focus on this tributary junction and their respective channels, valleys, and catchments.

1.2 Hypothesis

From the middle Miocene (Serravallian) to present, two large-scale developments have greatly influenced the evolution of Anatolia: the westward propagation of the NAF (Dewey et al., 1986; Şengör et al., 2005) and the lateral growth and uplift of the Central Anatolian Plateau (Yıldırım et al., 2011; Yıldırım et al., 2013b; Yıldırım, et al., 2013a). Along the northern margin of the Central Anatolian Plateau, the North Anatolian Fault restraining bend causes transpression while further west in the region of the Marmara Sea the fault transitions to a transtensional regime. As a consequence of the westward escape tectonics and counter-clockwise rotation of Anatolia, the direction of maximum strain from the restraining bend is predicted to be on its western flank. Using fluvial terrace ages of the Filyos River Valley, this thesis aims to contribute the first long-term rock uplift rates on the western flank. The region is growing in the pattern of a large-scale orogenic wedge with a positive flower structure geometry, causing areas closer to the restraining bend to yield more rapid rock uplift rates. Because the samples from this thesis are located closer to the restraining bend and farther west than the Gökırmak River Basin and the Kızılırmak Delta, long-term rock uplift rates are predicted to be greater than ~0.3 mm/a measured in those locations. During the thesis rock uplift rates were reported on the eastern flank of the restraining bend (0 km from the North Anatolian Fault) on the order of 1 mm/a. The site of this thesis is close to the restraining bend (<50 km), in the direction of strain from the restraining bend, and on the hanging wall of a local reverse fault. Therefore, it would be expected to reveal rock uplift rates of 1 mm/a or greater, especially if the local reverse fault has been active during the Quaternary.

In the Filyos River Gorge there is evidence of more than one displacement of the main river channel on scales of >100 m. Fluvial terraces were formed and preserved in these paleo-channels (wind gaps). While their remnants and configuration may appear ancient, we expect that their ages will be within the range of the OSL technique due to the expected relatively rapid incisional response the main river should have to uplift.

This would also confirm the formation of a 1 km-long epigenetic gorge from hillslope failures and channel migration.

Downstream from the Filyos River Gorge, an area of fill terraces formed along a wider valley eroding clastic bedrock. It is assumed that these terraces are older because of their high degree of erosion and minimal preservation. One area with excellent preservation was at a main-river tributary junction, where there is an unconformity in the stratigraphy between finer gravels which are overlain by much coarser and more angular clasts. Using OSL, the lowest fluvial terrace layer underlying the coarser clasts was sampled for its depositional age while the landform surface was sampled using cosmogenic ^{36}Cl exposure dating to understand the age of the overlying coarser and more angular clasts. It was assumed that a tributary junction alluvial fan developed overlying the lowest fill terrace level. The ages should allow the construction of a landscape model and comparison with the regional data and landscape model upstream. We predict that aggradation downstream should influence the incisional response of the main river upstream and possibly depress rock uplift rates.

2. MATERIALS AND METHODS

2.1 Mapping and Field Measurements, Filyos River Gorge

We conducted mapping and exploration of the western side of the Central Pontides using Google Earth and the Advanced Land Observing Satellite (ALOS) World 3-D digital surface model (DSM) (resolution: 30 m horizontal, 3mvertical). Notes and coordinates of landscape features were combined with the previous mapping data to produce a geomorphic map. During fieldwork, a DJI Phantom III Unmanned Aerial Vehicle (UAV) gathered aerial images used to analyze surface features and produce publication illustrations. To better understand the distribution of fluvial terraces and their relative positions, a DSM was created using a Sensefly Ebee UAV (mean horizontal accuracy: 6.6 cm). Details of the processing methods were written in Section 2.2. In gorge settings recording accurate elevations relative to sea level was made possible by using a Lecia differential GPS (dGPS), with an accuracy of ~20 cm. Trunk river bedrock was the reference point for the terrace staircase since it does not vary more than centimeters near the terraces. We used a Nikon Forestry Pro laser rangefinder with an error range of ±1 m to survey relative positions of terrace straths that were difficult to access. The rangefinder was used to gather multiple strath elevations along the terrace length and to record sediment thickness. The rangefinder and dGPS measurements were then amalgamated to create two-dimensional profiles of sediment thickness and average strath elevations above the Filyos River channel. In landslide-prone areas, distinguishing colluvium from alluvium is a priority when sampling terraces. In scenarios where channel interpretation is not straightforward, imbrication may be useful to interpret paleo-flow directions. Therefore, sediment thickness, grain sizes, clast sizes, roundness, clast lithologies, and facies sequences and boundaries were recorded when possible.

2.1.1 OSL-sampling, Filyos River Gorge

In OSL dating, light is used as a stimulation source to release electrons from traps stored in quartz lattices since the time of burial (Aitken, 1998). Sediment was sampled from five of the seven fluvial terrace levels in the gorge terrace staircase: T1 (highest),

T3, T5, T6, and T7 (lowest) (Figures 3.2–3.4). These terraces are located on the hanging wall of the Karabük Fault, between 0.6 and 2 km from the fault, with a range of strath elevations exceeding 200 m above the river level. Three OSL samples were collected from each sample location, which allows us to identify erroneous outliers, if present, and potentially reduce high methodological uncertainties associated with older OSL samples. We selected sample sites as close to the strath as possible since these sediments are more likely to be protected and not reworked. Each sample was extracted by hammering an opaque ~12 cm in diameter tube perpendicularly into a ~20 cm cavity dug into the terrace riser sediments. Finally, one environmental radiation sediment sample was collected at each site to constrain dose rates.

2.1.2 OSL laboratory procedures

All laboratory procedures were performed under dim red light. The collected samples were separated into 90–180 μm grains through wet sieving. Baths of 10% hydrochloric acid (HCl) removed carbonate, 10% hydrogen peroxide (H_2O_2) removed organic material, and 40% hydrofluoric acid (HF) dissolved feldspar. The remaining quartz grains were etched with 40% HF for 40 min, eliminating outer surfaces affected by alpha radiation. The samples were treated again with HCl then washed with distilled water. The purity of quartz grains was tested using infrared stimulation. Quartz aliquots of each sample were mounted on aluminum disks using silicon spray for OSL measurements. All measurements were carried out at the Luminescence Research and Archeometry Laboratory (Işık University, Istanbul) using an automated Risø DA-15 TL-OSL system equipped with an internal ^{90}Sr-^{90}Y beta source (~0.095 Gy/s). The optical stimulation was carried out with blue 470 nm light-emitting diodes (LEDs) (40 mW/cm^2) and 880 nm IR LEDs (~135 mW/cm^2). Detection of luminescence signals was performed using an EMI 9635QA photomultiplier tube fitted with 7.5-mm-thickness Hoya U-340 filters (Bøtter-Jensen, 1997).

2.1.3 Equivalent dose (De) estimate

We used the Single-Aliquot Regenerative Dose (SAR) protocol, which measures the natural luminescence signal before subsequent measurements of luminescence signals produced by given laboratory doses on the same aliquot (Murray & Wintle, 2000). Examples are shown in a radial plot of single grain De distributions for samples BLK-05 and BLK-08 (Figure 3.6). A small fixed test dose was utilized to correct and monitor

sensitivity changes during the procedures (Murray & Wintle, 2000). We used the SAR protocol with six cycles: natural dose (i = n), three regenerative doses (i = 1, 2, 3), bleach zero dose (i = 0), and finally a regenerative dose identical to the first regenerative dose (i = 1). In each cycle, the single aliquot was first preheated at 260°C for 10 seconds then recorded with blue light stimulation at 125°C for 40 seconds to obtain the main OSL signal (Li). A fixed small test dose was applied and the OSL signal (Ti) was measured at 125°C for 40 seconds before heating to 190°C. Sensitivity corrected signals (Li/Ti) were then obtained for each cycle. The corrected points were used to construct a growth curve (Figure 3.6).

Equivalent dose (De) to natural dose was found by interpolating the corrected natural signal (Ln/Tn) onto the x-axis through the growth curve that was measured before saturation. The SAR protocol suggests internal tests to validate the results. One of these tests is the "Recycling Ratio," defined as the ratio of the repeated doses. In SAR, the first regenerative dose (i = 1), given after the natural dose (i = n), was repeated in the last cycle to check for the sensitivity changes. The ratio between the normalized signal and that obtained after the first cycle should be close to 1, with a common tolerance of ±10% (Murray & Wintle, 2000). Besides monitoring the sensitivity change, the first regenerative dose was given to the same aliquot to monitor the sensitivity change in OSL signals of the same dose recorded at two different cycles, R1 and R5. These were terminated as the recycling ratio (R5/R1), which is expected to be close to unity. This was also an internal test for repeatability of the same dose at two different cycles.

Equivalent dose values for each sample were calculated using the De values obtained for each aliquot of the measured sample. Typically, an analysis of 10 aliquots is used to produce an age. We used the "Analyst" program; a Windows-based program that analyzes luminescence data collected using a Risø automated TL/OSL reader. Analyst can automatically process data and generate equivalent doses for each sample aliquot. Overdispersion in measurements can change from sample to sample (between 3.5% to 8.6%).

2.1.4 Dose rate

The luminescence signal measured in quartz is acquired from radiation exposure within the sample, from surrounding sediments, and cosmic radiation. The

environmental dose rate is based on the activity of major radioactive isotopes (U-Th series and K), to which a cosmic ray contribution is added. Alpha radiation was ignored due to its short alpha particle penetration through quartz grains etched by HF. For the cosmogenic contribution calculation, the latitude, longitude, elevation, and sample burial depth were added (Olley et al., 1996; Prescott & Hutton, 1988, 1994). At Acme Labs (Canada), Inductively Coupled Plasma Mass Spectrometry determined the radioisotope concentrations. The carbonate fraction and moisture content affecting the dose rate was also taken into account. Ultimately, the OSL-age of each sample was calculated by dividing the equivalent dose (De) obtained in Gy by the dose rate (Gy/ka), as seen below.

$$\text{OSL Age} = \frac{Equivalent\ Dose\ (De)}{Radiation\ Dose\ Rate} \tag{1.1}$$

2.1.5 Rock uplift rates

When the geometry and age of paleo-bedrock surfaces formed by fluvial erosion are measurable, the bedrock incision rate can be calculated and used as a rock uplift proxy (Burbank and Anderson, 2011). Strath terraces preserve elevated floodplains at a precise elevation that are often suitable for such calculations. However, when the amount of aggradation exceeds the transport capacity of a river, bedrock incision and lowering of the local base level is prevented (Burbank and Anderson, 2011). Fill terraces may also be used if the strath is visible and assumed to be the former base of the river channel, but complications should be considered regarding the prevention of incision due to aggradation and the potential climatic signal associated with fill terraces. If the main river can efficiently remove thick valley infill, its strath may be useful for rock uplift rate calculations. Otherwise, fill terraces in tectonically-active intermountain environments may represent periods when bedrock incision rates widely underestimate tectonically-driven rock uplift rates. We calculated the rock uplift at two locations to corroborate their validity.

Due to the lack of difference between weighted and arithmetic averages (A) of three coeval OSL samples from each terrace level (X ± x, Y ± y, Z ± z), we chose to use the arithmetic average (A) for uplift rate calculations.

$$\text{Arithmetic Average} = \left(\frac{X+Y+Z}{n}\right) \pm \frac{Stdev(A,B,C)}{\sqrt{n-1}} \tag{1.2}$$

For each OSL sample (X), there is a methodological error (x). Error propagation was used to calculate the average error (a) to report with each average OSL age (A):

$$a = \left(\frac{1}{n}\right) * \sqrt{x^2 + y^2 + z^2} \quad (1.3)$$

where (n) equals the number of samples. This yields (A ± a) ka.

Fluvial incision rates are widely considered valid proxies for inland area rock uplift rates (Litchfield & Berryman, 2006). Average rock uplift rates can be calculated between any displaced paleosurface elevation (E) above the river channel with a known age (A) and a younger paleosurface elevation above the river channel (F) with a known age (B). The modern river channel, where (F = 0) and (B = 0) can also be used. The equation divides the difference in elevation by the difference in age:

$$U = \frac{(E-F)}{(A-B)} \quad (1.4)$$

The errors associated with elevation measurements (E) and (F) are represented by (e) and (f). The errors calculated in equation 1.3 from ages (A) and (B) are represented by (a) and (b). These errors were propagated as follows. Variable (D) is the distance between levels, where (D = E-F). Variable (d) is the measurement error between two levels in an average uplift rate calculation. Variable (T) is the time between the landform ages, where (T = A-B). Variable (t) is the temporal error between the error margins of each landform age. Propagation of each of these errors uses the same equation:

$$d = \sqrt{e^2 + f^2} \quad (1.5)$$

$$t = \sqrt{a^2 + b^2} \quad (1.6)$$

After solving for the average uplift (U) in equation 1.3, the uplift rate error (u) can be solved with the following equation:

$$u = (U) * \sqrt{\left(\frac{d}{D}\right)^2 + \left(\frac{t}{T}\right)^2} \quad (1.7)$$

This produces an average uplift rate (U) with an error (±u).

2.2 Geomorphic Mapping, Main River-Tributary Junction

Using GoogleEarth and the ALOS-2 Digital Surface Model (DSM), we investigated the first 6 km downstream from the main gorge for fluvial terrace levels by mapping

relatively planar surfaces higher than the modern floodplain. Before choosing study areas to investigate, exploratory fieldwork was performed along over 100 km of the main river valley as well as many tributaries and the adjacent Bartın and Ulus basins. The environment downstream of the main gorge was chosen due to it being the start of a transition towards relatively high aggradation compared to upstream and having multiple accessible fluvial terrace levels that can be used to calculate rock uplift rates. It was also chosen because of fresh outcrop conditions where a temporary tributary junction alluvial fan may have formed. We used the ALOS-2 DSM to produce a detailed geomorphological map of the terraces, present-day floodplain, topography, and rivers. At the tributary junction where a suspected alluvial fan may have formed, we produced a high-resolution DSM of the terrace and adjacent floodplain. This terrace is often referred to as the junction terrace. Two large landslides were measured using the ALOS-2 DSM and photographed in the field. Outcrops were visited and described where present and the sediment characteristics of the valley floor were described. A Leica differential GPS (dGPS) was used to measure important features, such as straths, treads, and the river channel.

To produce the high-resolution DSM at the junction terrace, the coordinates and elevations of key points were recorded using dGPS. These were used as ground control points for the DSM. A Sensefly Ebee UAV was used to collect elevation data above the floodplain and terrace area at the main river-tributary junction. The DSM was created with a mean vertical accuracy of 23.4 cm and a horizontal accuracy of 7.2 cm. Pix4D software was used to orientate images and extract cloud points. Processing included triangulation with camera calibration and a subsequent automated model generation. Following each acquisition, alignment of acquired images was performed, then a pixel-based dense stereo reconstruction was implemented. Fine topographic details available from the original images were meshed and texturing was applied to the mesh. The point cloud was then derived and referenced to the UTM coordinate system with the bundle adjustment procedure. The point clouds extracted by UAV-SfM (Structure from Motion) methodology represented different point densities depending on the image's textural properties. Therefore, DSMs were generated from point clouds. The SfM technique applied to images acquired by a low altitude UAV system produced a point cloud and derived DSM with high topographic quality. The dGPS ground control points georeferenced the orthomosaics and sparse DSMs, while

the UAV acquired aerial images of the area with 12 MP resolution. The data have a front overlap (along-track) of 75% and a side overlap (across-track) of 70%. The ground sampling distance of the derived DSM is about 5 cm. These images and surface models were used as base maps of the geomorphic mapping.

2.2.1 Sedimentological and stratigraphic analysis, main river-tributary junction

The lowest fluvial terrace level (junction terrace) captured our attention due to the large, fresh outcrop facing the tributary to the south and the strong likelihood of its upper layers originating from a tributary fan. A south-facing outcrop of the uppermost 10-14 m was recently excavated, providing an opportunity to identify, measure, and describe characteristics of different layers within the landform. Most importantly, we wanted to differentiate between the potential alluvial fan and fluvial layers. Therefore, grain morphologies, such as roundness, shape, and sphericity, were documented. Grain size, matrix and cement characteristics, grain sorting, grading, and other characteristics were described. Rounder and finer layers with bedding or imbrication in the main river direction can suggest fluvial deposition, while larger, angular clasts can indicate an alluvial fan. To illustrate layer thicknesses and angles of boundaries, a laser range finder was used across the outcrops.

2.2.2 OSL and cosmogenic ^{36}Cl surface exposure dating sampling, main river-tributary junction

OSL dating is a method used to estimate deposition ages of sediment by calculating quartz and feldspar mineral's last exposure to daylight (Chen et al., 2012; Fuchs and Lang, 2009). The fresh excavation on the south side of the junction terrace had a quartz-rich fluvial sand/silt lens in which OSL-samples were extracted to estimate the age of the most recent valley-wide aggradation that formed a fill terrace. The absence of fine layers in the higher and presumably older terraces prevented sampling. The degree of erosion of those terraces also created a strong possibility of ages beyond the limit of OSL dating.

On the junction terrace tread surface, where the tributary is suspected to have formed a temporary alluvial fan overlying fill terrace sediments, the least disturbed areas of the uppermost 2 to 4.5 cm of three well-rooted, rounded, limestone boulders were extracted by hammer and chisel for cosmogenic ^{36}Cl exposure dating. Alluvial fan cosmogenic samples should be collected away from the landform margins, where

modification by erosion or deposition may have occurred (Anderson and Anderson, 2010). The boulders were at three different locations, all away from the incised margins and anthropogenic excavations (Figure 3.3). We also avoided the small village in the northeast quarter of the landform. The only evidence of surface disturbance around the samples is from grazing. The samples provide exposure ages of the proposed alluvial fan's clasts to estimate a minimum abandonment age of the landform. A sample of a similar size boulder was also collected from the modern river channel for calculation of minimum ^{36}Cl inheritance. The ages of the fill terrace and tributary junction alluvial fan can yield an estimation of the duration of aggradation, where the uplifting channel is prevented from incising bedrock. The strath underlying the fluvial fill terrace may also be used to calculate recent rock uplift rates for this location by dividing the vertical distance incised through a given time until present.

2.2.3 OSL laboratory procedures and equivalent dose (De) estimate

The SAR protocol was used for the OSL samples at the main river-tributary junction as in Section 2.1.3. These samples were processed and measured using the same methods, instruments, and laboratories as the strath terraces upstream in the Filyos River Gorge.

2.2.4 Cosmogenic ^{36}Cl exposure dating laboratory procedures

For the three limestone boulder samples from the surface of the fluvial terrace, chemical preparations were performed at the İTÜ Kozmo-Lab in Istanbul, Turkey according to procedures described in Sarıkaya et al. (2015). Samples were first crushed and sieved to gather the 0.25-1 mm fraction. This fraction was leached in deionized water and 10% HNO_3 then totally dissolved in HDPE bottles with 2 M HNO_3 as in (Schlagenhauf et al., 2010). ^{35}Cl (~95.28%) enriched Aldrich carrier ($Na^{35}Cl$) was added to the samples before total dissolution and chlorine was precipitated by the addition of $AgNO_3$. To remove sulfur from the final solution, precipitation of $BaSO_4$ was repeated via the addition of saturated $Ba(NO_3)$ and reacidifying with concentrated HNO_3. The final AgCl targets were sent to the CNRS-ASTER, Aix en Provence, France for measurements using Accelerated Mass Spectrometry (AMS). Following AMS measurements, the total Cl was calculated using the isotope dilution method of Desilets et al. (2006). Aliquots of leached samples were used to determine the major and trace element concentrations at the AcmeLabs, Canada. Relevant geochemical

data are reported in Table 3.2. To estimate local ^{36}Cl production rates, we used a combination of rates provided by the CRONUS-Earth (Cosmic-Ray Produced Nuclide Systematics on Earth) project (Borchers et al., 2016; Marrero et al., 2016; Phillips et al., 2016). Calculations of exposure ages were made using the CRONUS Web Calculator (URL-1) (Marrero et al., 2016). To perform an inheritance correction, a similar size channel boulder was sampled to estimate the inheritance using its concentration of nuclides. This concentration was subtracted from the concentrations of the three limestone boulder samples.

3. RESULTS

3.1 Geomorphology of the Filyos River Gorge

The strath terrace staircase occurs on the hanging wall of the Karabük Fault in a segment of the upper Filyos River Gorge. On the hanging wall the relief on the hillslopes increases (Figure 3.1C). The hanging wall bedrock is comprised of mostly turbidites, which accommodate the required lateral erosion for terrace formations. As the main river (Filyos) flows from the footwall to the hanging wall of the Karabük Fault it meets the first of two tributaries. The junction of the first tributary (Küçük River in Figure 3.1) is located at a widened valley floor with at least two terrace levels. The valley here is nearly 1 km-wide at its widest location. In the final 2 km of the tributary, the valley floor is aggraded covering 100 to 300 m of the valley floor. This segment of the main valley is followed by a 1 km-long granite bedrock gorge. Here, the second tributary junction occurs (Kavarılık River), where the valley is hanged 51 m over the main river. The main river then continues over turbidites again where lateral erosion widened a 1-km segment of the valley to a maximum of ~700 m. This segment is labeled Bolkuş Valley in figures and four terrace levels with three sampled for OSL ages. For the next 12 km, the main river incises through granite, limestones, and marbles, forming high relief on the hillslopes and minimal lateral erosion or valley floor formation.

The DSM we created illustrates the extent of terrace levels T3 through T7 (Figure 3.1a). The geomorphic map of the upper Filyos River Gorge illustrates local landscape features associated with rock uplift (Figure 3.1b). The slope map (Figure 3.1c) illustrates incision on the hanging wall block as well as lateral erosion achieved where terraces formed. Photographs of some sampled outcrops, fluvial terrace morphometries, and landscape features in the upper Filyos Gorge are in Figures 3.2–3.4, with photo directions depicted in Figure 3.1. Figure 3.5 shows a map of hanging valleys and the profiles of the tributaries connecting with the main river.

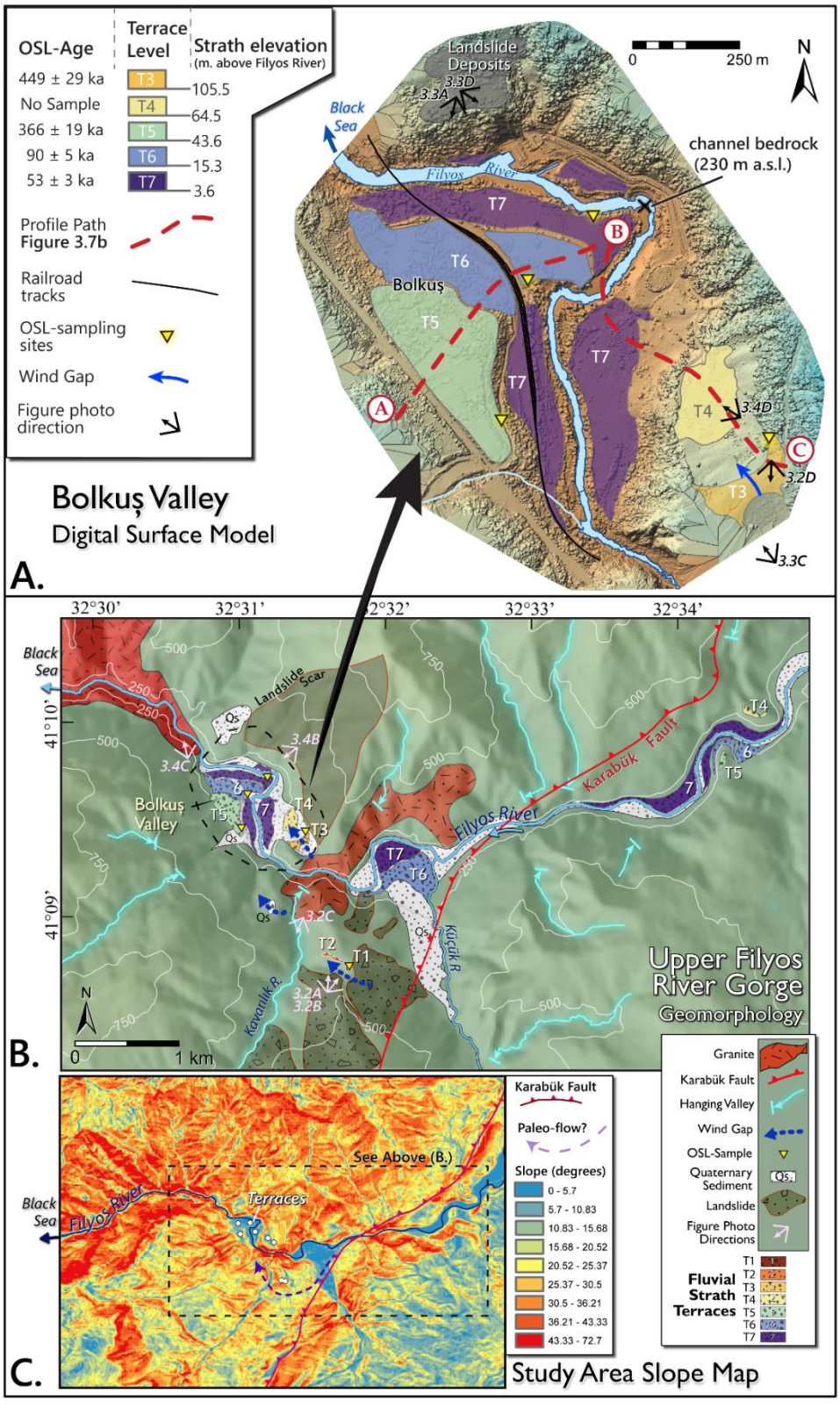

Figure 3.1 : (a.) Digital surface model (DSM) of the Bolkuş Valley segment of the Filyos River Gorge, depicting terrace surfaces for the five lowest levels. The Red dashed line is the location of the topographic profile of Figure 3.7b. (b.) Upper Filyos River Gorge geomorphic map. Black dashed outline represents the area of the DSM above. (c.) Slope map showing incision of the upper Filyos River Gorge. Black dashed box represents the area of section B.

500 m south of the granite gorge T1 and T2 are located in a wind gap of the main river. 300 m north of the granite gorge, T3 is located in another wind gap of the main river. Landslides are mapped south of T1 in the Kavarılık tributary while a landside scar of 1.2 million m2 was mapped north of the Bolkuş Valley.

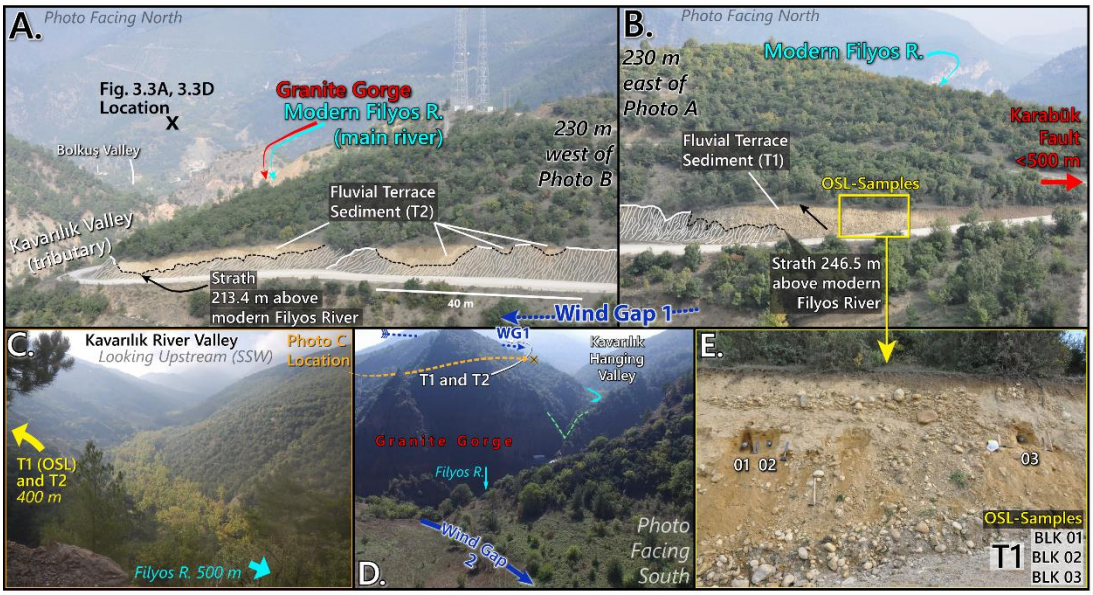

Figure 3.2 : Photos A and B, taken from the same location. (a.) Terrace 2 strath and sediments. (b.) Terrace 1 strath and sediments, including the OSL-sample location. (c.) Photo of the Kavarılık River tributary valley, a hanging valley. Photo location is downstream from T2 and 500 m upstream from the main river junction. (d.) UAV view of the tributary valley (Kavarılık) hanged above its junction with the main river (Filyos) at the gorge. WG = wind gap. (e.) Photo of T1 OSL sediment outcrop.

3.2 Stratigraphy of the Fluvial Terraces, Filyos River Gorge

Fluvial terrace elevations at the strath, overlying sediment thickness, and basic sediment characteristics are organized in Table 3.1. The thickest terrace was T5, a fill terrace with 21 m of sediment overlying the strath. The oldest three terraces had thin sediment cover (≤4 m) and relatively less horizontal extent (Table 3.1 and Figures 3.1 and 3.7b).

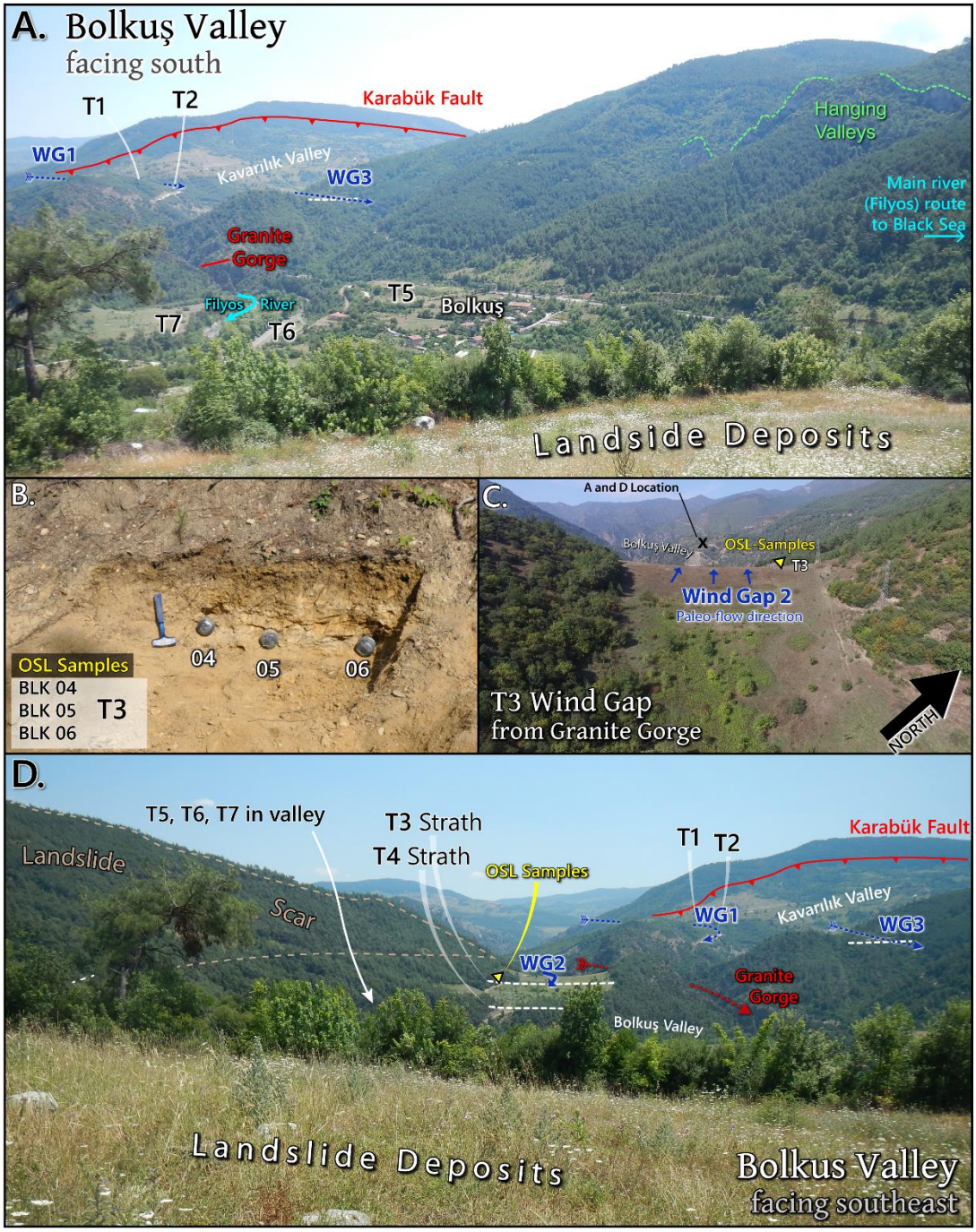

Figure 3.3 : (a.) View of lowest terrace locations from unconsolidated sediment perched above Bolkuş Valley. (b.) T3 OSL outcrop with sample tubes. (c.) Photo of wind gap 2, taken by a UAV above the gorge. (d.) Photo of T1 through T4 locations from the same location as photo A. From this angle, background features such as the landslide scar and footwall of the Karabük Fault are more visible.

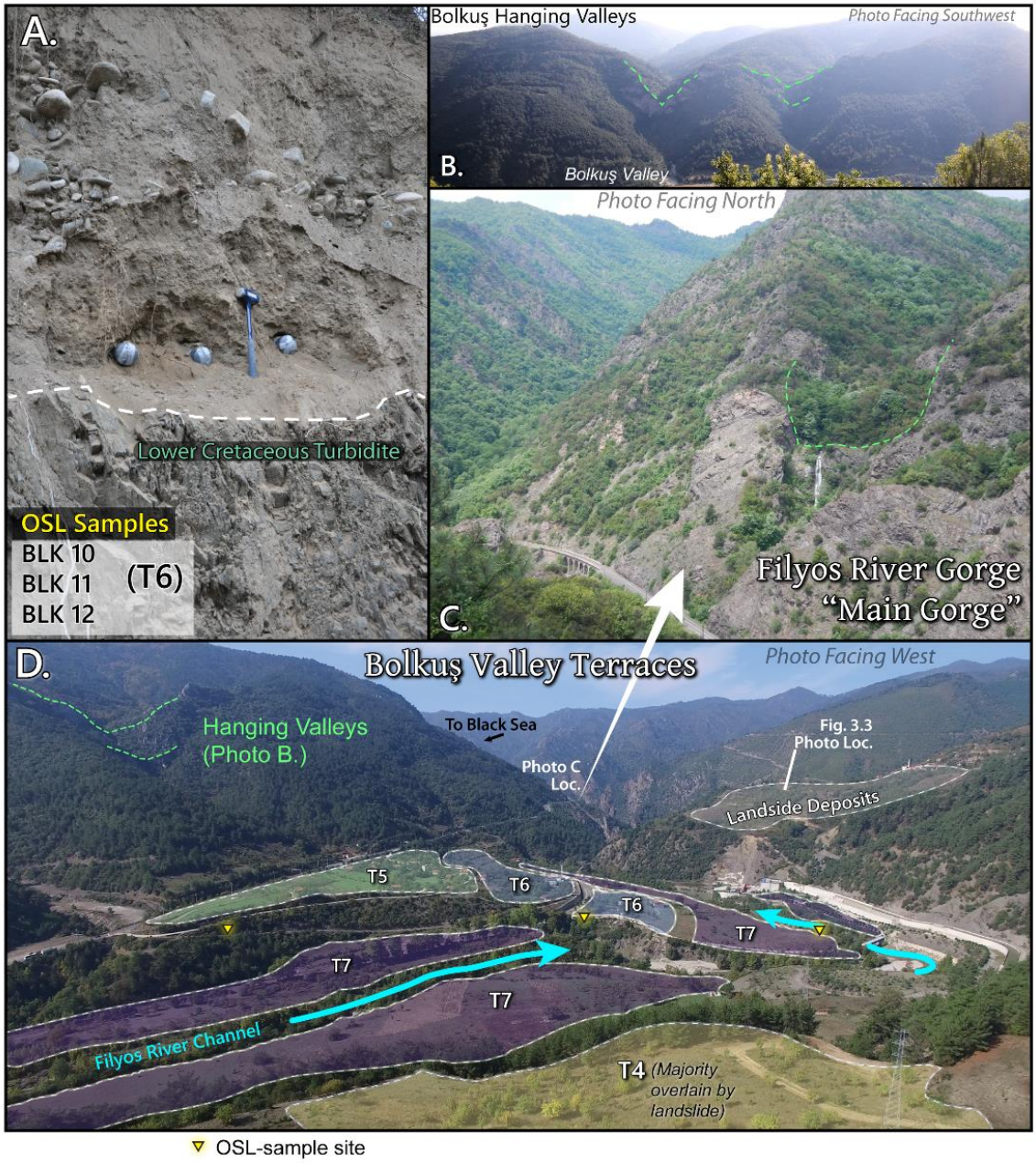

Figure 3.4 : (a.) Outcrop of sampled OSL-sediment of T6. Dashed line represents strath. (b.) Hanging valleys above Bolkuş Valley. (c.) Gorge downstream from Bolkuş, where the Filyos River leaves the terrace area. (d.) Overview of the lowest terraces at the village of Bolkuş.

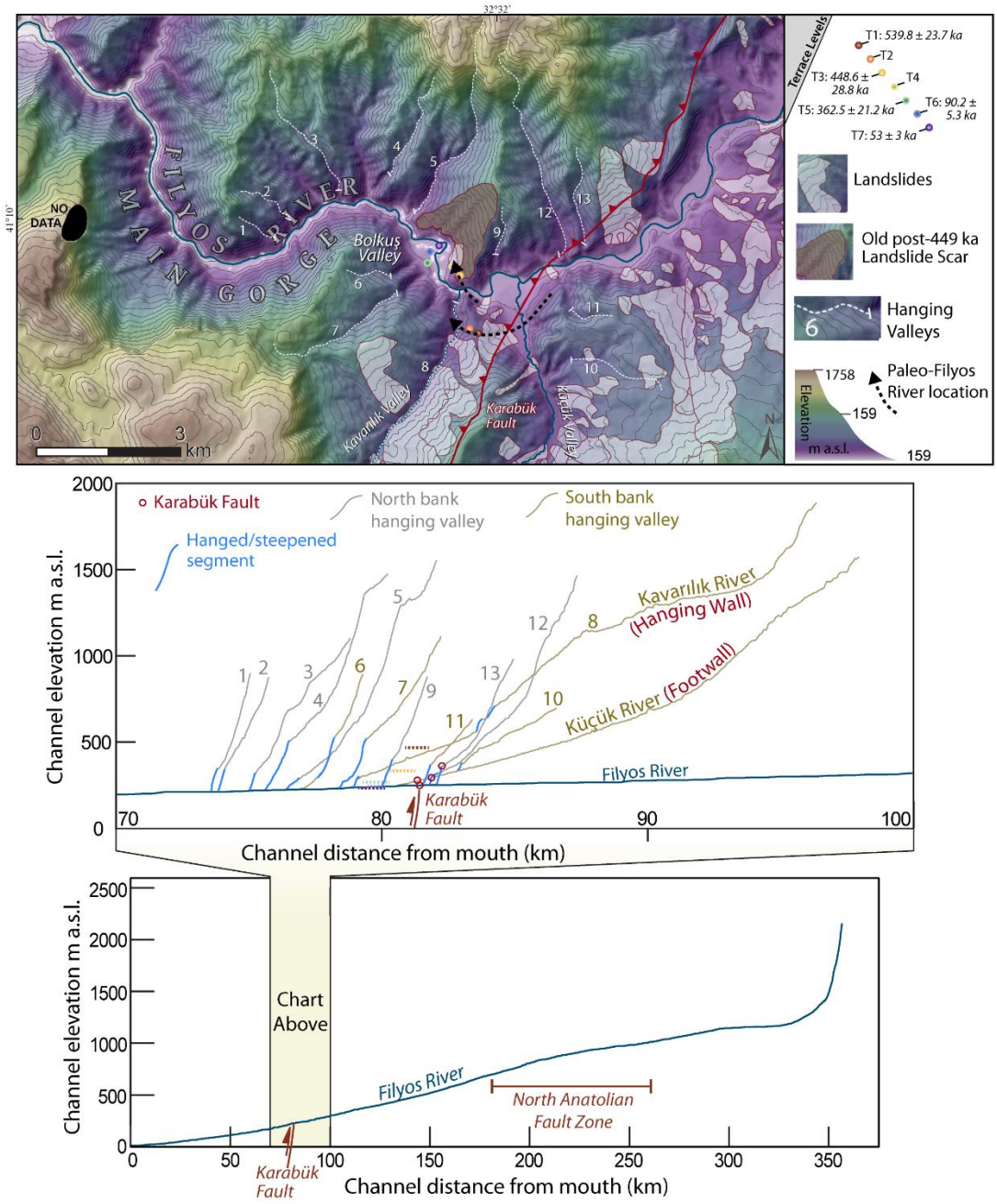

Figure 3.5 : (top) Topographic map of the Filyos River Gorge showing locations of all hanging valleys. (middle) Stream profiles of hanging valleys and a selected tributary, the Küçük River, which flows mostly on the footwall. The difference in uplift between the Küçük and Kavarılık tributaries may partially result from the uplift of the hanging wall. (bottom) A full stream profile of the main river of the study, the Filyos River. The strike-slip motion of the North Anatolian Fault along ~70 km of the river is the main disturbance to the concave-up profile. The shaded yellow area represents the reach of the river illustrated in the middle chart.

Table 3.1 : Sediment of the main river fluvial strath terraces in the upper Filyos River Gorge.

	Wind Gap 1		Wind Gap 2	Modern Channel			
Terrace level	**T1**	T2	**T3**	T4	**T5**	**T6**	**T7**
m a. s. l.	476.9	443.8	335.9	296	271.5	245.7	234
m above river	246.5	213.4	105.5	65.6	43.6	15.3	3.6
Maximum observed sediment thickness (m)	4	3	1.75	4-5	21	3.5	12.2
Terrace Sediment descriptions	Matrix-supported terrace: layered coarse sand to silt, sometimes as lenses and wedges without clasts. High overall clast density with rounded to well-rounded cobbles and large gravels of limestone sandstone, and few metamorphic, 3-30 cm in diameter. Occasional large boulders. Imbrication east to west.		Matrix-supported: poorly-sorted fine sand to silt, with some coarse sand. Clasts coarsened up from well-rounded mm-sized pebbles to rounded 50 cm cobbles. Some cemented sections. Terrace landform eroded and lacking with few outcrops.	Undescribed	**Outcrop 1** (overlying strath): Matrix supported with lenses of medium sand to silt within terrace of high clast density. Clasts subrounded to rounded, medium to low sphericity 0.5-30 cm. **Outcrop 2** (at tread): Matrix-supported by silt with some fine sand. Clasts rounded to well-rounded, fine gravel to cobble-sized.	Matrix-supported by poorly-sorted-primarily fine sand to silt matrix. Fine to medium rounded gravel scattered within. Lowest % of clasts in study. Bands of rounded cobbles of low sphericity occured, some of them tabular or bladed in shape.	Matrix-support-ed. Fining-up sequence from coarse cross-bedded sand to fine sand, overlain by 5-m of layered boulders with fine sand mixed within.
OSL-sample sediment descriptions	Sampled T1's silt lens ~1.5 m above the strath		Sampled silt lens near strath. Hammering difficulty in field and laboratory sieving indicated finer than other terraces.	Did not sample	Sampled silt lenses with some fine sand < 2 m above strath.	Sampled large area of silt with sand and fine gravel scattered within. Sediments bordered strath.	Sampled fine sand 7.5 m above strath.

*__Bold__ terraces levels were sampled for ages.

3.3 OSL ages of fluvial terrace staircase, Filyos River Gorge

Growth curves were constructed, as seen in Figure 3.6. The dose points of these two representative samples, BKL-08 and BKL-15, fit well with the exponential function for these samples. Supporting Information S1b indicates the recycling ratios for all BKL samples. The figure shows that all values were acceptable within a tolerance limit of 5%. In Figure 3.6c, the precision analyses used to calculate De vales using the "Analyst" program are presented for samples BLK-05 and BLK-08. The results from the De of each aliquot showed a small scattering in De distribution and the analyzed grains are assumed to be well bleached. This allowed use of the arithmetic mean for each of the 10 aliquots per sample. The final burial dose rates for the samples were estimated between 0.38 and 0.47 Gy/ka (Table 3.2). The luminescence ages, equivalent doses, and environmental dose rate obtained for each sample are presented in Table S2. From the highest (T1) to lowest (T7) elevations, the OSL-ages of all samples are seen in Figure 3.7 and Table 3.2. Based on arithmetic averages of three quartz OSL-samples per terrace, their respective deposition ages were calculated as 542 ± 24 kyr (T1), 449 ± 29 kyr (T3), 366 ± 19 kyr (T5), 90 ± 5 kyr (T6), and 53 ± 3 kyr (T7).

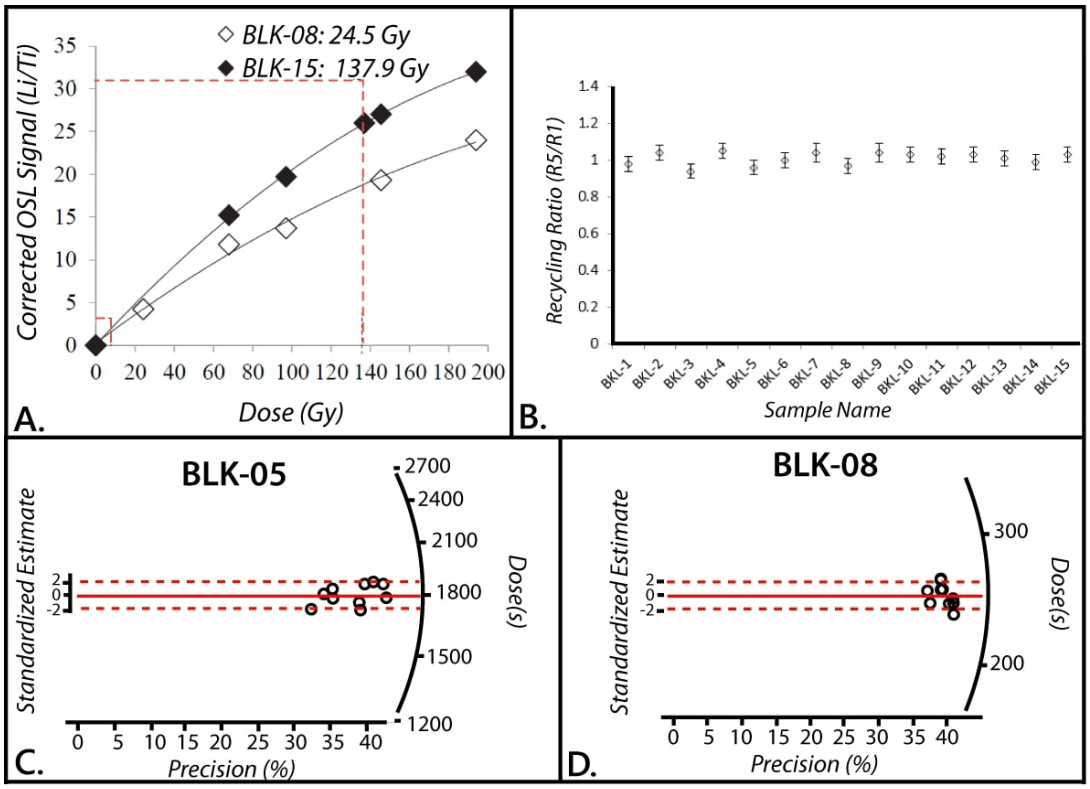

Figure 3.6 : (a.) Dose-response or growth curves fitted using a saturating exponential of representative samples of BLK-08, white diamonds, and BLK-15, black diamonds. Equivalent doses of 24.5 Gy and 137.9 Gy are shown on the x-axis. (b.) Recycling ratio for all samples. All values were acceptable since they are close to unity. (c. and d.) Prevision analyses for BLK-05 and BLK-08 by the Analist program, using 10 aliquots per sample.

Table 3.2 : OSL-ages, equivalent doses, environmental dose rates, and chemistry measured from each sample.

Terrace level	Sample code	Latitude, longitude *(decimal degrees, N, E)*	Depth *cm*	Elevation *m a.s.l.*	Dose *Gy*	Dose rate *Gy*	Cosmic *Gy/ka*	Water Cont.*%*	Carbonate *%*	U *ppm*	Th *ppm*	K *%*	Age (ka)
	BLK-01	41.1453, 32.5289	180	477	197.73 ± 2.79	0.38 ± 0.02	0.19	32.71	49.3	0.5	1.9	0.12	514.7 ± 32.4
T1	BLK-02	41.1453, 32.5289	180	477	211.00 ± 6.00	0.38 ± 0.02	0.19	32.71	49.3	0.5	1.9	0.12	549.2 ± 37.1
	BLK-03	41.1453, 32.5289	180	477	212.80 ± 14.17	0.38 ± 0.02	0.19	32.71	49.3	0.5	1.9	0.12	563.4 ± 51.3
	BLK-04	41.1574, 32.5240	175	336	159.93 ± 4.05	0.38 ± 0.03	0.19	55.72	49.0	0.5	2.4	0.14	418.8 ± 32.2
T3	BLK-05	41.1574, 32.5240	175	336	169.81 ± 22.86	0.38 ± 0.03	0.19	55.72	49.0	0.5	2.4	0.14	444.7 ± 68.0
	BLK-06	41.1574, 32.5240	175	336	185.13 ± 9.02	0.38 ± 0.03	0.19	55.72	49.0	0.5	2.4	0.14	484.8 ± 42.4
	BLK-07	41.1626, 32.5196	500	241	20.65 ± 1.50	0.45 ± 0.03	0.14	29.42	20.81	0.5	2.1	0.13	46.3 ± 4.3
T7	BLK-08	41.1626, 32.5196	500	241	24.46 ± 1.96	0.45 ± 0.03	0.14	29.42	20.81	0.5	2.1	0.13	54.8 ± 6.0
	BLK-09	41.1626, 32.5196	500	241	25.18 ± 0.85	0.45 ± 0.03	0.14	29.42	20.81	0.5	2.1	0.13	56.5 ± 4.6
	BLK-10	41.1606, 32.5174	300	246	43.87 ± 3.37	0.47 ± 0.03	0.17	31.94	25.86	0.5	2.1	0.14	93.1 ± 9.6
T6	BLK-11	41.1606, 32.5174	300	246	42.43 ± 2.82	0.47 ± 0.03	0.17	31.94	25.86	0.5	2.1	0.14	90.1 ± 8.6
	BLK-12	41.1606, 32.5174	300	246	41.16 ± 3.35	0.47 ± 0.03	0.17	31.94	25.86	0.5	2.1	0.14	87.4 ± 9.3
	BLK-13	41.1577, 32.5168	800	273	154.69 ± 9.75	0.39 ± 0.03	0.11	52.54	35.96	0.5	2.4	0.14	394.5 ± 37.6
T5	BLK-14	41.1577, 32.5168	800	273	152.19 ± 7.41	0.39 ± 0.03	0.11	52.54	35.96	0.5	2.4	0.14	376.4 ± 36.6
	BLK-15	41.1577, 32.5168	800	273	137.93 ± 3.04	0.39 ± 0.03	0.11	52.54	35.96	0.5	2.4	0.14	325.8 ± 25.0

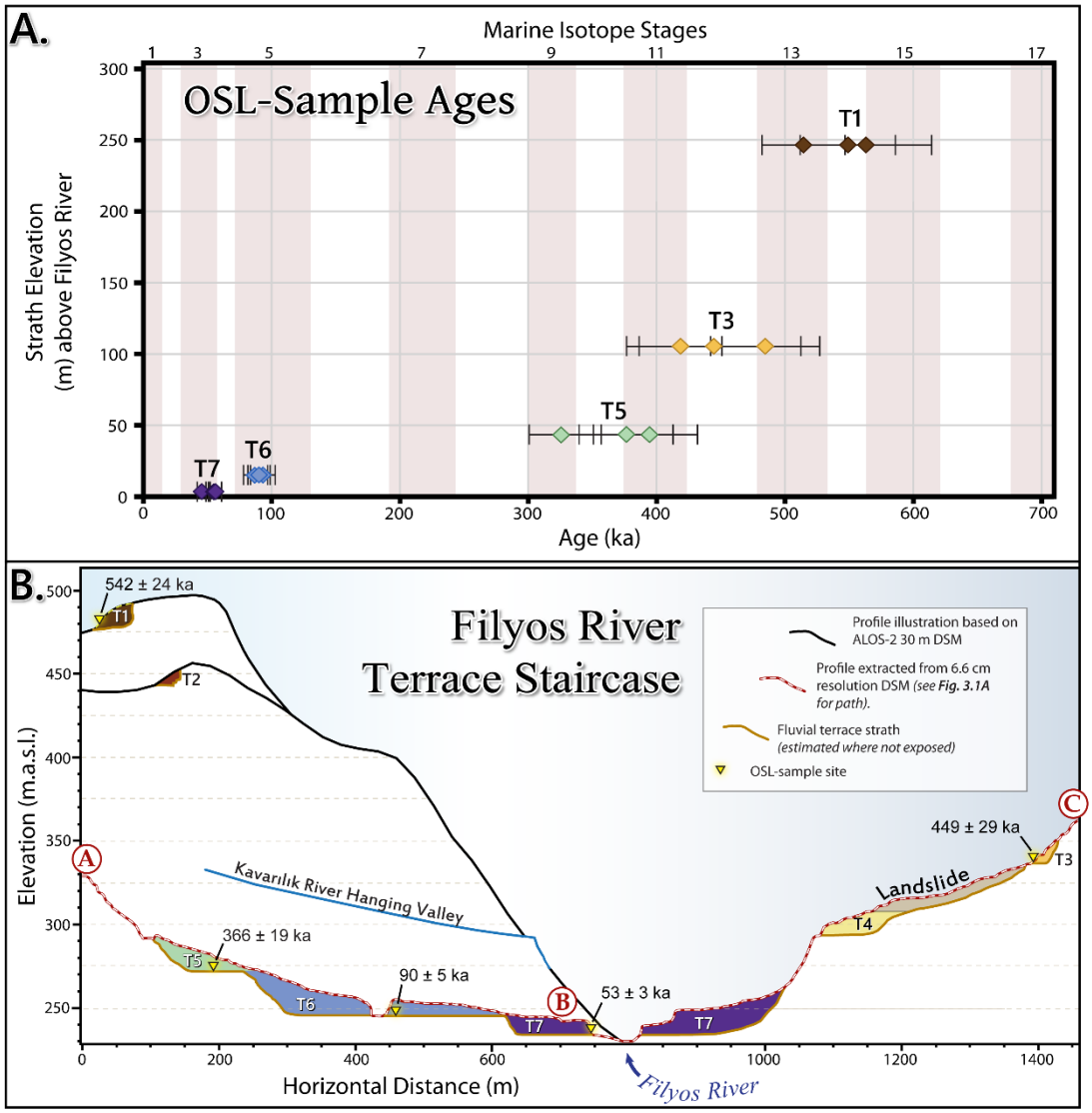

Figure 3.7 : (a.) OSL-sample ages and uncertainties in relation to height above Filyos River. Vertical uncertainties related to strath elevations are too small to depict: maximum: ±3.5 m. (b.) Terrace profiles with OSL-ages. Red dashed line is the profile extracted from DSM of Figure 3.1. Straths are based on measurements of exposed strath outcrops. Therefore, the unexposed bases of the sediments are estimates.

3.4 Rock uplift rates, Filyos River Gorge

OSL ages and elevation of strath levels above the modern river allow us to quantify long-term average rock uplift rates and their variations through time (Figure 3.8; Table 3.3). The highest terrace level T1 is 246.5 ± 0.2 m above the modern river and uplifted during the last 542 ± 24 ka, yielding a 0.45 ± 0.01 mm/a average uplift rate over this time. We could not date the T2 level (213.4 ± 0.2 m above the river) but 105 ± 2.5 m above the river T3 level formed 449 ± 29 ka. Between T1 and T3, the average uplift rate was 1.52 ± 0.6 mm/a. The T4 level was discovered after the OSL-measurements,

but 43.6 ± 2.5 m above the river T5 formed 366 ± 19 ka. During the time between T3 and T5, the average uplift rate was 0.74 ± 0.3 mm/a. The next terrace level at 15.3 ± 0.2 m above the river was T6, formed 90 ± 5 ka. During the time between T5 and T6, the average uplift rate was 0.10 ± 0.01 mm/a. Finally, 3.6 ± 0.2 m above the river, T7 was formed 53 ± 3 ka. During the time between T6 and T7, the average uplift rate was 0.31 ± 0.05 mm/a. During the time between T7 and present, the average uplift rate was 0.06 ± 0.005. Overall, our data suggests a variable rock uplift over time and an average long-term uplift rate of 0.45 ± 0.02 mm/a for the last 539.8 ± 23.7 ka. It should be noted that T5 has 21 m of sediment and could be classified as a fill terrace. However, since our OSL-samples were collected 1 m above the terrace's strath, T5's strath elevation was also used to calculate the rock uplift rate.

Table 3.3 : Dated fluvial terrace levels, vertical incision, and rates between periods in the study.

Short Term Uplift Rates					
Terrace level	Height (m above river)	Age (ka)	Horizontal distance between levels (m)	Time between dates (ky)	Average uplift rates (mm/y)
T1	246.5 ± 0.2	542.4 ± 23.7	141 ± 2.5	93 ± 37.3	1.52 ± 0.6
T3	101.5 ± 2.5	449.4 ± 28.8	61.9 ± 3.5	83.6 ± 34.7	0.74 ± 0.3
T5	43.6 ± 2.5	365.6 ± 19.4	28.3 ± 2.5	275.4 ± 20.1	0.10 ± 0.01
T6	15.3 ± 0.2	90.2 ± 5.3	11.7 ± 0.3	37.7 ± 6.0	0.31 ± 0.05
T7	3.6 ± 0.2	52.5 ± 2.9	3.6 ± 0.2	52.5 ± 2.9	0.07 ± 0.01
Channel bedrock	0	present			
Longer Period Uplift Rates *based on above*		T1 to T5	202.9 ± 2.5	176.9 ± 30.6	1.15 ± 0.2
		T5 to present	43.6 ± 2.5	365.6 ± 19.4	0.12 ± 0.01
	(full study duration) →	T1 to present	246.5 ± 0.2	542.4 ± 23.7	0.45 ± 0.02

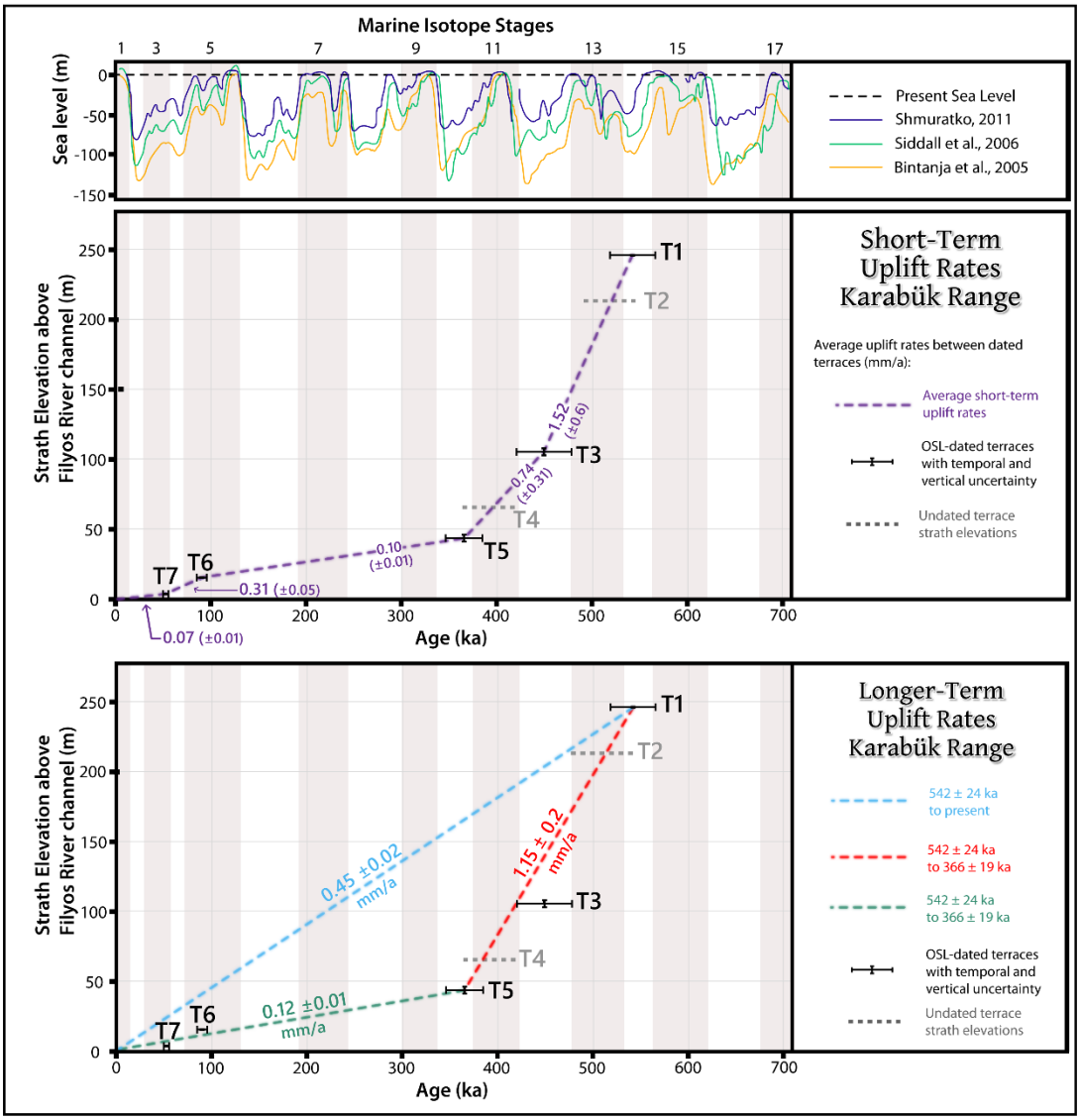

Figure 3.8 : (top) Sea level curves from the last ~700 ka (Bintanja et al., 2005; Shmuratko, 2011; Siddall et al., 2006), modified from Yıldırım et al., 2013a. Warm MIS stages are dully shaded in the background of the graphic. MIS terminations are based on Lisiecki & Raymo, 2005. (middle) Average OSL-ages and error plotted against strath heights in meters above the modern Filyos River. Purple dashed lines are derived from short-term uplift rates between each landform age. (bottom) Same graphic as middle, but dashed lines represent longer-term rates classified by faster pre-366 ka in red and slower post-366 kyr in green. The average long-term uplift from the entirety of the study is also illustrated in blue.

3.5 Geomorphology and stratigraphy, main river-tributary junction (downstream, Study Area B)

In the first 6 km downstream from the main gorge, the bedrock is generally turbidites with many landslide scars on the hillslopes. Relief is higher on the south slope, where the mountains are capped by limestone and the tributary (Şimşir River) incised through the limestone in its final kilometers before connecting with the main valley (Figures

3.9 and 3.10). The fluvial terrace sequence in the main valley is comprised of three fill terrace levels all on the north side of the channel (Figure 3.10). The highest terrace level, Terrace 1 (T1), is a planar landform (tread ~180 m above the modern channel). Many rounded boulders were rooted on the tread. The margins of T1's risers were highly eroded and vegetated, causing poor conditions for OSL-sampling. The middle terrace level (T2) was observed at two locations and had a measured strath of 99 m above the modern channel and an uneven tread between 125-150 m above the modern channel. Sediments in the exposed outcrops were too coarse for OSL sampling (Figure 3.17). Between T2's strath and Terrace 3 (T3) sediments, the bedrock is incised by an intermittent south-flowing stream that turns at a ridge, then flows parallel to the main river for 2 km (Figures 3.10 and 3.17).

The lowest terrace level, T3, was observed at three locations, with two existing in the same cluster above the same floodplain. The upstream location had poor outcrop conditions for observations and was not described. The other T3 in this cluster is located at the mouth of the Şimşir River (tributary). It is the best-preserved terrace in this study and is named the 'junction terrace' for ease of reference. At the junction terrace, the longest planar straths were measured 14 m above the modern channel (Figure 3.11). However, parts of the strath were incised, causing it to dip towards the modern river down to 6 m above the modern main channel. A total of 37 m of sediments were measured overlying the straths. The lowest ~20 m were mostly silt and sand. The bedding structures were unclear in these layers due to poor outcrop conditions, but some sub-layers of rounded gravel were visible in parts. Better conditions were present in the excavation above the lowest ~20 m of sediment.

In the excavation, an unconformity was present about 9 meters below the tread. Below the unconformity, a longitudinal bar and meander were observed. Fluvial gravel layers were visible overlain by 2-3° angles dipping downstream and fining into a sand lens. This lens is the OSL-sample layer and was cut by a north-flowing channel (valley flows east-west) filled with medium to coarse gravel that graded to fine gravel. This is overlain by a 3-6 m thick braided river deposit of higher energy gravels that coarsen upward. Above the unconformity, a significant increase in clast size, poor sorting, and an absence of sediment matrix was present. Two layers are identified with the overlying layer being much coarser. This top layer was sampled on its surface for cosmogenic ^{36}Cl exposure ages of the proposed junction alluvial fan. The sample

locations are marked on the DSM in Figure 3.12. This DSM shows how planar the landform surface is and its extent reaching the north side of the valley. The DSM also reveals a channel incision on the northwest side of the terrace, incising into the alluvial fan layers. Downstream ~4 km from the junction terrace, the third T3 is present with an observed strath 8 m above the modern channel and tread ~45 m above the modern channel. The sediments observed at this terrace were entirely fluvial.

Sediment descriptions and depositional environments are presented in Table 3.4, with details of the large outcrops of the junction terrace. Figure 3.11 presents a UAV view of the junction terrace from across the river, which shows the location of the sampled boulders on the terrace tread and the location where the OSL samples were extracted at the west end of the south-facing outcrop. Figure 3.11 also includes an illustration of the fresh upper 15 meters of outcrops that were exposed by a recent excavation. Photos of the stratigraphy and their interpretations on the west side of this south-facing outcrop are in Figure 3.13 and the east side in Figure 3.14.

At the cluster of terraces, the local floodplain width reaches 500 m upstream from the junction terrace and tributary mouth before narrowing to 180 m at the junction terrace, then widening again downstream to 400 m (Figures 3.10 and 3.12). The floodplain sediments observed upstream were finer, often silt, while the bedload was gravel at the tributary junction and downstream.

Landslide B, which was classified as an old landslide by the Turkish Geological Survey (MTA), was observed and photographed. It slid north into the main valley 2 to 4 km upstream from the junction terrace. The main river has eroded and removed its toe. The remaining landslide scar has an area of 4.1 km^2 with a 915 m vertical distance from its crown to the present base (Figures 1.4 and 3.10). Landslide A, which was previously unidentified, flowed westward into the tributary valley 3.5 to 5 km upstream from the tributary-main valley junction and is immediately upstream from a tributary canyon (Figures 1.4, 3.9, 3.10, and 3.15). The landslide scar has an area of 3.79 km^2 and a 1245 m vertical distance between the crown and toe. Along the toe of the landslide, the stream is deflected westward 300-500 m, where more outcrops of angular clasts overlie bedrock of turbidites. At the channel, a smaller landslide from the west side of the channel converges. The channel in between the two landslides has bedload covering the bedrock. Upstream from the landslides, it was impossible to search for lacustrine sediments due to the steepness of the slope between roads and the

channel. Downstream from the landslide, an outcrop was observed in the field immediately upstream from the tributary canyon, 3.3 km upstream from the confluence with the main valley (Figure 3.16). Here, angular sediments overlie rounded fluvial gravel in a sand matrix (Figure 3.16). In the tributary canyon, the bedload disappears, switching to erosional bedrock. Inside the canyon, there is a 7 to 10 m waterfall with boulders and large clasts trapped on the upstream side. The erosional bedrock begins downstream from this point and lasts until near the main river junction.

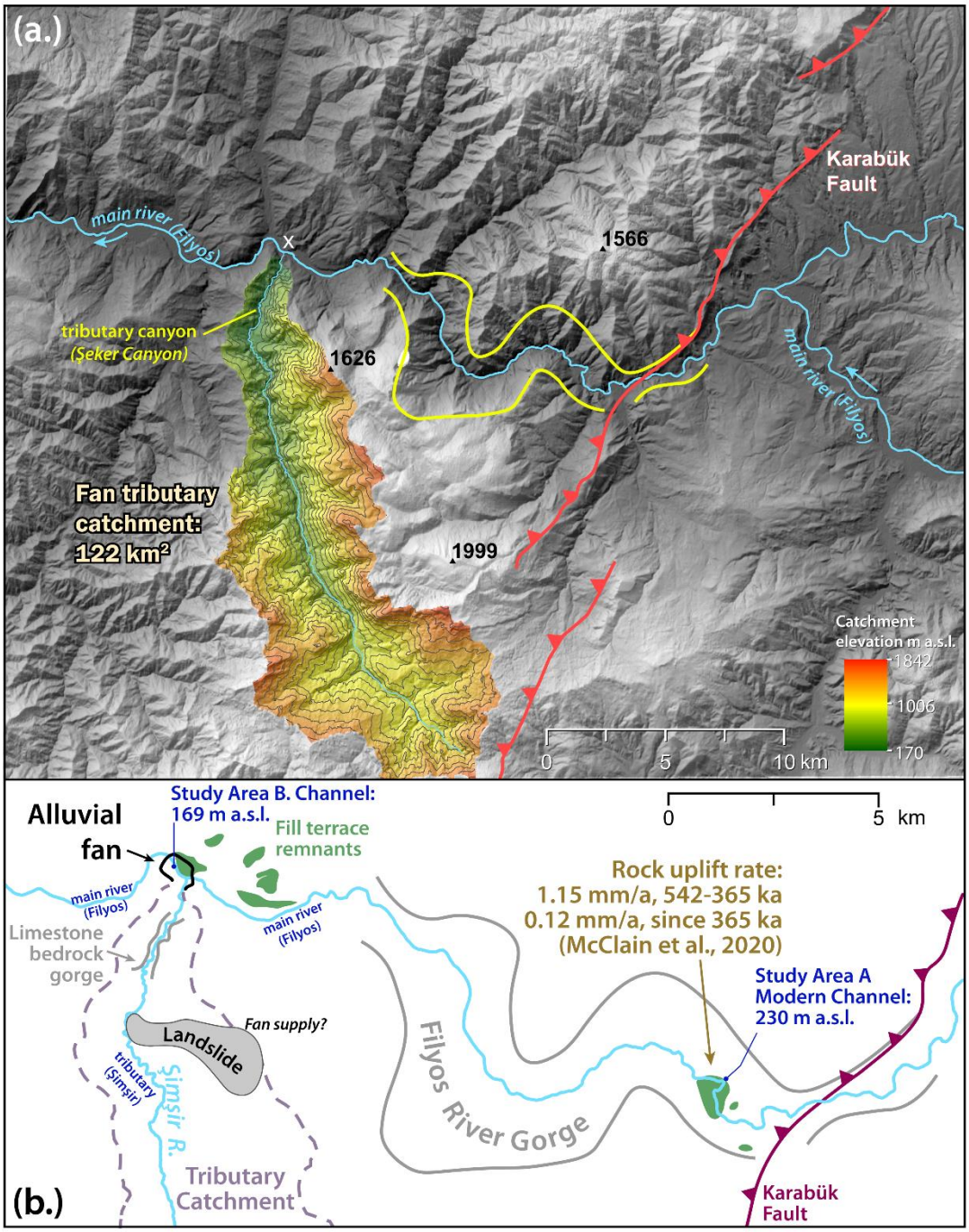

Figure 3.9 : (a.) Topographic hillshade map of Study Area B, showing the tributary catchment of interest (Şimşir River). The contour interval in the tributary catchment is 100 m. The location of two bedrock gorges are marked in yellow and the site of our samples and proposed alluvial fan is marked with a white X. (b.) Simplified map of the study area without topography. This map shows the arrangement of the study setting, with the Karabük Fault, main gorge, and the fluvial terraces of Study Site A (McClain et al., 2020) located upstream to the east of Study Area B. It also shows the location of the tributary bedrock gorge and landslide of interest to the south, with the approximate fan location at the junction with the main river. The modern channel elevations of the study area relative to the upstream study area are important when considering base-level changes and aggradation influence upstream.

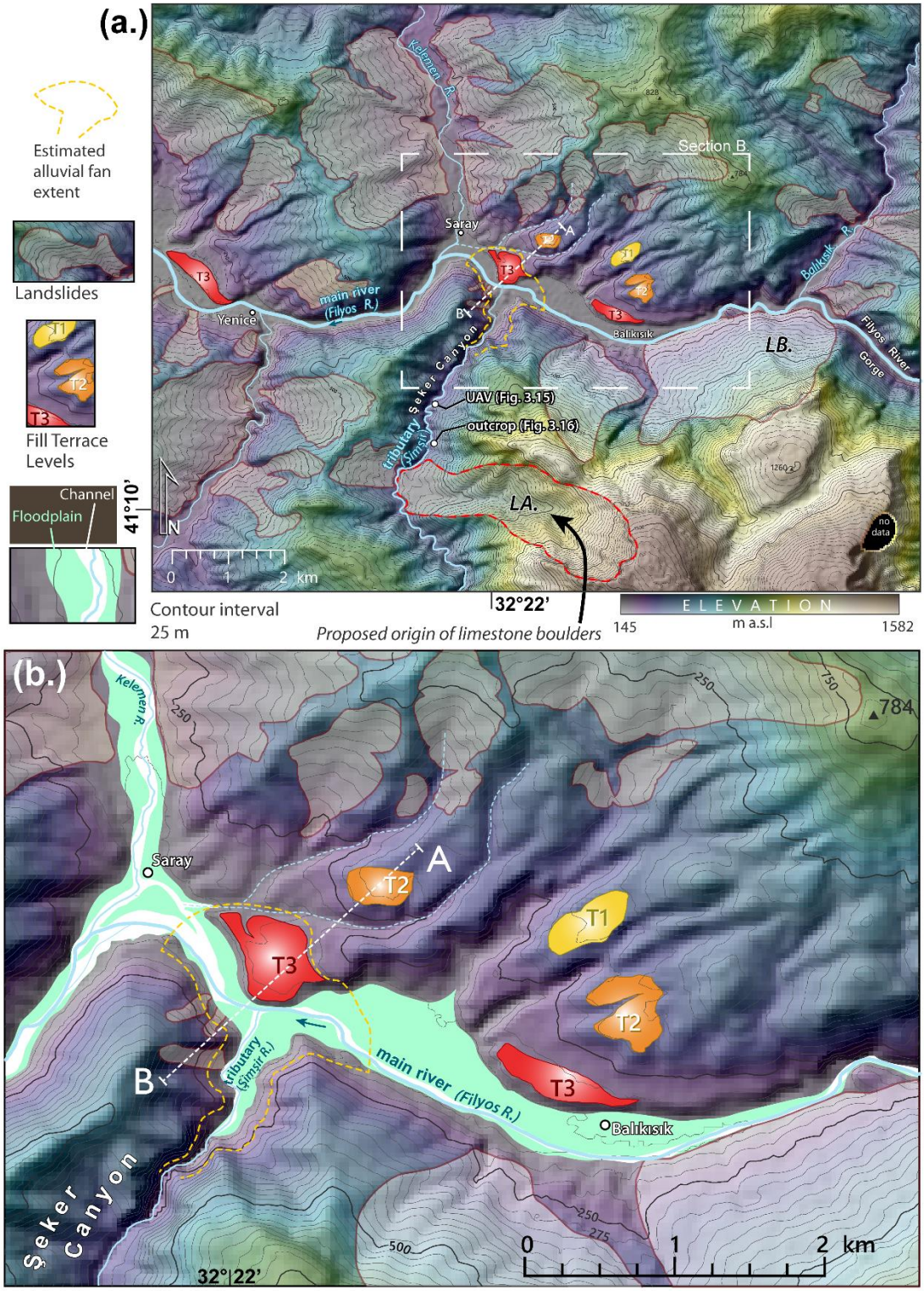

Figure 3.10 : (a.) Topographic map downstream from the Filyos River Gorge, showing the locations of fluvial terraces, landslides, possible extent of proposed alluvial fan, and Figures 3.15 and 3.16 photo locations. (b.) The main river (Filyos) flows westward and the tributary of interest flows northward. (b.) A closer view of the floodplain area and tributary junction is mapped below. The A-B topographic profile of Figure 3.17 is depicted with a white dashed line. Landslides LA and LB and the intermittent channels adjacent to T2 are discussed later.

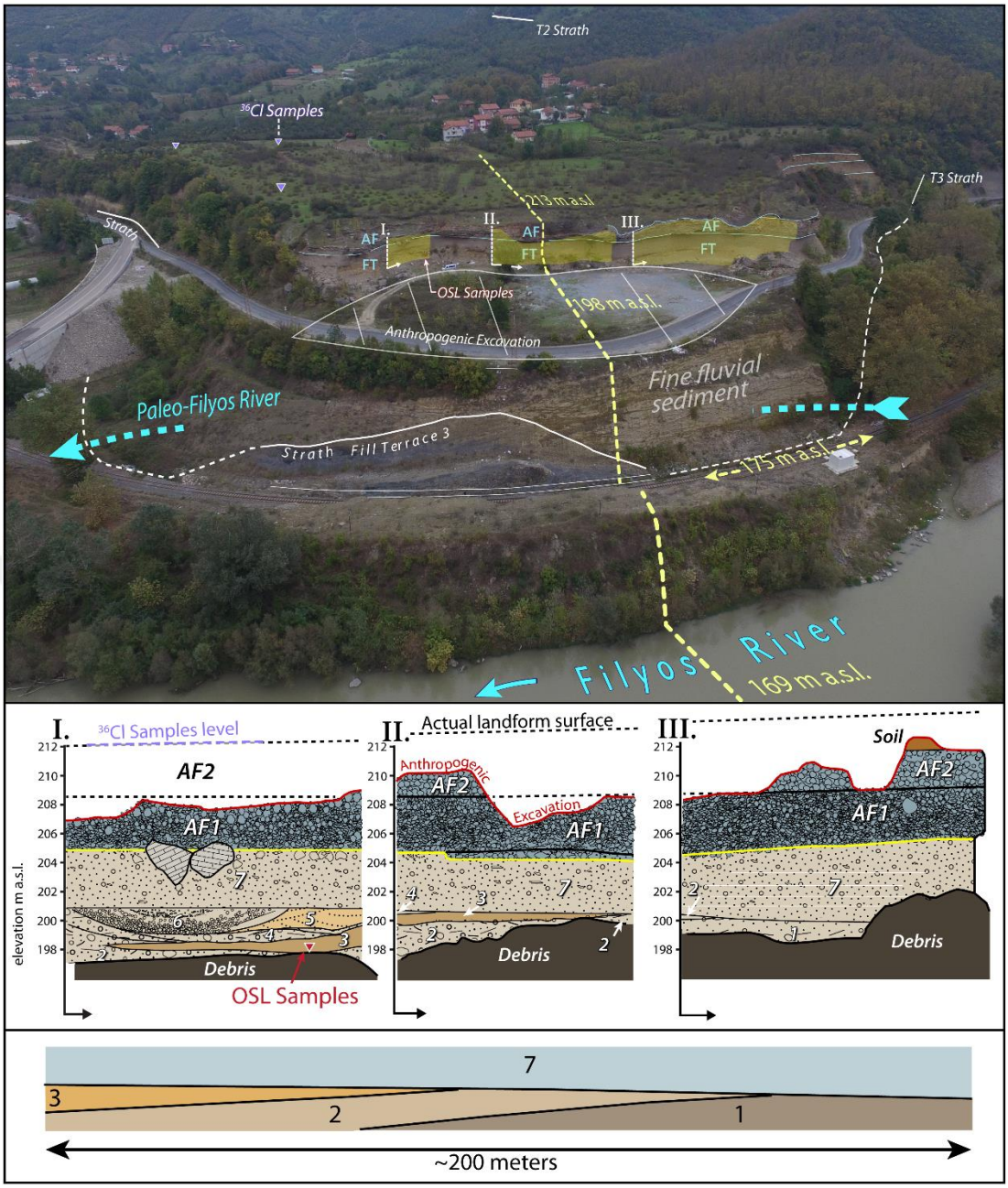

Figure 3.11 : (top) UAV view of the junction terrace, which is part of T3, the lowest level. Sample locations are labeled, the bedrock strath is marked in white, and the horizon between fluvial and alluvial fan layers is marked on the outcrop. Y-axes I, II, and II are marked at their locations and represent the axes in the middle illustration. (middle) Illustration of the exposed alluvial fan and fluvial sediments in three sections of the southern outcrop. (bottom) A simplified illustration of the orientation of layers 1, 2, 3, and 7, which correspond to the progradation of a longitudinal bar.

Table 3.4 : Descriptions and interpretations of sediment layers observed in the study area.

Layer (youngest to oldest) Terrace 3	Description	Interpretation
Lowest 15—18 m of sediment	Poor outcrop conditions showed mostly silt layers with some rounded to well-rounded gravel layers present.	Low energy, possibly floodplain. Deposition of coarser clasts may result from flow velocity increases in main channel, supply from tributary, or both.
Layer 1	Thickness unknown, only uppermost 2–3 m exposed. Rounded to sub-rounded gravel (2–5 cm) and cobbles (10–20 cm), with several cobbles 40–50 cm. Silt matrix present, but high clast density and clast support of layer.	High energy fluvial.
Layer 2	Overlaps Layer 1 at ~2–3° angle. Lowest few cm: Finer clasts at the base, all below 10 cm with almost no silt matrix. Gravel stained burnt orange overlain by gravel stained black. Above lowest cms: rounded to sub-rounded 2–5 cm gravel with sediment matrix from coarse sand to fine gravel.	High energy fluvial. Black organic matter may be remnants of a wood deposit that initiated finer central bar deposition downstream.
Layer 3 (Sampled for OSL Age: 275.6 ± 12.8 ka)	Overlaps Layer 2 at ~2–3° angle. Maximum thickness of 1 m. Thickness mostly uniform until pinching out to west. Mostly silt with some sand.	Lower-energy possibly sand to silt medial bar or longitudinal bar.
Layer 4	Thin layer of fluvial gravel similar to Layer 2 (see below).	High energy fluvial. Likely the same part of bedload from Layer 2 that shifted over the downstream side of the finer bar.
Layer 5	Maximum thickness of 2 m. Cross-bedded sand.	Low energy fluvial. Deposition of Layers 3 and 5 on the inside curve of meander (Layer 6 channel) behind a longitudinal bar, with Layers 2 and 4 being part of a coarser bedload that occasionally moved on top of finer layers.
Layer 6	Channel incision shaped layer. Base of coarse to medium, rounded to sub-rounded gravel with normal grading to fine gravel. Surfaces of fine gravel stained black.	High energy braided channel. Instead of typical east-west flow, the channel turned when it eroded into bed before depositing fluvial gravel stained in organic matter.
Layer 7	Overlies erosional boundary. Maximum 6 m thick in east, to less than 3 m thick in the west. Layer is clast-supported with horizontal bedding. From base, sub-rounded to well-rounded, average ~1 cm, well-sorted coarsening upward to average ~3 cm and less sorting near top. No cobbles in lowest half m of layer. Cobbles present and coarsening in size until reaching ~20 cm near top. Largest clasts often tabular or bladed and horizontally deposited. Top 20 cm of layer finer grain sizes similar to base of layer. Two sub-rounded to sub-angular ~2 m limestone boulders deposited near top.	Erosional base may have removed uppermost layers of bed from high velocity flow. This was followed by the latest preserved layers from this aggradational period. Braided channel transported gravel to this location. Due to rounding, it is assumed there was transport time and therefore this layer occurred upstream-downstream from here. Coarsening up represents energy increase, which brought cobbles near the top.

Table 3.4 (continued) : Descriptions and interpretations of sediment layers observed in the study area.

Layer (youngest to oldest)	Description	Interpretation
Terrace 3		
Layer AF1	Poorly sorted, with majority angular to well-rounded coarse gravels 10–30 cm and occasional cobbles and boulders. Layer entirely clast-supported with cementation of clasts. Weak horizontal bedding present.	Tributary alluvial fan remnant. Layer deposited earlier in alluvial fan development (underlying). Deposition was likely close to the main river, which may have removed finer sediments, while displacing the main river northward.
Layer AF2	Layer ~2 m thick. Poorly-sorted, angular to well-rounded clasts between cobble and boulder size (up to 3 m). Clast-supported and cemented. Some orange silt present near top, possibly associated with overlying layer of soil development.	Development of AF1 ramp allowed transportation of coarser alluvial clasts.
Terrace 2	Sediment between 30 and 80mthick. Observed outcrop started with turbidites strath tilted 30 northward (99 m above channel, 268 m a.s.l.), overlain by rounded to well-rounded, poorly-sorted, 0.25–12 cm gravel. Layer is clast-supported with silt matrix. Overlying layer of silt (matrix-supported) with clasts 0.25–7 cm mixed in. On terrace tread gravel is everywhere.	Older fluvial terrace.
Terrace 1	Tread ~350 m above river. Rounded to sub-rounded clasts on surface. Silt matrix observed in outcrops. Due to heavy vegetation, few outcrops are present and any evidence of a base (strath) is buried in vegetation.	Oldest fluvial terrace of the study area.

3.6 Terrace OSL-ages and alluvial fan cosmogenic ^{36}Cl exposure ages

The final burial dose rates for the samples were 0.49 ± 0.03 Gy/ka (Table 3.5). The luminescence ages, equivalent doses, and environmental dose rate obtained for each sample are presented in Table 3.5. Our OSL ages of three samples from a sand lens in the junction terrace (T3) yielded respective deposition ages of 256.2 ± 19.2 ka, 278.6 ± 22.1 ka, and 292.0 ± 22.2 ka.

For the alluvial fan limestone boulders on the terrace (T3) tread, spallation of ^{40}Ca was primarily responsible for ^{36}Cl production within our samples, with between 92.8 and 94.1% of production (Table 3.5). Potassium spallation contributed no more than 0.054%. The age of the channel boulder to estimate minimum inheritance was 3.85 ± 0.39 ka. A concentration of 66,792 ^{36}Cl atoms per gram of rock was measured in the channel sample. This yielded inheritance corrected exposure ages of 78.6 ± 9.5 ka, 39.5 ±3.5 ka, and 60.6 ± 6.4 ka (Figure 3.12, Table 3.5).

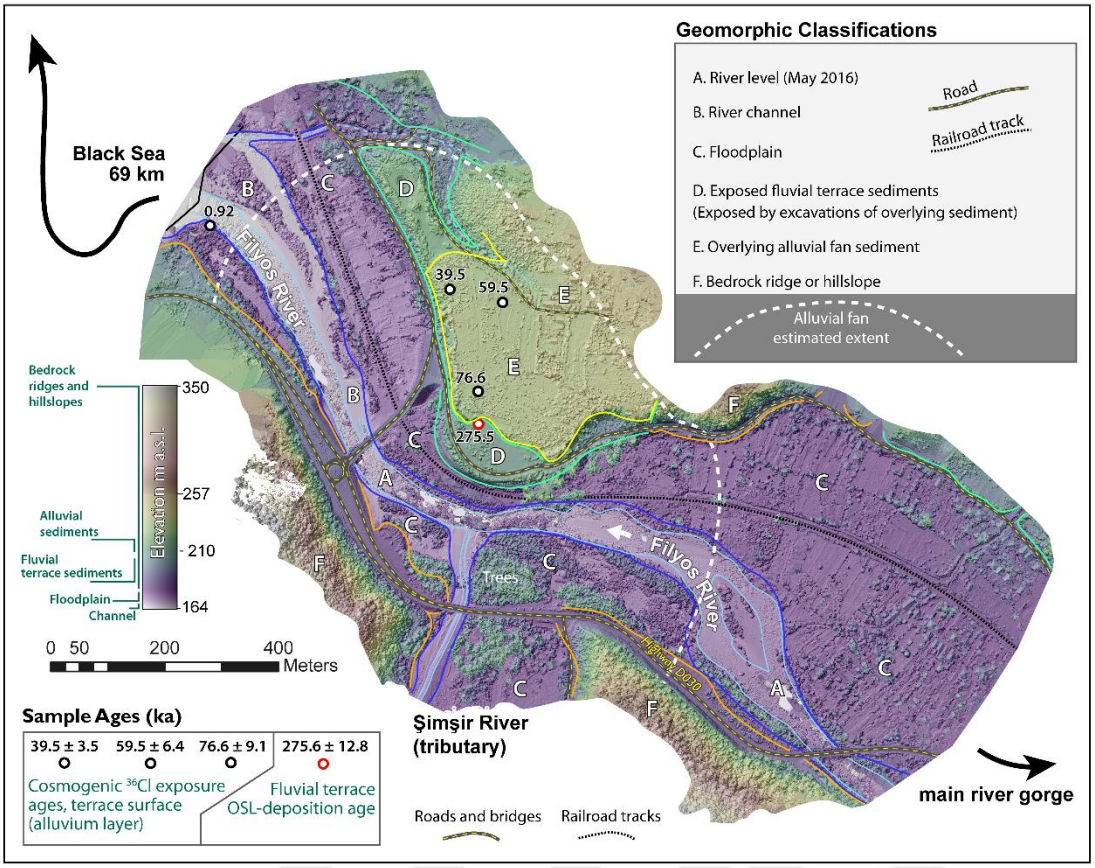

Figure 3.12 : DSM produced at the junction of the Filyos (main) and Şimşir (tributary) rivers, showing the junction terrace (T3) location and the classification of different surface features that were confirmed based on elevation and field observations. A remnant of the valley infill is preserved where labeled 'D.' While most of it eroded where there are now broad floodplains, a 1 km^2 tributary junction alluvial fan is proposed to have formed downstream (north) of the tributary canyon (Şeker Canyon) and in the main river valley. The layers from this fan are preserved where the letter 'E' is marked. Sample ages of the fluvial terrace and the overlying alluvial fan layer are in the lower left and sample locations are on the map. The channel sample in the western margin of the DSM is the inheritance correction boulder, with an age of 0.92 ± 0.1 ka.

Table 3.5 : Chemistry and ages of OSL samples (top) and ^{36}Cl samples (bottom).

OSL Samples (Latitude 41.2066, Longitude 32.3683, Elevation 198 m a.s.l.)

Terrace Level	Sample Code	Depth cm	Dose (Gy)	Dose Rate (Gy)	Cosmic Gy/ka	Water Content %	Carbonate %	U ppm	Th ppm	K %	Age (ka)
T3	OSL-01	1100	125.14 ± 4.35	0.49 ± 0.03	0.10	37.76	5.05	0.5	2.9	0.19	256.2 ± 19.2
	OSL-02	1100	135.97 ± 5.93	0.49 ± 0.03	0.10	37.76	5.05	0.5	2.9	0.19	278.6 ± 22.1
	OSL-03	1100	142.43 ± 5.24	0.49 ± 0.03	0.10	37.76	5.05	0.5	2.9	0.19	292.0 ± 22.2

OSL Average Age (ka): **275.6 ± 12.8**

Cosmogenic ^{36}Cl Exposure Samples

Terrace Level	Sample Code	Elevation (m a.s.l.)	Latitude (decimal)	Longitude (decimal)	Sample thickness (cm)	Bulk density (g/cm3)	Shielding factor	Year collected	Water content (%)
T3	Filyos 1	213	41.2073	32.3684	2.0	2.6	0.99307	2015	0.02
	Filyos 2	213	41.2089	32.3677	4.0	2.6	0.99626	2015	0.02
	Filyos 3	213	41.2087	32.3688	4.5	2.6	0.99582	2015	0.02
Modern channel	Inheritance sample	169	41.2101	32.3623	5.0	2.6	1.00000	2015	0.02

Terrace Level	Sample Code	**Age ± Total Unc. (ka)**	Internal Unc. (ka)	Erosion rate mm/ka	Measured ^{36}Cl Concentration (atoms/g)	Rock Cl Concentration (ppm)	Sample Cosmogenic ^{36}Cl (atoms/g)	Sample Radiogenic ^{36}Cl (atoms/g)
T3	Filyos 1	76.6 ± 9.1	4.1	5	1545532	34.7	1545311.18	220.82
	Filyos 2	39.5 ± 3.5	1.5	5	890601	31.2	890396.33	204.67
	Filyos 3	59.5 ± 6.4	2.9	5	1207368	24.3	1207209.90	158.09
Modern channel	Inheritance sample	0.92 0.1	0.08	5	21507	29.3	16731.72	4775.27

Terrace Level	Sample Code	Ca (%)	K (%)	Cl (%)	Ca (atoms g^{-1} a^{-1})	K (atoms g^{-1} a^{-1})	Fe (atoms g^{-1} a^{-1})	Ti (atoms g^{-1} a^{-1})	Ca (atoms g^{-1} a^{-1})	K (atoms g^{-1} a^{-1})	Cl (atoms g^{-1} a^{-1})
T3	Filyos 1	93.17	0.05354	6.77	18.779	0.010793	0.00077216	0.00025429	0.88835	0.00051012	1.4293
	Filyos 2	92.76	0.05363	7.18	18.531	0.010712	0.00065692	0.00025239	0.90006	0.00052145	1.5039
	Filyos 3	94.10	0.05417	5.84	18.408	0.010597	0.00086643	0.00024967	0.9026	0.00052086	1.1992
Modern Channel	Inheritance sample	91.07	0.06727	8.82	13.886	0.010255	0.004402	0.0019329	0.70664	0.00052427	1.4137

Terrace Level	Sample Code	Scaling method	Scalling Factors: Ca spallation	K spallation	Fe spallation	Ti spallation	Fast muons	Slow muons	Cl epithermal	Cl thermal
T3	Filyos 1	Stone et al., 2000	0.86908	0.86908	0.86908	0.86908	0.87411	0.87411	0.86908	0.86908
	Filyos 2	Stone et al., 2000	0.87451	0.87451	0.87451	0.87451	0.87746	0.87746	0.87451	0.87451
	Filyos 3	Stone et al., 2000	0.86911	0.86911	0.86911	0.86911	0.87411	0.87411	0.86911	0.86911
Modern Channel	Inheritance sample	Stone et al., 2000	0.8411	0.8411	0.8411	0.8411	0.85663	0.85663	0.8411	0.8411

Terrace Level	Sample Code	$\Sigma_{th.ss}$ (cm^2/g)	$\Sigma_{eth.ss}$ (cm^2/g)	$\Sigma_{sc.ss}$ (cm^2/g)	Q_s (unitless)	Q_{th} (unitless)	Q_{eth} (unitless)	Q_μ (unitless)
T3	Filyos 1	0.0029639	0.024953	0.12479	1.0298	1.2241	1.0788	1.0118
	Filyos 2	0.0029152	0.024908	0.12454	1.0139	1.4248	1.1305	1.0233
	Filyos 3	0.0029149	0.024902	0.12447	1.0101	1.4710	1.1402	1.0259
Modern Channel	Inheritance sample	0.0030589	0.024412	0.12163	1.0075	1.5007	1.1498	1.0291

Figure 3.13 : The west side of the south-facing junction terrace outcrop, including the longitudinal bar sand lens of the OSL samples and the fluvial gravel-alluvial fan sediment horizon. The junction terrace (T3) is part of the lowest fill terrace level. The yellow dashed line is the fluvial terrace-alluvial fan unconformity. This outcrop faces the tributary junction from the opposite side of the main river.

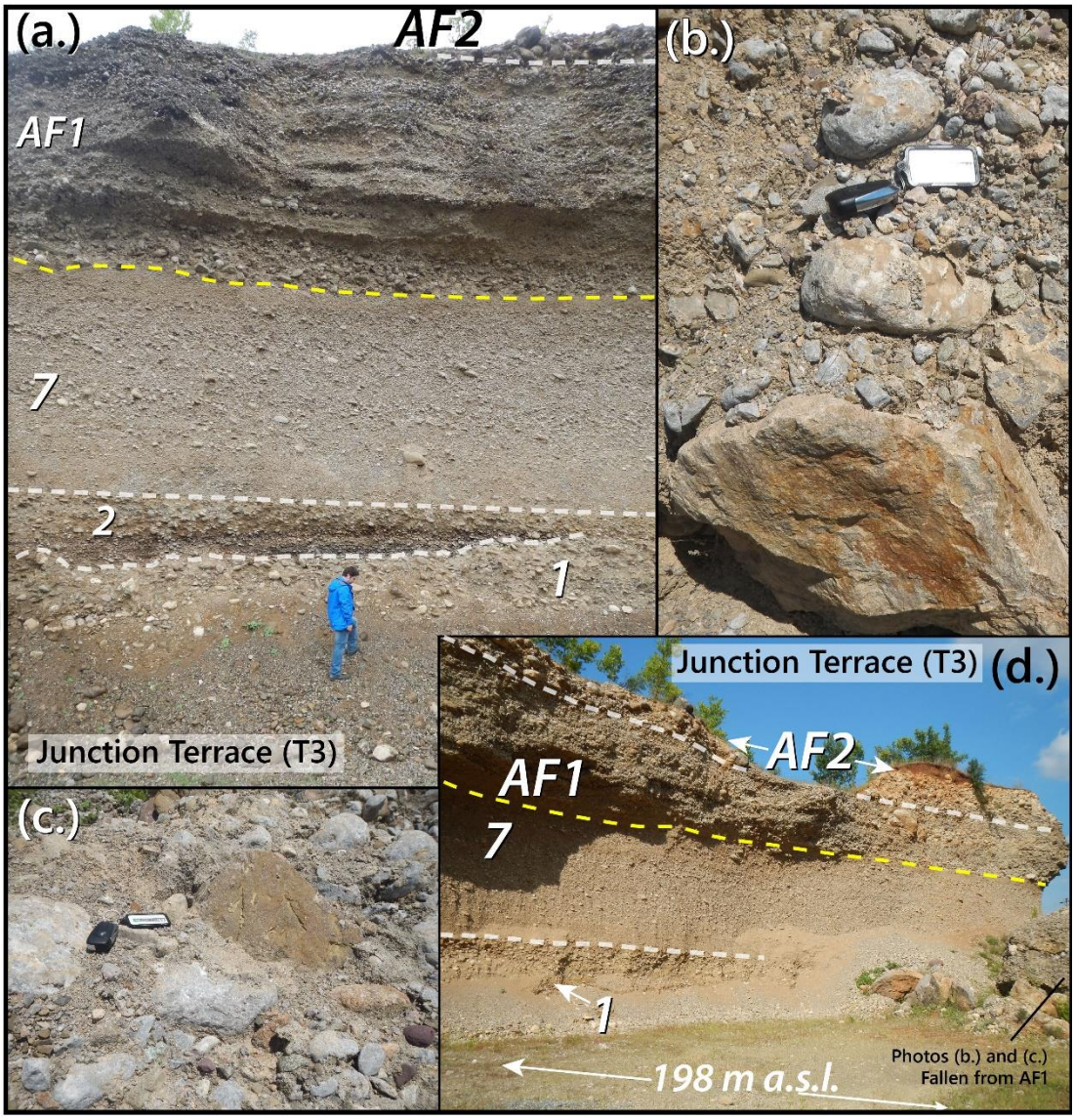

Figure 3.14 : The east side of the south-facing junction terrace outcrop, showing the layers above and below the fluvial gravel-alluvial fan sediment unconformity (yellow line). The junction terrace (T3) is part of the lowest fill terrace level. Photos B and C show close photographs of Layer AF1 that fell, located in the debris of the lower right side of Photo D. These are examples of angular clasts within the upper layers. This outcrop faces the tributary junction from the opposite side of the main river.

Figure 3.15 : Photograph of the landslide in the tributary valley that supplied the junction alluvial fan (top) (modified from Google Maps, 2020). UAV view of the tributary valley looking upstream from between the landslide and limestone tributary canyon (middle). UAV from the same location, looking downstream towards the tributary's canyon and main river valley. The tributary canyon walls are visible, with a very narrow base and widened upper sections that could be the result of a raised channel and outburst flood channel widening.

Figure 3.16 : Outcrop at the margin of the proposed landslide. (a.) Upper layer composed of angular clasts overlying fluvial sand and gravel. (b.) Closer view of the rounded gravel and sand outcrop. (c.) Close view of the sediment from photo B. Outcrop location seen in Figure 3.15b. Had a landslide dam failed, the raised channel could have deposited fluvial gravels at these levels. The absence of lateral erosion in the tributary prevents incision and deposition cycles that would preserve fluvial terraces on scales of $>10^4$ years.

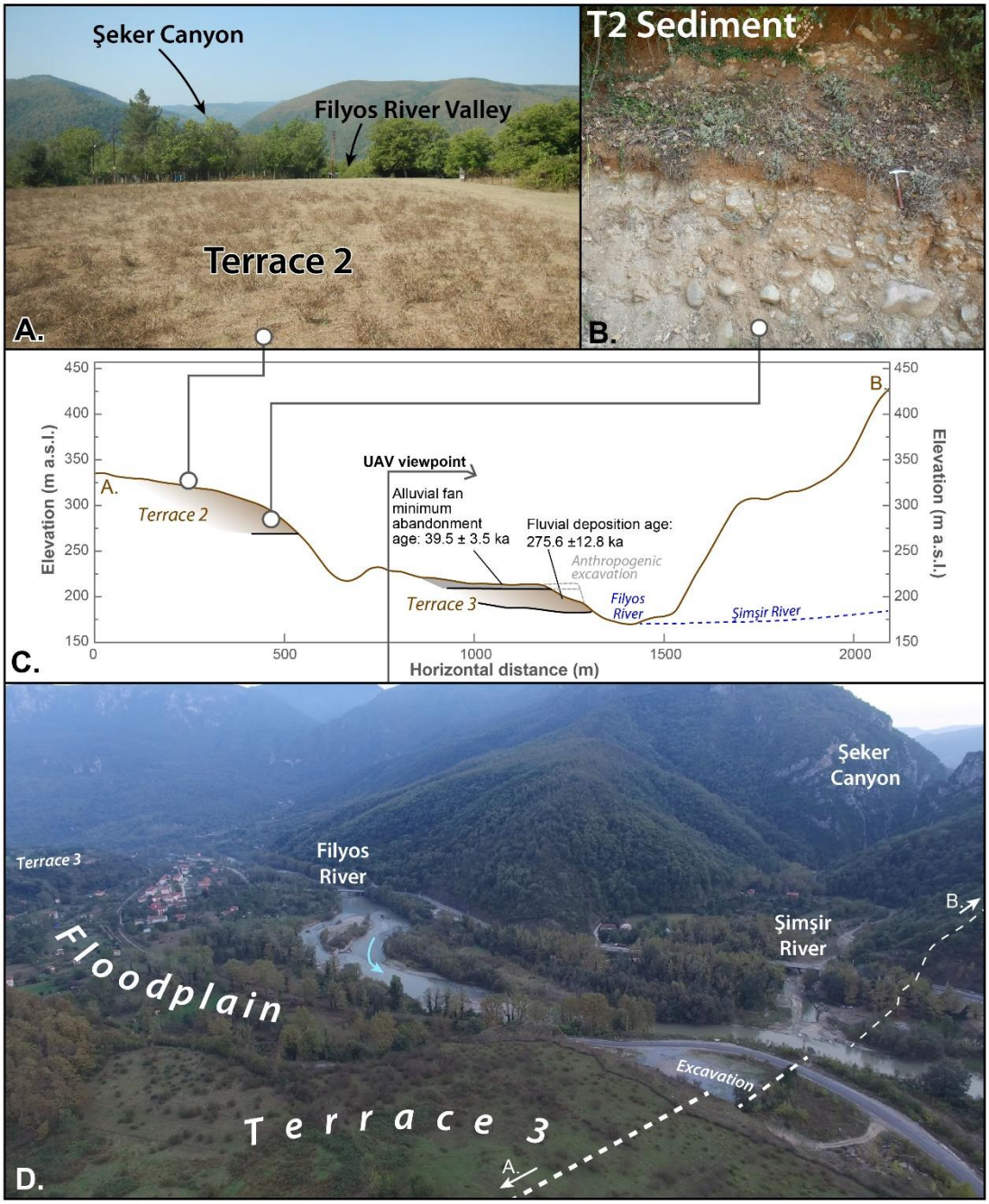

Figure 3.17 : (a.) Photograph from tread of the main river's Terrace 2, facing south towards the limestone tributary canyon. (b.) Photograph of T2's coarse fluvial sediments. These outcrops confirmed the occurrence of a fill terrace level but the clast density prevented sampling using the OSL technique. (c.)Topographic profile based on the ALOS-2 DSM (see map in Figure 3.10b), starting from bedrock ridge south of the main river, through the junction terrace (T3) and Terrace 2 on the north side of the valley. (d.) Photograph from UAV showing another angle of the main river valley facing the tributary that supplied the alluvial fan sediments. The dashed white line is part of the location of the profile in C.

4. DISCUSSION

4.1 Local Controls on Fluvial Incision, Filyos River Gorge

A dominant surface feature of the Central Pontides is landslides (Duman et al., 2005; Durutürk et al., 2017; Ercanoğlu, 2005; Ercanoğlu et al., 2016; Ercanoglu & Gokceoglu, 2002). Duman et al. (2005) and Durutürk et al. (2017) examined landslides in our study area and concluded Cretaceous flysch units such as the turbidites in the Karabük Range are especially prone to landslides. The three wind gaps adjacent to the Filyos River Valley at the start of the gorge were most likely the result of landslides that horizontally displaced the channel away from T1 (542 ± 24 ka) and T2, which are south of the modern channel. Such a scenario could be classified as an epigenetic gorge (Ouimet et al., 2008). Earthquakes are a primary cause of landslides (Adams, 1981; Fan et al., 2014; Ouimet, 2010; Ouimet et al., 2008) and sediment supply in some tectonically active regions (Ouimet, 2010; Pearce & Watson, 1986). Fan et al. (2014) demonstrated how gorge environments of plateau margins with active faults could be prone to coseismic landslide damming. An earthquake acts as a trigger, then short landslide runout distances and narrow valley width may accommodate landslide damming. While the details of timing and volume of paleo-landslide damming are beyond the scope of this study, there is a strong possibility of landslide blockages and the OSL ages reveal that the Filyos River's high stream power was sufficient to quickly remove blockages and resume vertical incision into uplifting bedrock.

4.2 Aggradational Pulses and Progressive Incision (River Junction)

The main river valley (Filyos River) is incising in response to the ongoing uplift of the Central Pontides. Hillslope processes, such as landslides, supply sediments that are transported into the main rivers and lower reaches of tributaries. Marble, limestone, and granite bedrock accommodate vertical incision and limit channel mobility in the fluvial network. Contrarily, the turbidites common in the Central Pontides permits the main rivers to laterally erode and form fluvial terraces. Upstream from the study area,

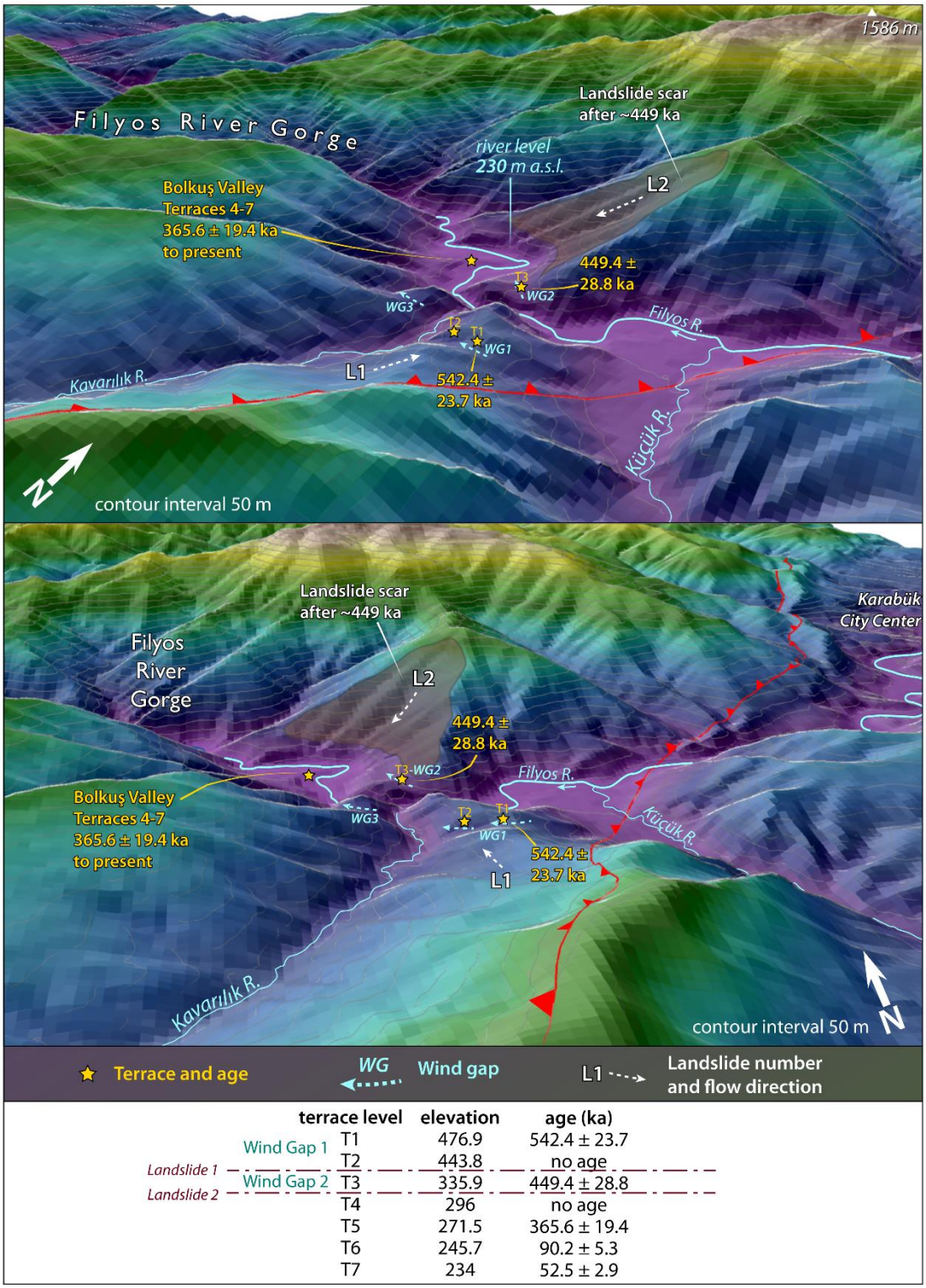

	terrace level	elevation	age (ka)
Wind Gap 1	T1	476.9	542.4 ± 23.7
	T2	443.8	no age
Landslide 1			
Wind Gap 2	T3	335.9	449.4 ± 28.8
Landslide 2			
	T4	296	no age
	T5	271.5	365.6 ± 19.4
	T6	245.7	90.2 ± 5.3
	T7	234	52.5 ± 2.9

Figure 4.1 : A three-dimensional illustration of Study Area A on the hanging wall of the Karabük Fault and entrance of the Filyos River Gorge. Here, the main river has been displaced at least twice in the last ~half million years, creating several wind gaps and an epigenetic gorge. The hanging wall surrounding the main river is mostly landslide-prone turbidites while the epigenetic gorge has vertically incised a stronger granite bedrock since forming after 449 ka.

in the upper reach of the main river gorge, the main river laterally eroded turbidites to form a strath terrace staircase. Downstream from the main river gorge, our results reveal that such laterally eroded segments of the main river valley experienced increased aggradation and multiple periods of fill terrace formations. We observederoded remnants of three fill terrace levels on the northern hillslopes of the main river valley. Short, intermittent tributaries flowing perpendicular to the trunk river have had sufficient time to erode breaks between the formerly continuous fill terrace deposits before incising vertically into the bedrock of the hillslopes. Between T2 and T3, one of these intermittent tributaries with low stream power turns and incises the bedrock in the valley flow direction between the two terrace levels (Figures 3.10b and 3.17c). Since T1 and T2 could not be sampled for ages, the geomorphological evidence can only hint at significant erosional phases between T1, T2, and T3. Our OSL-ages of a longitudinal bar within the lowest fill terrace (T3) at the tributary junction show a deposition of 275.6 ± 12.8 ka (MIS 8), which may coincide with the most recent period of high aggradation along this reach of the main valley.

Poorly-sorted and coarse sediments overlie the fluvial terrace sediments at the tributary junction but are present nowhere else. Sediment supply by the upstream landslide in the main river valley labeled ‘LB’ in Figures 1.4 and 3.10, was ruled out due to the absence of such clasts elsewhere. Instead, the large landslide located upstream from the tributary canyon, labeled ‘LA’ in Figures 1.4 and 3.10, is suspected to have supplied large sediment volumes for alluvial fan development at the tributary junction. An outcrop on the downstream margin of the landslide (Figure 3.16) shows fluvial gravel 21 to 33 m above the modern channel and it is interpreted as the deposition of fluvial sediments following the breach of the landslide dam. Interiors of most landslides are difficult to view since their sediments are only exposed after dam failure or breaching (Korup, 2013). Alluvial fans with a 3 to 5% slope may bring thousands of cubic meters of sediment, ranging from mud to boulders, to the fan area in a single event (Stock, 2013). There is a 5% slope between the outcrop of Figure 10 and the alluvial fan layers on the opposite side of the main river. The 122 km^2 tributary catchment has a high perennial streamflow with great flood potential. Therefore, the catchment is capable of transporting large volumes of sediment through the tributary canyon and onto a ~1 km^2 area at the tributary junction.

In these topographic environments of steep hillslopes, tributaries containing high episodic sediment supplies from landslides often form alluvial fans where the tributary meets the main river floodplain (Stock, 2013). Terraces in these environments may also thicken, widen, and remain more easily preserved due to sediment influx from the tributary (Pazzaglia, 2013). Meanwhile, canyons formed in tectonically thickened limestones act as barriers in their catchment, causing a decreased sediment to water ratio in tributary fans downstream from such canyons (Mather and Stokes, 2017). In the case of this study, the proximity of the main river-tributary junction to the canyon outlet prevents lateral migration of the junction during an extreme sediment flux increase, even if the water to sediment ratio is high. As the fan prograded across the main valley, it displaced the main river to the north (opposite) side of the valley and deposited alluvial fan sediments across the width of the main valley. This displacement was observed in two ways. First, alluvial fan layers reached the valley walls on the opposite side of the main river. Second, there is a river incision into only the northwestern (downstream) part of the alluvial fan sediments. This incision may be the result of a short spillway from a temporary lake on the upstream side of the fan. While evidence suggests the fan prograded across the valley, the sediments are coarser than predicted for a tributary fan downstream from a limestone canyon (i.e. Mather and Stokes, 2017). This could be explained by a large landslide blockage raising the tributary catchment elevation some tens of meters to where the canyon is wider. Ensuing outburst floods may infill bedrock gorges and rapidly increase bedrock channel widths (Korup, 2013), as seen in the upper sections of the tributary gorge in Figure 9. Our cosmogenic exposure ages suggest a minimum surface abandonment age of just 39.5 ± 3.5 ka (MIS 3), meaning this landform would have overlain a valley that was approaching its present-day morphology. Following alluvial fan erosion by the main river and tributary, the main channel and its junction returned to the southern side of the valley. This abandoned and helped preserve the alluvial fan sediments perched on the fluvial terrace tread while the rivers finished eroding and transporting the remaining alluvial fan sediments.

In brief, OSL ages reveal the main river (Filyos River) aggraded thick fill terrace deposits most recently at 275.6 ± 12.8 ka. What remained of this terrace level existed for ~235 ka until a tributary junction alluvial fan formed at the tributary junction,

overlying the fluvial terrace sediments. The dated layers were abandoned at ~39.5 ± 3.5 ka (Figures 3.17 and 4.2).

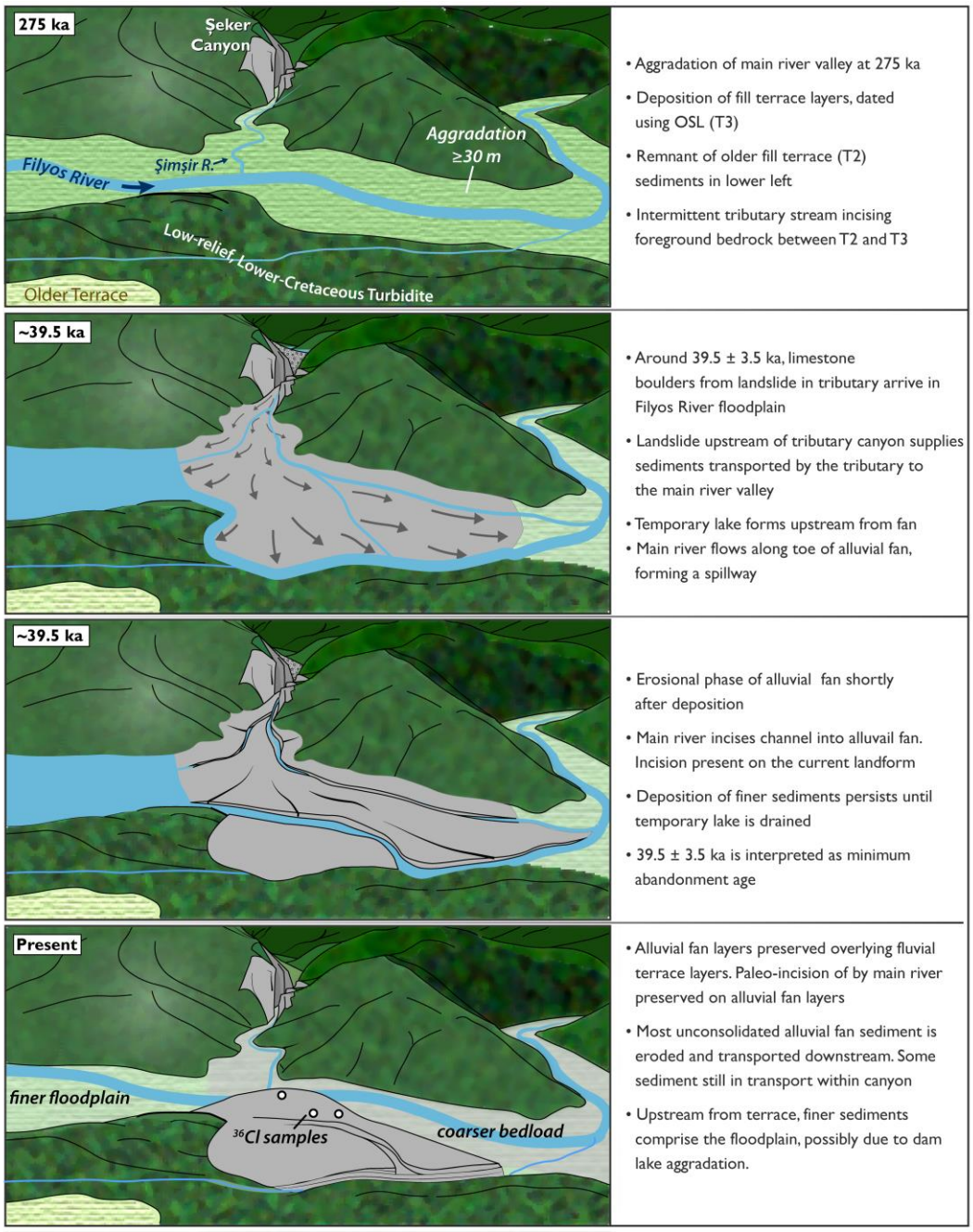

Figure 4.2 : Illustration of the model of the study environment. The illustration faces south with the main river flowing left to right and the tributary of interest in the background.

4.3 OSL-Age and Cosmogenic ^{36}Cl Exposure Age Considerations (River Junction)

For the OSL ages of three sand lens samples in the fluvial terrace, low levels of U, Th, and K were measured. Also, very low radioactive content was measured, meaning the

saturation of quartz by released electrons was slow. The final burial dose rates for the samples of 0.49 ± 0.03 Gy/ka (Table 3.5) are significantly lower than typical dose rates measurements of OSL studies. However, low dose rates have been measured in previous Central Pontides OSL studies (Yıldırım et al., 2013a; Berndt et al., 2018; McClain et al., 2020). High water and carbonate content can lead to an overestimation of the OSL age by weakening external radiation (Zander and Hilgers, 2013). While the water content was high, the carbonate content was low. Three coeval samples were used to reduce the uncertainty and potentially correct or omit outliers. The range of the three average OSL ages is within 40 ka and the uncertainties for each sample are around 20 ka. Arithmetic and weighted averages were nearly identical, but the arithmetic average produced slightly higher uncertainties. To be conservative, we reported the arithmetic average with higher uncertainties, yielding an average age of 275.6 ± 12.8 ka for the T3 fill terrace.

Meanwhile, we sampled three limestone boulders at the surface of the overlying alluvial fan layer using cosmogenic ^{36}Cl exposure dating. A modern channel boulder was sampled for inheritance, which contributed 21507 atoms/g to subtract from measured ^{36}Cl concentrations (Table 4.1). Inheritance corrections cause exposure ages to decrease by ~1 ka. However, the deposition of these alluvial fan layers is considered more complex compared to the modern channel. The inheritance boulder in the present-day main river channel is fluvial and has been in transport in the main river, not the tributary. Therefore, it may have a completely different history than the fan samples. Therefore, we chose to report exposure ages that were not corrected for inheritance.

Table 4.1: Boulder ^{36}Cl exposure ages with and without inheritance corrections and with a 5 mm/ka erosion rate and no erosion rate. Sample 'Filyos 3' is believed to be the sample that best represents the age of the alluvial fan abandonment. The calculation used to represent the minimum surface abandonment age is in bold.

Sample code	Boulder age (ka) (no inheritance correction, zero erosion)	Boulder age (ka) (no inheritance correction, 5 mm ka^{-1} erosion)	Boulder age (ka) (inheritance corrected, zero erosion)	Boulder age (ka) (inheritance corrected, 5 mm ka^{-1} erosion)	Estimated surface abandonment age (ka)
Filyos 1	62.6 ± 5.3	76.6 ± 9.1	61.7 ± 5.2	75.0 ± 8.8	
Filyos 2	36.1 ± 2.8	**39.5 ± 3.5**	35.2 ± 2.8	38.4 ± 3.4	**39.5 ± 3.5**
Filyos 3	49.6 ± 4.5	59.5 ± 6.4	48.6 ± 4.4	58.4 ± 6.3	

The part of the alluvial fan surface that was sampled was only a maximum of 10 m-thick and we have three different exposure ages with uncertainties spread over nearly

50 ka. While the alluvial fan was active long enough to obstruct the main river and create a spillway incision into the fan layers, erosional activity of the main river could not have persisted for the tens of thousands of years required to cause a differential exhumation of 50 ka. The surface was likely abandoned shortly after deposition, causing the age of 39.5 ± 3.5 ka to be the minimum surface abandonment age. The samples with older ages likely had a previous exposure history. When calculating the cosmogenic ^{36}Cl exposure ages, the parameter with the greatest influence was the erosion rate. Calculations for ^{36}Cl were performed using 0, 2.5, 5, and 10 mm/ka to see the variation (Figure 4.3, Table 4.1). The oldest boulder, which we do not believe to represent the true landform age, was the most influenced by the erosion rate while the youngest, which is more likely to represent the true landform age, had a difference of 3 ka. We reported the 5 mm/ka erosion rate, though the choice has minimal influence on the narrative.

4.4 Tectonic versus Climatic and Lithologic Controls on Incision

Hillslopes in mountainous regions are stabilized by vegetation cover during warm climatic periods. Interglacial periods may reduce the frequency of landslides and decrease the potential for valley aggradation (Maddy et al., 2001; Vandenberghe, 2003). Rivers erode their courses in vertical, lateral, and headward directions. Triggering mechanisms of these processes might be either climatic, tectonic, or both. The climatically driven incision is usually in harmony with global cycles (e.g., Milankovitch), and if cyclicity of fluvial incision is coincident with pronounced climatic cycles that would be evidence of climatic control on the fluvial incision. However, a 1 to 10 ka lag in erosional response to Milankovitch Cycle changes may be expected in rapidly uplifting areas (Braun et al., 2015). Therefore, a precise dating effort is needed for this kind of correlation. However, errors of age estimation increase with the older ages of terraces, which may not permit attributing formation to a single climatic cycle. On the other hand, tectonic processes such as rock uplift also trigger vertical incision and this usually happens randomly with respect to climatic cycles. In this context, when we look at the ages of our terraces and their correlation with glacial–interglacial cycles in the last 700 ka, we observe two clusters in the Filyos River Gorge terrace staircase of Study Area A (Figures 3.7, 3.8, and 4.5). The youngest cluster is composed of T6 and T7 terraces and the oldest cluster is comprised of T1, T3, and T5

terraces, with undated T2 and T4 a part of the older cluster. The ages of the two youngest terrace levels (T6 and T7) coincide with MIS3 and MIS5 interglacials. It is difficult to identify a climatic signal for the older T1, T3, and T5 terraces because of their large errors but if we tentatively consider their mean ages as representative ages then we can say that they are coincident with MIS 14, MIS 12, and MIS 10 glacial periods. The incision rate slope in Figure 3.8 projects interglacial periods of MIS13 and MIS11 for T2 and T4, respectively. The inconsistency makes it complicated to decide which periods (glacial or interglacial) have more influence on local terrace formation. This irregularity might be an indicator of local influences such as tectonics, which may cause steepening of hillslopes or coseismic landslides capable of damming the valley and/or changing the sediment mass balance of the fluvial system. Nevertheless, such flights of strath terraces only develop in regions where long-term pervasive uplift elevated older terraces to higher positions.

Contrary to interior parts of Anatolia, which become more arid in interglacial periods, stalagmite growth at the nearby Sofular Cave suggests increased humidity occurs here during the warming of interglacials (Göktürk et al., 2011). Downstream from the Filyos River Gorge (Study Area B), the most recent period of main river aggradation at 275 ± 12.8 ka formed a fill terrace. This occurred in the middle of a glacial period, Marine Isotope Stage MIS 8 (Figure 4.3). However, the terrace formation period follows a marine regression of some 75-100 m (Figure 4.3). While the local shoreline would move several km away from the modern shoreline, large parts of the shallow shelf of the western Black Sea would have been exposed, decreasing the availability of moisture from the westerlies. In the simplest scenario, interglacial periods would initiate incision as vegetation stabilizes hillslopes and discharge increases (Vandenberghe, 2003). However, four interglacial and three glacial periods have followed the formation of this terrace and no lower levels have been formed.

The minimum abandonment age of the tributary junction alluvial fan overlying the lowest fill terrace level occurred at ~39.5 ± 3.5 ka (Figure 4.3), which means the large landslide which supplied the tributary and main valleys with sediments occurred in the interglacial period MIS 3. This was a relatively cooler interglacial period when water intrusions into the Black Sea from the Mediterranean or Caspian Seas were disconnected (Badertscher et al., 2011). Stalagmite growth at Sofular Cave suggests this period was disconnected to the Mediterranean Sea during MIS 3 (Badertscher et

al., 2011) (Figure 4.3). This means the humid windward slopes of the study area could have been less vegetated and more easily prone to erosion and hillslope failures compared to other interglacials.

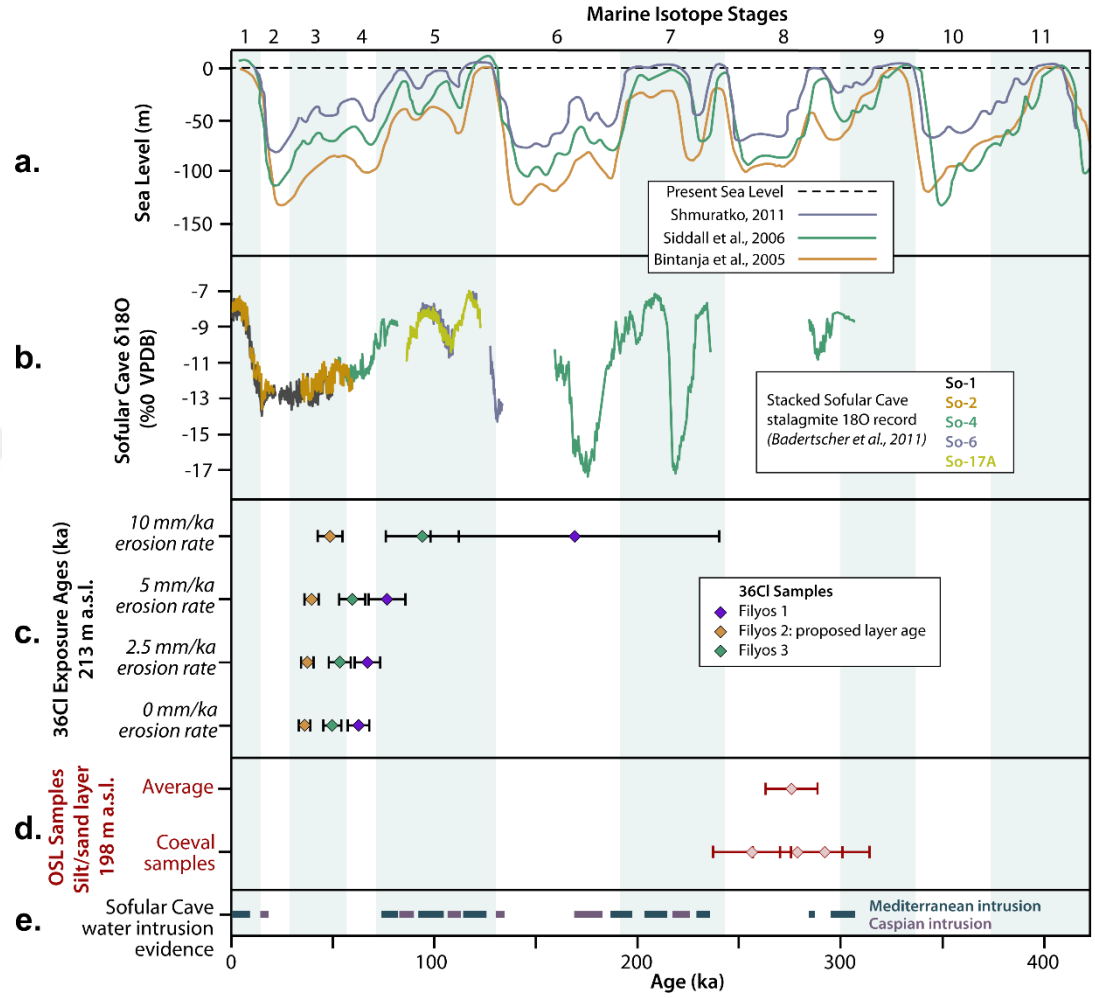

Figure 4.3 : Comparison of the Study Area B results downstream from the Filyos River Gorge with published data closer to the Black Sea from Sofular Cave and sea level curves. (a.) Sea level curves from MIS 11 through present were modified from Yıldırım et al. (2013b). Humid interglacial periods are shaded blue and their terminations are based on Lisiecki and Raymo (2005). (b.) Simplified Sofular Cave $\delta^{18}O$ stalagmite records, modified from Badertscher et al. (2011). (c.) Cosmogenic ^{36}Cl exposure ages of the limestone boulders on the junction terrace alluvial fan layer. Calculations with various erosion rates are illustrated in Section C. (d.) OSL-sample ages and uncertainties of three coeval samples and their average age from the fluvial terrace/T3 sediments. (e.) Evidence of water intrusions into the Black Sea from the Mediterranean and Caspian Seas from the nearby Sofular Cave (Badertscher et al., 2011).

If we consider patterns around the Central Pontides, fluvial landforms have a variable relationship with climate, probably due to the relationship with tectonic uplift. However, many fluvial terraces, pediment surfaces, and marine terraces formed during

MIS 5, with sediment deposition in every sampled basin. In the case of the study area, a 270 ka hiatus of terrace formations 14 km upstream ended in MIS 5. A period of frequent strath terrace formation and rapid incision ended with a fill terrace deposition. The resumption of strath terrace formation occurred ~270 ka later. The Filyos River (main river) may efficiently remove localized aggradation, such as alluvial fans or landslides, as evident in this study and McClain et al. (2020). However, there appears to be a lag between the thick aggradation of the fluvial network and subsequent incision. The relationship between lithology and lateral erosion causes limited areas for aggradation along >100 km of the main river course and even less area in some of the larger tributaries. If this is the case, then the bedrock incision into the strath in the study area may have been recent, after the alluvial fan deposition.

Lithology of bedrock hillslopes in local catchments appears to greatly influence the sediment budget of the fluvial network. Turbidites are common in the Central Pontides and are a primary lithology on the hanging wall side of the Karabük Fault. Turbidites are also recognized as the most landslide-prone lithology in northwestern Anatolia, with Mesozoic and Cenozoic units accounting for 58% of landslides (Duman et al., 2005). Landslides under forested areas of these units may be underestimated by many orders (Görüm, 2019). Contrarily, limestone is another local lithology that shows a low landslide density. While lowest order tributaries leave erosional incisions on turbidites, the limestone of the area is more resistant to such erosion. Therefore, the ratio of exposed turbidites to limestone at a given time may greatly influence the sediment budget of the fluvial network.

The study area tributary and main river have many areas with limestone-turbidites unconformities, where the differential erosion causes a gradient increase. Landslide LA is an example of the consequence of this gradient. The failure at the lithologic boundary temporarily increased the flux of limestone clasts into the fluvial system, then exposed the more erosive underlying turbidites. The landslide scar is an area that was previously a continuous limestone surface (Geologic map, Fig. 2). The catchment of the Kelemen tributary on the north side of the main river (Figs. 2 and 3) only contains turbidites. Its hillslopes are densely scared by landslides and its valley appears deeply aggraded. In addition to the sediment supply from the tributary in the south and the main river in the east, this catchment to the north also supplies an abundance of

sediment to this reach of the main river. All of the aggradation is then transported downstream through narrower valley floors.

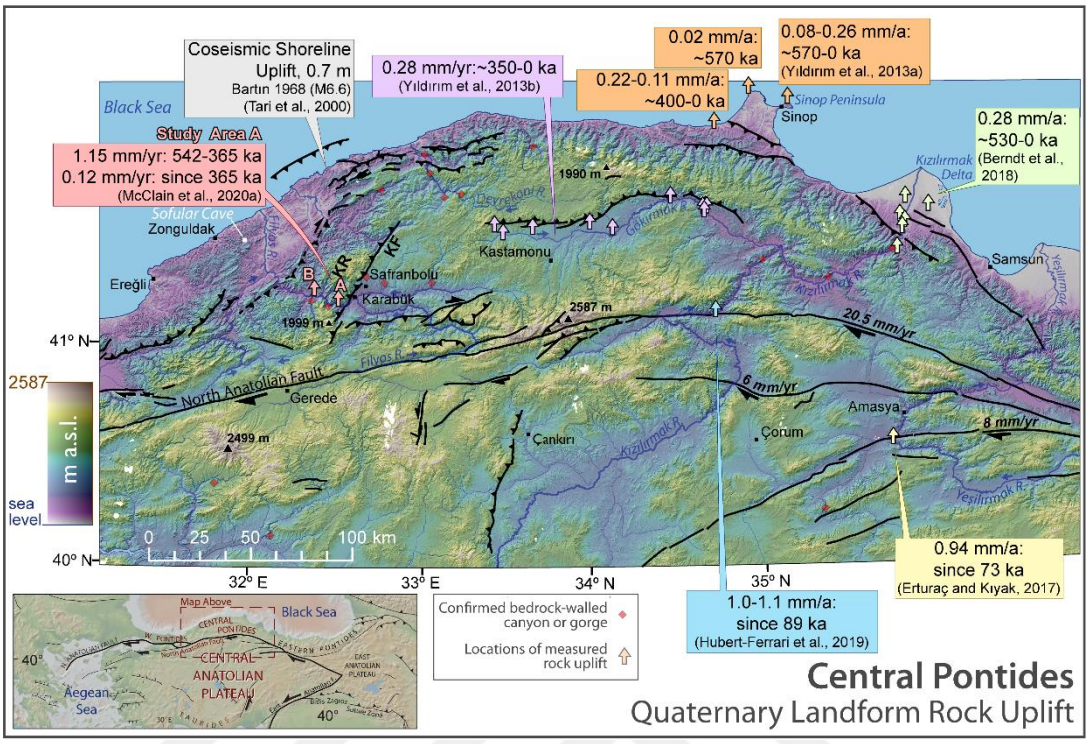

Figure 4.4 : This map of the Central Pontides illustrates the topography and major faults of the region. Dashed faults are probable or proposed faults. Sample sites of all landforms used to calculate Central Pontides Quaternary rock uplift rates are labeled with arrows. Their colors correspond to the publication and the chart in Figure 4.5. For this thesis, Study Area A yielded long-term uplift rates and is labeled 'A' on the map. Study Area B, ~15 km downstream, yielded environmental evidence that questioned whether the rock uplift decrease at 'A' was tectonic.

4.5 Downstream Aggragation Implications for Rock Uplift and Upstream Dynamics

As discussed in sections 5.1 and 5.3, the bedrock lithology causes a spatial gap between the rock uplift rates recorded at fluvial terraces 14 km upstream in the Filyos River Gorge and the terraces within this downstream study area. Despite the distance, the main river flows nearly parallel to the NAF in this reach. This means our two study areas may experience the same relationship to NAF transpression as the upstream study, where a fluvial terrace staircase recorded a non-steady rock uplift rate of 0.45 mm/a during the last 542 ka. Before 365 ka, the uplift rate measured there was 1.15 mm/a, then after 365 ka decreased to 0.12 ± 0.01 mm/a (McClain et al., 2020). Periods were measured as low as 0.07 mm/a from 52 ka until the present. The only apparent

tectonic environmental difference upstream is that the terraces formed on a reverse fault hanging wall, adjacent to the active Karabük Fault, and consequently may express

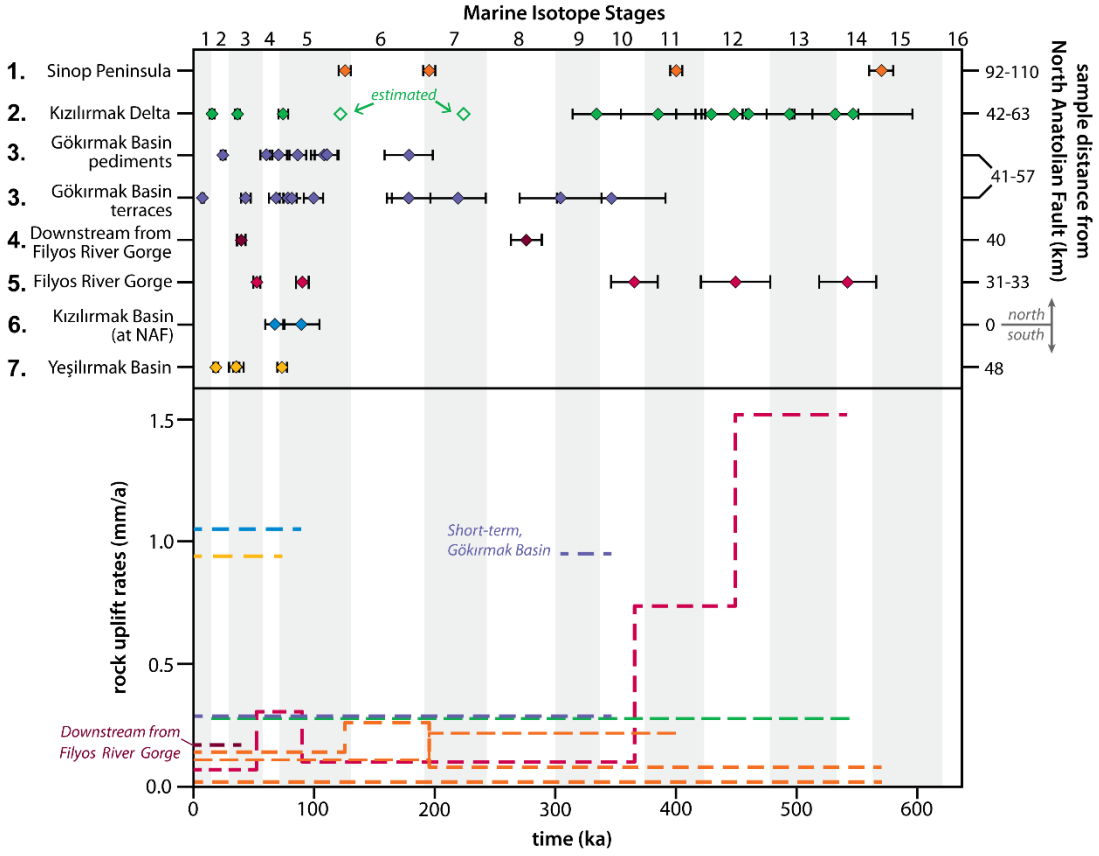

Figure 4.5 : (Top) Landform ages from different rock uplift rate studies throughout the Central Pontides. Each number corresponds to locations in Figure 4.4 and is arranged by distance from the North Anatolian Fault with number 6 located at the fault. (1.) Sinop Peninsula marine terrace ages from Yıldırım et al. (2013a). (2.) Kızılırmak Delta strath terrace, fill terrace, and delta terrace ages from Berndt et al. (2018). (3.) Gökırmak Basin strath terrace and pediment surface ages from Yıldırım et al. (2013b). (4.) Filyos River main river fill terrace and tributary junction alluvial fan ages of Study Area B. (5.) Filyos River Gorge strath terrace staircases ages from Study Area A. (6.) Kızılırmak River Valley fill terrace ages at the North Anatolian Fault in Hubert-Ferrari et al. (2019). Yeşilırmak Valley fluvial terrace ages south of the North Anatolian Fault from Erturaç and Kıyak (2017). (Bottom) Rock uplift rates through time at each study area. Colors correspond to the top section and the map in Figure 4.4. The Gökırmak Basin has a long-term uplift rate reported as 0.28 mm/a and illustrated in the chart (Yıldırım et al., 2013b). However, a higher short-term uplift rate is seen in MIS 9 and is comparable in magnitude to other studies. It is also illustrated in the chart. The Sinop Peninsula reported rock uplift rates at three locations and therefore has three orange lines representing rock uplift rates in this chart (Yıldırım et al., 2013a). MIS stage boundaries are based on Lisiecki and Raymo (2005).

additional uplift resulting from its activity. Otherwise, the model of the Central Pontides, which shows a relationship between rock uplift rate and proximity to the NAF should be the same in our study area.

A fill terrace formed upstream in the Filyos River Gorge during MIS 10 (~365 ka), followed by an incision rate decrease and hiatus in terrace formations until MIS 5 (~90 ka). Acceleration or deceleration of rock uplift rates by tectonic processes occur less rapidly than acceleration or deceleration of bedrock incision rates by climate change (Pazzaglia, 2013). These upstream incision rate variations over time might not be fully associated with a decreased tectonically-driven regional uplift but instead might be associated with aggradation upstream as well as variable downstream dynamics that derive local base-level changes. The shortage of depositional space along the main river likely increases the amount of aggradation in the wider clastic valleys where terraces form. When these areas aggrade they may form a new base-level for the next depositional environment upstream.

The complicated interaction between different surface processes, such as hillslope failures and fluvial incision/aggradation in the humid flanks of orogenic margins may increase the amount of sediment within the fluvial system, shifting it from an incisional to aggradational phase. For example, if landslide dams plug the valley or prolonged landslide activity supplies vast amounts of sediment for the fluvial system, a new local base level is formed. This new base level may be able to decrease fluvial bedrock incision rates for some period if it exists for a sufficient time. Since the Filyos River Valley is located in one of the most landslide-prone areas in Turkey (Duman et al., 2005; Durutürk et al., 2017; Ercanoğlu et al., 2016), the occurrence of such events might not be extraordinary.

Our data show aggradation at ~275 ka, which coincides with the period of low bedrock incision rates 14 km upstream and follows the formation of a fill terrace upstream ~360 ka (McClain et al., 2020). The dramatic decrease of the upstream uplift rates, from 1.15 mm/a to 0.12 mm/a after 365 ka, might be a result of a combination of aggradation followed by these kinds of downstream dynamics associated with a new base-level. When we calculate the rock uplift rate at the junction terrace we use 39.5 ka as the abandonment age of the terrace surface and 6 m of incision of bedrock below the lowest fill terrace strath. This yields an incision rate of 0.15 mm/a. If we add 2 meters to account for incised bedrock that is currently hidden below the gravel bedload, the

incision rate becomes 0.20 mm/a. Both rates exceed the rates measured upstream after 365 ka, which are a similar distance to the NAF. This is contrary to what is expected in the Central Pontides positive flower structure model proposed by Yıldırım et al. (2011), where proximity to the NAF governs rock uplift rates (Yıldırım et al., 2013 a, b; Berndt et al., 2018; McClain et al., 2020).

It is clear that this 235 ka-long aggradational period acts as a local base level upstream and the 39.5 ka to present last phase of incision has not reached 14 km upstream. While the alluvial fan deposits may only occur at this location, more widespread fluvial aggradation is required to form fill terraces. The tread of the alluvial fan deposits is 18 m lower than the modern channel 14 km upstream (230 m a.s.l.) and the fluvial deposits 24 m lower. Considering how aggradation would have likely occurred both upstream and downstream from this terrace on a scale of kilometers, the upstream aggradation could have easily influenced later (~360 ka to present) terraces of the study upstream, causing an underestimation of rock uplift rates due to the raised base level of the Filyos River.

We believe that this is an important implication not only for the Filyos River but also global incision rate estimations from river terraces. Therefore, investigation of sedimentary deposits downstream in the Filyos River Valley and other valleys may yield valuable insights that shaped the landscape or rates of bedrock incision and uplift. The prevalence of aggradation and minimal bedrock incision suggests that the fluvial system was unable to achieve states of equilibrium, making rock uplift rate estimations unattainable. This study implicates that incision rate estimations from strath terraces should be corroborated with ages and incision rates of existent downstream fill terraces, otherwise tectonic signals might be underestimated.

4.6 Implication of Spatiotemporal Uplift Rate Variations Along the Restraining Bend of the NAF

GPS-derived plate kinematic analyses of the restraining bend reveal that NAF-normal velocities vary along the strike of the restraining bend (Yıldırım et al., 2011). Higher velocities are located at the central and western sections of the restraining bend. This asymmetric pattern might also influence regional uplift rate patterns.

We evaluated this variability along the north-south and east-west trends. Uplift rates from the Sinop Peninsula (Yıldırım et al., 2013b), the Gökırmak Basin (Yıldırım et al.,

2013a), and the Kızılırmak Valley at the NAF (Hubert-Ferrari et al., 2019) provide a useful north-south section of uplift rates for comparison. Average rock uplift rates yielded from OSL ages of uplifted marine terraces since 570 ka varied between 0.02 to 0.18 mm/a in the Sinop Peninsula at the northernmost point of the central peninsula, with a short period as high as 0.26 mm/a (locations in Figures 4.4 and 4.5) (Yıldırım et al., 2013b). Cosmogenic exposure ages of strath terraces and deformed pediment surfaces suggested an average uplift rate of 0.28 ± 0.01 mm/a in the Gökırmak Basin north of the central part of the bend during the last 350 ka, with a short period as high as 0.47 mm/a (Yıldırım et al., 2013a). Recently, Hubert-Ferrari et al. (2019) found 1.0 to 1.1 mm/a incision rates on the strath terraces of the Kızılırmak River at Kamil Village (on the 1944 Rupture). These rates reveal that uplift rates are higher close to the NAF and the north–south trending uplift rate variability appears to be determined by the distance from the main strand. On the other hand, the east–west trend of the uplift rate is also variable. Average uplift rates yielded from OSL ages of uplifted delta and strath terraces in the Kızılırmak Delta (eastern flank) yielded rates of 0.28 ± 0.07 mm/a since 545 ka (Berndt et al., 2018). This rate is on the order of the average uplift rate from the Gökırmak River basin, 0.28 ± 0.01 mm/a, which is the biggest tributary of the Kızılırmak River in the Central Pontides. Our results yield an average long-term uplift rate of 0.45 ± 0.02 mm/a with a short period as high as 1.52 mm/a. There are distinct differences in rock uplift rates between the western flank and eastern flank, even though these rates are obtained from similar distances 50–60 km from the main strand. This asymmetric pattern indicates a regional influence of the restraining bend. This is because the greatest horizontal stress loads more strain on the western flank of the bend, which is comparable with plate kinematic analysis (Yıldırım et al., 2011). These rates are long-term (since middle-Pleistocene) average rates that also vary temporally, which might be an indicator of variation of the strain over time or hydrological power of the rivers associated with the changing climate or both. In the case that uplift variation is an indicator of variation of strain, with an uplift rate of 1.15 mm/a before 366 ka then 0.12 mm/a from ~366 ka until present, it seems there are similar patterns in the Central Pontides that align with the timing of the uplift rate shift. Only one location at the Sinop Peninsula shares this pattern of an uplift rate decrease. However, the decrease comes at ~190 ka (Yıldırım et al., 2013b). Because the other sample locations on the Sinop Peninsula have different uplift rate patterns, their variations may result from the activity of local faults. In the Gökırmak Basin, the

terrace ages are only dated back to ~350 ka, but the short-term uplift rate between the ~350 and 300 ka appears significantly greater than the remainder of the study. If the timing of the uplift rate decrease is aligned with the Gökırmak Basin, then this may be indicative of a decrease in strain over the central and western parts of the restraining bend. However, the likeliness of a tectonic strain decrease diminished after the results downstream from the Filyos River Gorge demonstrated that the Filyos River Valley experienced lengthy aggradational periods where bedrock incision was prevented and a new base level created. Therefore, this thesis assumes that the rock uplift rate decrease calculated at the Filyos River Gorge strath terrace staircase is underestimated after ~366 ka.

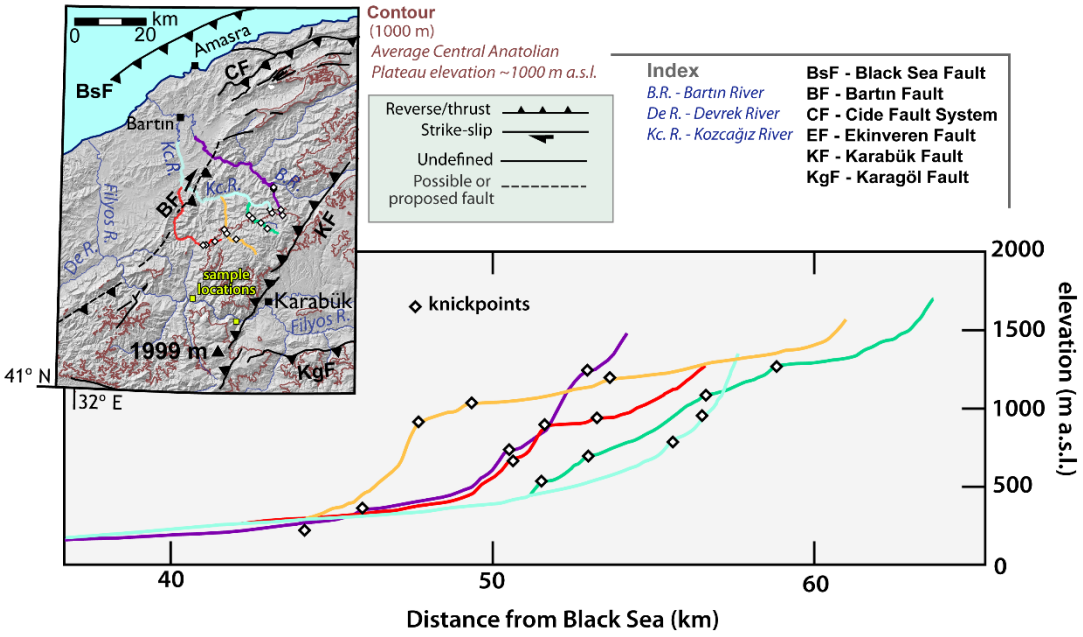

Figure 4.6 : Stream profiles on the northwest side of the Karabük Range. The yellow squares in the south part of the map show sample locations where the long-term rock uplift was calculated next to the Karabük Fault and aggradatioinal dynamics were revealed downstream to the west.

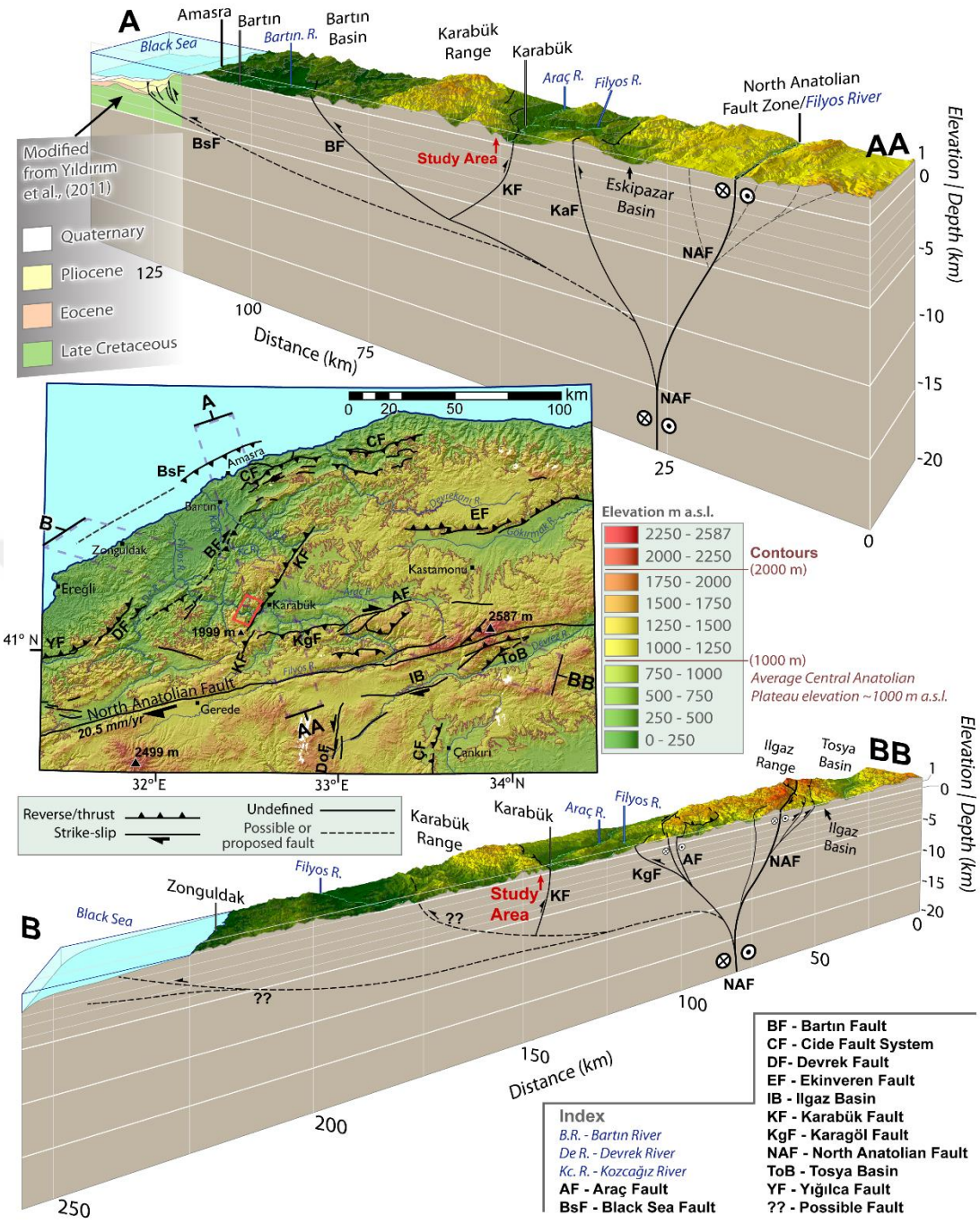

Figure 4.7 : Conceptual models for the western flank of the central Pontides. Study Area A, where long-term rock uplift rates were calculated, is in the red box on the map. The 3-D profiles of A-AA and B-BB were extracted from the ALOS-2 DSM and have a vertical exaggeration of 2. The geologic cross-section under the Black Sea in A-AA was modified from Yıldırım et al. (2011) and is based on Damcı et al. (2004). Bathymetry under B-BB is a simplified illustration.

4.7 Mode and Mechanism of Deformation

Between the NAF and the Black Sea, the Araç, Karabük, Bartın, and Cide faults are the major onshore faults across the western flank (Bengü, 2017; Ellero et al., 2015;

Emre et al., 2013; Sunal & Tüysüz, 2002; Tüysüz, 1999; Yıldırım et al., 2011). One recent development west of the Ilgaz Range has been understanding of the North Anatolian Fault as a ~30-km-wide shear zone with a positive flower structure between the Araç Fault in the north and main strand of the NAF in the south (Ellero et al., 2015). This flower structure includes a system of antithetic faults. The fault planes and projected earthquake hypocenters suggest the faults steepen and converge in the center between the NAF and the Araç Fault. The structural data from the Karabük Fault shows compressional stress in the NNW-SSE direction with a slight dextral component (Bengü, 2017). This is consistent with two offset hanging valleys in the geomorphic map of Figure 3.1 or stream numbers 12 and 13 in Figure 3.5. The Bartın Fault on the windward side of the Karabük Range, which is also antithetic of the Karabük Fault, suggests a dextral fault with a reverse component, similar to the Araç Fault (Bengü, 2017). Stream profile extractions suggest that uplift is occurring at distances north and northwest of the sample area in the Karabük Range (Figure 4.6). Furthermore, there is a presence of many knickpoints on the stream profiles and a perched landscape. Further north, the offshore seismic reflection data display north verging thrust faults deforming the abyssal plain of the Black Sea (Damcı et al., 2004) (Figure 4.7), which is comparable with the thrust faulting focal mechanism solution of the 1968 Bartın Earthquake (Mw 6.8). The NW-SE orientation of the horizontal stress axis of this focal mechanism is in harmony with the NW-SE orientation of the greatest horizontal stress driven by dextral simple shear of the NAF, revealing transpressional characteristics of the western flank. According to the active fault map of Turkey, the only onshore fault in the western flank with probable Quaternary activity is the Karabük Fault (Emre et al., 2013). Nevertheless, the presence of asymmetric ranges, linear mountain fronts, deeply incised gorges and canyons, hanging valleys, strath terraces, offset rivers, and knickpoints on the up-thrown blocks of the faults are tectono-geomorphic evidence of their Quaternary activity, even though they were inherited structures. When we consider offshore seismic reflection data, the focal mechanism solution of the Bartın Earthquake, structural data from the Karabük region (Bengü, 2017) and the North Anatolian Fault Zone (Ellero et al., 2015), and regional tectonic geomorphology, we can speculate that the positive flower structure proposed by Ellero et al. (2015) is not limited to 30 km north of the NAF but is broader as proposed by Yıldırım et al. (2011), with a western flank of the northern margin propagating northward as a growing orogenic wedge with a positive flower-structure geometry (Figure 4.7).

5. CONCLUSIONS

OSL dating of five uplifted fluvial strath terrace levels at the entrance of the Filyos River Gorge revealed a nonsteady bedrock incision rate in the Karabük Range of the Central Pontides during the last 542 ± 24 ka. A period of higher a period of higher incision rates were calculated before 366 ± 21.2 ka, where rates of 1.52 ± 0.6 then 0.74 ± 0.3 mm/a occurred. These rates are assumed to be valid and correspond to the tectonic signal. The bedrock incision of this period can be considered tectonically-driven and generated surface topography on the hanging wall of the Karabük Fault. There is a strong possibility fault activity generated major coseismic landslides. At least two major landslides in the Filyos River Gorge forced the main river to migrate, forming 2-3 wind gaps, where the oldest three terrace levels were formed and preserved. The relatively high rock uplift rates in this study appear to be a glimpse of higher-order Quaternary uplift rates within the Central Pontides due to the study location close to the North Anatolian Fault and within a subrange. Aggradation downstream revealed that the bedrock incision rates calculated in the younger terraces after 366 ± 21.2 ka may be greatly underestimated and not correspond to rock uplift rates.

Downstream from the Filyos River Gorge we investigated three fill terrace levels and mapped geomorphic features at a main river-tributary junction where alluvial fan layers were found. The 122 km^2 tributary catchment ends with a limestone canyon before its confluence with the main river. Upstream from this canyon is a large, previously unmapped landslide that has influenced the main river valley sedimentary record. We OSL-sampled the lowest fluvial fill terrace level, which yielded a deposition age of 275.6 ± 12.8 ka. Three limestone boulders of the landform tread, which were part of the alluvial fan layer, were sampled for cosmogenic ^{36}Cl exposure ages, yielding a minimum surface abandonment age of 39.5 ± 3.5 ka.

We conclude that this reach of the main river is lithologically able to accommodate lateral erosion and therefore is prone to high aggradation and fill terrace formation. On the contrary, the lithologies in the reach between the Filyos River Gorge terrace

staircase and this fill terrace area restrict lateral erosion. Landslide sediment was transported through the tributary into the main river valley, where it was deposited as an alluvial fan, ~235 ka after the fill terrace was formed. This alluvial fan reached the opposite side of the valley and caused a temporary lake upstream from the alluvial fan. Because of the high aggradation along this segment of the valley, a meaningful rock uplift rate is challenging to calculate at this location. Based on the time since the fill terrace abandonment (39.5 ka) and the 6-8 m strath above the channel, a minimum rock uplift rate was estimated between 0.15 and 0.2 mm/a. This is an important implication not only for the Filyos River but also global incision rate estimations from river terraces. Therefore, investigation of sedimentary deposits downstream in the Filyos River Valley and other valleys may yield valuable insights that shaped the landscape or rates of bedrock incision and uplift. The prevalence of aggradation and minimal bedrock incision suggests that the fluvial system was unable to achieve states of equilibrium, making meaningful rock uplift rate estimations unattainable. This study implicates that incision rate estimations from strath terraces should be corroborated with ages and incision rates of existent downstream fill terraces, otherwise tectonic signals might be underestimated.

After considering the downstream aggradation, the bedrock incision rates upstream in the Filyos River Gorge that slowed to between ~0.07 and 0.3 mm/a between 366 ± 21.2 ka and present may significantly underestimate the rock uplift rates in the Karabük Range. This means the 0.45 ± 0.02 mm/a rock uplift rate between 542 ± 24 ka and present is a minimum long term uplift rate, with a more probable rock uplift rate on the order of 1.15 mm/yr based on the pre-366 ± 21.2 ka bedrock incision rates.

Nevertheless, the results indicate that the western flank has a faster uplift rate compared to the eastern flank of the North Anatolian Fault restraining bend, implying higher loading of the transpressional strain on the western flank of the Central Pontides. This part of the western flank of the Central Pontides propagates northward as a growing orogenic wedge with a positive flower structure geometry (Figure 4.7). This supports the notion that the North Anatolian Fault is the main driving force controlling the uplift pattern of the northern margin of the Central Anatolian Plateau.

REFERENCES

Abgarmi, B., Delph, J. R., Arda Ozacar, A., Beck, S.L., Zandt, G., Sandvol, E., …Biryol, C. B. (2017). Structure of the crust and African slab beneath the central Anatolian plateau from receiver functions: New insights on isostatic compensation and slab dynamics. *Geosphere, 13,* 1774–1787. https://doi.org/10.1130/GES01509.1

Adams, J. (1981). Earthquake-dammed lakes in New Zealand. Geological Society of America, *Geology, 9,* 215–219.

Aitken, M. J. (1998). *An introduction to optical dating. The dating of Quaternary sediments by the use of photon-stimulated luminescence*. Oxford, New York, Tokyo: Oxford University press.

Akdoğan, R., Okay, A. I., Sunal, G., Tari, G., Meinhold, G., and Kylander-Clark, A. R. C. (2017). Provenance of a large Lower Cretaceous turbidite submarine fan complex on the active Laurasian margin: Central Pontides, northern Turkey. *Journal Asian Earth Science, 134,* 309–329. https://doi.org/10.1016/j.jseaes.2016.11.028

Allen, M., Jackson, J., and Walker, R. (2004). Late Cenozoic reorganization of the Arabia-Eurasia collision and the comparison of short-term and long-term deformation rates. *Tectonics 23,* https://doi.org/10.1029/2003TC001530

Anderson, R.S., and Anderson, S.P. (2010). *Geomorphology, The Mechanics and Chemistry of Landscapes.* Cambridge University Press, The Edinburgh Building, Cambridge CB2 8RU, UK.

Andrieux, J., Över, S., Poisson, A., and Bellier, O. (1995). The North Anatolian Fault zone: Distributed Neogene deformation in its northward convex part. *Tectonophysics, 243* (1–2), 135–154. https://doi.org/10.1016/0040-1951(94)00195-F

Aslan, İ., and Aksay, A. (2002). Geological Map of the Zonguldak F28 Quadrangle. Ankara, Turkey. *General Directorate of Mineral Research and Exploration (MTA).* Scale 1:25,000.

Aydar, E., Çubukçu, H. E., Şen, E., and Akın, L. (2013). Central Anatolian Plateau, Turkey: Incision and paleoaltimetry recorded from volcanic rocks. *Turkish Journal of Earth Science 22,* 739–746. https://doi.org/10.3906/yer-1211-8

Ayhan, M. E., and Koçyiğit, A. (2010). Displacements and kinematics of the February 1, 1944 Gerede earthquake (North Anatolian fault system, Turkey): Geodetic and geological constraints. *Turkish Journal of Earth Sciences, 19,* 284–311. https://doi.org/10.3906/yer-0901-17

Barka, A., and Reilinger, R. (1997). Active tectonics of the eastern Mediterranean region: Deduced from GPS, neotectonic, and seismicity data. *Annali di Geofisica, 40,* 587–610.

Bengü, E. (2017). *Post-Paleogene stress distribution in the Bartın-Ulus-Safranbolu Basins, Western Pontides, Turkey.* (Ph.D. thesis), Graduate School of Natural and Applied Sciences, Middle East Technical University.

Berndt, C., Yıldırım, C., Çiner, A., Strecker, M.R., Ertunç, G., Sarıkaya, M. A., …Kiyak, N. G. (2018). Quaternary uplift of the northern margin of the Central Anatolian Plateau: New OSL dates of fluvial and delta-terrace deposits of the Kızılırmak River, Black Sea coast, Turkey. *Quaternary Science Reviews 201,* 446–469. https://doi.org/10.1016/j.quascirev.2018.10.029

Badertscher, S., Fleitmann, D., Cheng, H., Edwards, R. L., Göktürk, O. M., Zumbühl, A., …Tüysüz, O. (2011). Pleistocene water intrusions from the Mediterranean and Caspian seas into the Black Sea. *Nature Geoscience 4,* 236–239. https://doi.org/10.1038/ngeo1106

Bartol, J., Govers, R. (2014). A single cause for uplift of the Central and Eastern Anatolian plateau? *Tectonophysics 637,* 116–136. https://doi.org/10.1016/j.tecto.2014.10.002

Bintanja, R., van de Wal, R. S. W., and Oerlemans, J. (2005). Modelled atmospheric temperatures and global sea levels over the past million years. *Nature, 437* (7055), 125–128. https://doi.org/10.1038/nature03975

Borchers, B., Marrero, S., Balco, G., Caffee, M., Goehring, B.M., Gosse, J., …Stone, J.O. (2016). Geological calibration of spallation production rates in the CRONUS-Earth project. *Quaternary Geochronology, 31,* 188-198.

Bøtter-Jensen, L. (1997). Luminescence techniques: instrumentation and methods. *Radiation Measurements, 17,* 749-768.

Braun, J., Voisin, C., Gourlan, A. T., and Chauvel, C. (2015). Erosional response of an actively uplifting mountain belt to cyclic rainfall variations. *Earth Surface Dynamics, 3* (1), 1–14. https://doi.org/10.5194/esurf-3-1-2015

Bull, W. (1991). Geomorphic response to climate change. Oxford: Oxford University Press.

Burbank, D. W., and Anderson, R. S. (2011). *Tectonic Geomorphology*. John Wiley & Sons**.**

Chen, Y., Li, S. H., and Li, B., (2012). Slip rate of the Aksay segment of Altyn Tagh Fault revealed by OSL dating of river terraces. *Quataternary Geochronology 10,* 291–299. https://doi.org/10.1016/j.quageo.2012.04.012

Cosentino, D., Schildgen, T. F., Cipollari, P., Faranda, C., Gliozzi, E., Hudáčková, N., …Strecker, M. R. (2012). Late Miocene surface uplift of the southern margin of the Central Anatolian plateau, Central Taurides, Turkey. *GSA Bulletin, 124,* 133–145. https://doi.org/10.1130/B30466.1

Çiner, A., Doğan, U., Yıldırım, C., Akçar, N., Ivy-Ochs, S., Alfimov, V., …Kubik, P. W. (2014). Quaternary uplift rates of the Central Anatolian Plateau, Turkey: insights from cosmogenic isochron-burial nuclide dating of the Kızılırmak River terraces. *Quaternary Science Reviews 107,* 81–97. https://doi.org/10.1016/j.quascirev.2014.10.007

Damcı, E., Demirbağ, E., and Sarıkavak, K. (2004). Interpretation of seismic reflection data from offshore Bartın-Amasra, paper presented at 16th International Geophysical Congress and Exhibition of Turkey, Ankara, Turkey.

Desilets, D., Zreda, M., Almasi, P. F., and Elmore, D. (2006). Determination of cosmogenic ^{36}Cl in rocks by isotope dilution: innovations, validation and error propagation. *Chem. Geol. 233,* 185–195. https://doi.org/10.1016/j.chemgeo.2006.03.001

Dewey, J. F., Hempton, M. R., Kidd, W. S. F., Saroglu, F., and Şengör, A. M. C. (1986). Shortening of continental lithosphere: The neotectonics of eastern Anatolia—A young collision zone. *Geological Society - Special Publications, 19* (1), 1–36. https://doi.org/10.1144/GSL.SP.1986.019.01.01

Dewey, J. F., and Şengör, A. M. C. (1979). Aegean and surrounding regions: Complex multiplate and continuum tectonics in a convergent zone. *GSA Bulletin, 90* (1), 84–92. https://doi.org/10.1130/0016-7606(1979)90<84:AASRCM>2.0.CO;2

Dilek, Y. (2006). Collision tectonics of the Mediterranean region: Causes and consequences. *Geological Society of America Special Paper, 409*. https://doi.org/10.1130/2006.2409(01)

Duman, T. Y., Can, T., Emre, Ö., Keçer, M., Doğan, A., Ateş, Ş., and Durmaz, S. (2005). Landslide inventory of northwestern Anatolia, Turkey. *Engineering Geology, 77,* 99–114. https://doi.org/10.1016/j.enggeo.2004.08.005

Duman, T. Y., Can, T., and Emre, O. (2011). 1:1,500,000 Scale Turkish Landslide Inventory Map. *General Directorate of Mineral Research and Explorations. Special Publications 27,* Ankara.

Durutürk, B., Demir, N., Koseoglu, I., Onal, U. B., and Ercanoglu, M. (2017). Gis-Based Determination of Landslide Properties in Regional Scale: Karabuk Province (NW Turkey). *Annals of Valahia University of Targoviste, Geographical Series, 17* (1), 37–46. https://doi.org/10.1515/avutgs-2017-0004

Ellero, E., Ottria, G., Marroni, M., Pandolfi, L., and Göncüoğlu, M. C. (2015). Analysis of the North Anatolian shear zone in central Pontides (northern Turkey): Insight for geometries and kinematics of deformation structures in a transpressional zone. *Journal of Structural Geology, 72,* 124–141. https://doi.org/10.1016/j.jsg.2014.12.003

Emre, Ö., Duman, T. Y., Özalp, S., Elmacı, H., Olgun, Ş. and Şaroğlu, Ş. (2013). Active fault map of Turkey with explanatory text, Ankara, *General Directorate of Mineral Research and Exploration, Special Publication Series-30*.

Ercanoğlu, M., and Gökçeoğlu, C. (2002). Assessment of landslide susceptibility for a landslide-prone area (north of Yenice, NW Turkey) by fuzzy approach. *Environmental Geology 41,* 720–730. https://doi.org/10.1007/s00254-001-0454-2

Ercanoglu, M. (2005). Landslide susceptibility assessment of SE Bartin (West Black Sea region, Turkey) by artificial neural networks. *Natural Hazards and Earth System Sciences, 5* (6), 979–992. https://doi.org/10.5194/nhess-5-979-2005

Ercanoğlu, M., Uçar, I., Sönmez, H., Özyurt, N.N., Dağdelenler, G., Özsayın, E., …Alkevli, T. (2016). Assessment of landslide and flood hazard potential of Yenice district (Karabük, Turkey). *International Symposium on Natural Hazards and Hazard Management,* Karabük, 2016.

Erturaç, M. K., and Kıyak, N. G. (2017). Investigating the fluvial response to late Pleistocene climate changes and vertical deformation: Yeşilırmak Terrace Staircases (central north Anatolia). *Geological Bulletin of Turkey, 60,* 615-636. https://doi.org/ 10.25288/tjb.370625

Fernández-Blanco, D., Bertotti, G., Aksu, A., and Hall, J. (2019). Monoclinal flexure of an orogenic plateau margin during subduction, south Turkey. *Basin Research, 31,* 709–727. https://doi.org/10.1111/bre.12341

Finetti, I., Bricchi, G., Del Ben, A., Pipan, M., and Xuan, Z. (1988). Geophysical study of the Black Sea. *Bollettino di Geofisica Teorica ed Applicata, XXX* (117–118), 197–324.

Fuchs, M., and Lang, A. (2009). Luminescence dating of hillslope deposits-A review. *Geomorphology, 109,* 17–26. https://doi.org/10.1016/j.geomorph.2008.08.025

Google (2020). Omr Frk 2016, retrieved from https://www.google.com.tr/maps/@41.1746907,32.3487128,3a,75y,100h,90t/data=!3m8!1e1!3m6!1sAF1QipOqgUTauzyO4szv97C3QP0Y2dIlaGHT2LZ-zg57!2e10!3e11!6shttps:%2F%2Flh5.googleusercontent.com%2Fp%2FAF1QipOqgUTauzyO4szv97C3QP0Y2dIlaGHT2LZ-zg57%3Dw203-h100-k-no-pi0-ya345-ro-0-fo100!7i7680!8i3840?hl=en

Göğüş, O. H., Pysklywec, R. N., Şengör, A. M. C., and Gün, E. (2017). Drip tectonics and the enigmatic uplift of the Central Anatolian Plateau. *Nature Communications, 8*. https://doi.org/10.1038/s41467-017-01611-3

Göktürk, O. M., Tüysüz, O., Edwards, R. L., Fleitmann, D., Badertscher, S., Kramers, J., Leuenberger, M., Cheng, H., and Fankhauser, A. (2011). Climate on the southern Black Sea coast during the Holocene: implications from the Sofular Cave record. *Quaternary Science Reviews 30,* 2433–2445. https://doi.org/10.1016/j.quascirev.2011.05.007

Görüm, T. (2019). Landslide recognition and mapping in a mixed forest environment from airborne LiDAR data. *Engineering Geology, 258*. https://doi.org/10.1016/j.enggeo.2019.105155

Hewitt, K. (1998). Catastrophic landslides and their effects on the Upper Indus streams, Karakoram Himalaya, northern Pakistan. *Geomorphology, 26*, 47–80. https://doi.org/10.1016/S0169-555X(98)00051-8

Hewitt, K. (2006). Disturbance regime landscapes: Mountain drainage systems interrupted by large rockslides. *Progress in Physical Geography, 30*, 365–393. https://doi.org/10.1191/0309133306pp486ra

Hippolyte, J. C., Espurt, N., Kaymakci, N., Sangu, E., and Müller, C. (2016). Cross-sectional anatomy and geodynamic evolution of the central Pontide orogenic belt (northern Turkey). *International Journal of Earth Sciences, 105* (1), 81–106. https://doi.org/10.1007/s00531-015-1170-6

Hubert-Ferrari, A., Drab, L., Benedetti, L., Van der Woerd, J., and Van Campenhout, J. (2019). Cosomogenic data about uplifted river terraces: implications regarding Central North Anatolian Fault segment and the Central Pontide Orogenic Wedge. *72nd Geological Congress of Turkey*, Ankara, January–February 2019.

Jackson, J., and McKenzie, D. (1984). Active tectonics of the Alpine–Himalayan Belt between western Turkey and Pakistan. *Geophysical Journal of the Royal Astronomical Society, 77*, 185–264. https://doi.org/10.1111/j.1365-246X.1984.tb01931.x

Jolivet, L., Faccenna, C., Huet, B., Labrousse, L., Le Pourhiet, L., Lacombe, O., …Driussi, O. (2013). Aegean tectonics: Strain localisation, slab tearing and trench retreat. *Tectonophysics, 597–598*, 1–33. https://doi.org/10.1016/j.tecto.2012.06.011

Kaymakçı, N., Duermeijer, C. E., Langereis, C., White, S. H., and van Diyk, P. M. (2003). Palaeomagnetic evolution of the Çankırı basin (Central Anatolia, Turkey): Implications for oroclinal bending due to indentation. *Geology Magazine, 140* (3), 343–355. https://doi.org/10.1017/S001675680300757X

Ketin, I. (1948). Über die tektonisch-mechanischen Folgerungen aus den großen anatolischen Erdbeben des letzten Dezenniums. *Geologische Rundschau, 36-36* (1), 77–83. https://doi.org/10.1007/bf01791916

Ketin, I., and Abdüsselamoğlu, S. (1969). Bartın depreminin etkileri. *Bulletin of the Geological Society of Turkey, 12* (1–2), 66–76.

Koç, A., Kaymakci, N., Van Hinsbergen, D. J. J., and Kuiper, K. F., (2017). Miocene tectonic history of the Central Tauride intramontane basins, and the paleogeographic evolution of the Central Anatolian Plateau. *Global and Planetary Change, 158*, 83–102. https://doi.org/10.1016/j.gloplacha.2017.09.001

Koçyiğit, A. (1987). Karabük-Safranbolu Tersiyer havzası kuzey kenarının stratigrafisi ve niteliği. *Türkiye Jeoloji Kurumu Bülteni, 30*, 61–69.

Korup, O. (2013). Landslides in the Fluvial System. In: Shroder, J., Wohl, E., *Treatise on Geomorphology.* Academic Press, San Diego, CA. vol. 9, Fluvial Geomorphology, 244-259.

Kuşçu, I., Parke, J. R., White, R. S., McKenzie, D., Anderson, G. A., Timothy, A., …Şengör, A.M.C. (2004). Active slumping offshore Amasra (southwest Black Sea) and its relation with regional tectonics. *Mineral Research and Exploration Bulletin, 128,* 27–47.

Leopold, L. B., Wolman, M. G., and Miller, J. P. (1964). *Fluvial Processes in Geomorphology.* W.H. Freeman and Company, San Francisco, CA, USA, 1964.

Le Pichon, X., and Angelier, J. (1979). The hellenic arc and trench system: A key to the neotectonic evolution of the eastern mediterranean area. *Tectonophysics, 60,* 1–42. https://doi.org/10.1016/0040-1951(79)90131-8

Lisiecki, L. E., and Raymo, M. E. (2005). A pliocene-Pleistocene stack of 57 globally distributed benthic δ18O records. *Paleoceanography, 20,* PA1003. doi:10.1029/2004PA001071

Maddy, D., Bridgland, D., and Westaway, R. (2001). Uplift-driven incision and climate-controlled river terrace development in the Thames Valley, UK. *Quaternary International, 79,* 23–36. https://doi.org/10.1016/S1040-6182(00)00120-8

Maddy, D., Demir, T., Bridgland, D. R., Veldkamp, A., Stemerdink, C., van der Schriek, T., and Westaway, R. (2008). The Early Pleistocene development of the Gediz River, Western Turkey: An uplift-driven, climate-controlled system? *Quaternary International, 189,* 115–128. https://doi.org/10.1016/j.quaint.2007.08.045

Marrero, S. M., Phillips, F. M., Caffee, M. W., and Gosse, J. C. (2016). CRONUS-Earth cosmogenic ^{36}Cl calibration. *Quaternary Geochronology, 31,* 199–219. https://doi.org/10.1016/j.quageo.2015.10.002

Mather, A. E., and Stokes, M. (2017). Bedrock structural control on catchment-scale connectivity and alluvial fan processes, High Atlas Mountains, Morocco. *Geological Society, London, Special Publications, 440* (1), 103-128.

McClain, K. P., Yıldırım, C., Çiner, A., Şahin, S., Sarıkaya, M. A., Özcan, O., …Öztürk, T. (2020). Quaternary rock uplift rates and their implications for the western flank of the North Anatolian Fault restraining bend; inferences from fluvial terrace ages. *Tectonics, 39,* https://doi.org/10.1029/2019TC005993

McKenzie, D. (1972). Active tectonics of the Mediterranean region. *Geophysical Journal, 30* (2), 109–185. https://doi.org/10.1111/j.1365-246X.1972.tb02351.x

McKenzie, D. (1978). Active tectonics of the Alpine-Himalaya belt: the Aegean Sea and surrounding regions. *Geophysical Journal of the Royal Astronomical Society, 55,* 217-254.

Meijers, M. J. M., Kaymakci, N., Van Hinsbergen, D. J. J., Langereis, C.G., Stephenson, R.A., and Hippolyte, J.C. (2010). Late Cretaceous to Paleocene oroclinal bending in the central Pontides (Turkey). *Tectonics, 29.* https://doi.org/10.1029/2009TC002620

Meijers, M. J. M., Brocard, G. Y., Cosca, M. A., Lüdecke, T., Teyssier, C., Whitney, D.L., and Mulch, A. (2018). Rapid late Miocene surface uplift of the Central Anatolian Plateau margin. *Earth and Planetary Science Letters, 497,* 29–41. https://doi.org/10.1016/j.epsl.2018.05.040

Merritts, D. J., Vincent, K. R., and Wohl, E. E. (1994). Long river profiles, tectonism, and eustasy: A guide to interpreting fluvial terraces. *Journal of Geophysical Research, 99* (B7), 14,031–14,050. https://doi.org/10.1029/94JB00857

Murray, A. S., and Wintle, A. G. (2000). Luminescence dating of quartz using an improved single-aliquot regenerative-dose protocol. *Radiation Measurements, 32* (1), 57–73. https://doi.org/10.1016/S1350-4487(99)00253-X

Okay, A. I., Şengör, A. M. C., and Görür, N. (1994). Kinematic history of the opening of the Black Sea and its effect on the surrounding regions. *Geology, 22* (3), 267–270. https://doi.org/10.1130/0091-7613(1994)022<0267:KHOTOO>2.3.CO;2

Okay, A. I., Satir, M., Maluski, H., Siyako, M., Monie, P., Metzger, R., and Akyüz, S. (1996). Paleo- and Neo-Tethyan events in northwest Turkey : geological and geochronological constraints. *The Tectonic History of Asia,* 420–441.

Okay, A. I., and Tüysüz, O. (1999). Tethyan sutures of northern Turkey. *Geological Society, London, Special Publications, 156* (1), 475–515. https://doi.org/10.1144/GSL.SP.1999.156.01.22

Okay, A. I., Tüysüz, O., Satir, M., Özkan-Altiner, S., Altiner, D., Sherlock, S., and Eren, R. H. (2006). Cretaceous and Triassic subduction-accretion, high-pressure-low- temperature metamorphism, and continental growth in the Central Pontides, Turkey. *GSA Bulletin, 118,* 1247–1269. https://doi.org/10.1130/B25938.1

Öğretmen, N., Cipollari, P., Frezza, V., Faranda, C., Karanika, K., Gliozzi, E., …Cosentino, D. (2018). Evidence for 1.5 km of Uplift of the Central Anatolian Plateau's Southern Margin in the Last 450 kyr and Implications for Its Multiphased Uplift History. *Tectonics, 37,* 359–390. https://doi.org/10.1002/2017TC004805

Olley, J. M., Murray, A. S., and Robert, R. G. (1996). The effects of disequilibria in the uranium and thorium decay chain on burial dose rates in fluvial sediments. *Quaternary Science Reviews, 15* (7), 751–760. https://doi.org/10.1016/0277-3791(96)00026-1

Ouimet, W. B. (2010). Landslides associated with the May 12, 2008 Wenchuan earthquake: Implications for the erosion and tectonic evolution of the Longmen Shan. *Tectonophysics, 491* (1–4), 244–252. https://doi.org/10.1016/j.tecto.2009.09.012

Ouimet, W. B., Whipple, K. X., Crosby, B. T., Johnson, J. P., and Schildgen, T. F. (2008). Epigenetic gorges in fluvial landscapes. *Earth Surface Processes and Landforms, 33* (13), 1993–2009. https://doi.org/10.1002/esp.1650

Önal, K. M., and Demirbağ, E. (2019). New evidences of compressional tectonic regime at the southern part of the western Black Sea Basin offshore Akçakoca-Cide. *Istanbul Yerbilimleri Dergisi, 30,* 25–49.

Pazzaglia, F. J. (2013). Fluvial Terraces. In: Shroder, J. (Editor in Chief), Wohl, E. (Ed.), *Treatise on Geomorphology.* Academic Press, San Diego, CA, vol. 9, Fluvial Geomorphology, pp. 379-412.

Pearce, A. J., and Watson, A. J. (1986). Effects of earthquake-induced landslides on sediment budget and transport over a 50-yr period. *Geology, 14* (1), 52–55. https://doi.org/10.1130/0091-7613(1986)14<52:EOELOS>2.0.CO;2

Phillips, F. M., Argento, D. C., Balco, G., Caffee, M. W., Clem, J., Dunai, T., …Zreda, M. G. (2016). The CRONUS-Earth project: a synthesis. *Quaternary Geochronology, 31,* 119-154.

Piper, J. D. A., Tatar, O., Gursoy, H., Koçbulut, F., and Mesci, B. L. (2006). Paleomagnetic analysis of neotectonic deformation in the Anatolian accretionary collage, Turkey. *GSA Bulletin, Special Papers, 409,* 417–439. https://doi.org/10.1130/2006.2409(20)

Platzman, E. S., Tapirdamaz, C., and Sanver, M. (1998). Neogene anticlockwise rotation of central Anatolia (Turkey): Preliminary palaeomagnetic and geochronological results. *Tectonophysics, 299,* 175–189. https://doi.org/10.1016/S0040-1951(98)00204-2

Prescott, J. R., and Hutton, J. T. (1988). Cosmic ray and gamma ray dosimetry for TL and ESR. *Nuclear Tracks and Radiation Measurements, 14* (1–2), 223–227. https://doi.org/10.1016/1359-0189(88)90069-6

Prescott, J. R., and Hutton, J. T. (1994). Cosmic ray contribution to dose rates for luminescence and ESR dating: Large depths and long-term time variations. *Radiation Measurements, 23* (2–3), 497–500. https://doi.org/10.1016/1350-4487(94)90086-8

Reid, M. R., Schleiffarth, W. K., Cosca, M. A., Delph, J. R., Blichert-Toft, J., and Cooper, K. M. (2017). Shallow melting of MORB-like mantle under hot continental lithosphere, Central Anatolia. *Geochemistry Geophysics Geosystems, 18,* 1866–1888. https://doi.org/10.1002/2016GC006772

Reilinger, R., McClusky, S.C., Oral, M.B., King, R.W., Tokoz, M.N., Barka, A.A., …Sanli, I. (1997). Global Positioning System measurments of present-day crustal movements in the Arabia-Africa-Eurasia plate collisional zone. *Journal of Geophysical Research, 102,* 9983-9999

Sarıkaya, M. A., Yıldırım, C., and Çiner, A. (2015). Late Quaternary alluvial fans of Emli Valley in the Ecemiş Fault Zone, south central Turkey: Insights from cosmogenic nuclides. *Geomorphology, 228,* 512–525. https://doi.org/10.1016/j.geomorph.2014.10.008

Savi, S., Tofelde, S., Wickert, A. D., Bufe, A., Schildgen, T. F., and Strecker, M. R. (2020). Interactions between channels and tributary alluvial fans: channel adjustments and sediment-signal propagation. *Earth Surface Dynamics, 8,* 303-322. https://doi.org/10.5194/esurf-8-303-2020

Schildgen, T. F., Cosentino, D., Niedermann, S., Wittmann, H., Bookhagen, B., Yıldırım, C., …Strecker, M. R. (2012a). Multi-phased uplift of the southern margin of the Central Anatolian plateau, Turkey: A record of tectonic and upper mantle processes. *Earth and Planetary Science Letters, 317–318,* 85–95. https://doi.org/10.1016/j.epsl.2011.12.003

Schildgen, T. F., Cosentino, D., Caruso, A., Buchwaldt, R., Yıldırım, C., Bowring, S. A., Rojay, B., …Strecker, M.R. (2012b). Surface expression of eastern Mediterranean slab dynamics: Neogene topographic and structural evolution of the southwest margin of the Central Anatolian Plateau, Turkey. *Tectonics, 31*. https://doi.org/10.1029/2011TC003021

Schildgen, T. F., Yildirim, C., Cosentino, D., and Strecker, M. R. (2014). Linking slab break-off, Hellenic trench retreat, and uplift of the Central and Eastern Anatolian plateaus. *Earth-Science Reviews, 128,* 147–168. https://doi.org/10.1016/j.earscirev.2013.11.006

Schlagenhauf, A., Gaudemer, Y., Benedetti, L., Manighetti, I., Palumbo, L., Schimmelpfennig, I., …Pou, K. (2010). Using in situ Chlorine-36 cosmonuclide to recover past earthquake histories on limestone normal fault scarps: A reappraisal of methodology and interpretations. *Geophysical Journal International, 182,* 36–72. https://doi.org/10.1111/j.1365-246X.2010.04622.x

Shmuratko, V. I. (2001). Gravity-resonance Exotectonic *(Gravitatsiono-rezonansnaiia ekzotektonika).* Astroprint, Odessa (in Russian).

Siddall, M., Chappell, J., and Potter, E. K. (2006). Eustatic sea level during past interglacials. *Developments in Quaternary Science, January 2007,* 75-92. doi: 10.1016/S1571-0866(07)80032-7

Sosson, M., Kaymakci, N., Stephenson, R., Bergerat, F., and Starostenko, V. (2010). Sedimentary basin tectonics from the Black Sea and Caucasus to the Arabian Platform: introduction. *Geological Society of London, Special Publications, 340,* 1–10. https://doi.org/10.1144/sp340.1

Stock, J. D., (2013). Waters Divided: A History of Alluvial Fan Research and a View of Its Future, *Treatise on Geomorphology.* Elsevier Ltd. https://doi.org/10.1016/B978-0-12-374739-6.00249-9

Stokes, M., and Mather, A. E. (2015). Controls on modern tributary-junction alluvial fan occurrence and morphology: High Atlas Mountains, Morocco. *Geomorphology, 248,* 344–362. https://doi.org/10.1016/j.geomorph.2015.08.003

Stokes, M., Mather, A. E., Belfoul, M., Faik, F., Bouzid, S., Geach, M. R., …Thiel, C. (2017). Controls on dryland mountain landscape development along the NW Saharan desert margin: Insights from Quaternary river terrace sequences (Dadès River, south-central High Atlas, Morocco). *Quaternary Science Reviews, 166,* 363–379. https://doi.org/10.1016/j.quascirev.2017.04.017

Stone, J. O. (2000). Air pressure and cosmogenic isotope production. *Journal of Geophysical Research, 105* (B10). doi:10.1029/2000JB900181

Sunal, G., and Tüysüz, O. (2002). Palaeostress analysis of tertiary post-collisional structures in the Western Pontides, northern Turkey. *Geological Magazine, 139* (3), 343–359. https://doi.org/10.1017/S0016756802006489

Şengör, A. M. C., Grall, C., İmren, C., Le Pichon, X., Görür, N., Henry, P., …Siyako, M. (2012). The geometry of the North Anatolian transform fault in the sea of Marmara and its temporal evolution: Implications for the development of intracontinental transform faults. *Canadian Journal of Earth Sciences, 51,* 222–242.

Şengör, A. M. C., and Kidd, W. S. F. (1979). Post-collisional tectonics of the Turkish-Iranian plateau and a comparison with Tibet. *Tectonophysics, 55* (3-4), 361–376. https://doi.org/10.1016/0040-1951(79)90184-7

Şengör, A. M. C., Özeren, S., Genç, T., and Zor, E. (2003). East Anatolian High Plateau as a mantle-supported, north-south shortened domal structure. *Geophysical Research Letters, 30,* 2–5. https://doi.org/10.1029/2003GL017858

Şengör, A. M. C., Tüysüz, O., İmren, C., Sakınç, M., Eyidoğan, H., Görür, N., …Rangin, Claude. (2005). The North Anatolian fault: A new look. *Annual Reviews Earth Planetary Science, 33* (1), 37–112. https://doi.org/10.1146/annurev.earth.32.101802.120415

Şengör, A. M. C., and Yılmaz, Y. (1981). Tethyan evolution of Turkey: A plate tectonic approach. *Tectonophysics, 75* (3–4), 181–241. https://doi.org/10.1016/0040-1951(81)90275-4

Tari, E., Sahin, M., Barka, A., Reilinger, R., King, R. W., McClusky, S., and Prilepin, M. (2000). Active tectonics of the Black Sea with GPS. *Earth, Planets and Space, 52* (10), 747–751. https://doi.org/10.1186/BF03352276

Timur, E., and Aksay, A. (2002). Geological map of the Zonguldak F29 quadrangle. Ankara, *Turkey General Directorate of Mineral Research and Exploration (MTA),* Ankara, Turkey, 2002. Scale 1:25,000.

Tüysüz, O. (1999). Geology of the Cretaceous sedimentary basins of the Western Pontides. *Geological Journal, 34* (1–2), 75–93. https://doi.org/10.1002/(SICI)1099-1034(199901/06)34:1/2<75::AID-GJ815>3.0.CO;2-S

Url-1 <*http://www.cronuscalculators.nmt.edu*>, date retrieved 29.06.2020.

Vandenberghe, J. (2003). Climate forcing of fluvial system development: An evolution of ideas. *Quaternary Science Reviews, 22,* 2053–2060. https://doi.org/10.1016/S0277-3791(03)00213-0

Wedding, H. (1969). 3 Eylül 1968'de Vukua gelen Bartın-Amasra yer sarsıntısı. *MTA Dergisi, 71,* 135–140.

Whittaker, A. C., Attal, M., Cowie, P. A., Tucker, G. E., and Roberts, G. (2008). Decoding temporal and spatial patterns of fault uplift using transient

river long profiles. *Geomorphology, 100* (3–4), 506–526. https://doi.org/10.1016/j.geomorph.2008.01.018

Wortel, M. J. R., and Spakman, W. (2000). Subduction and Slab Detachment in the Mediterranean-Carpathian Region. *Science's Compass Review, Geophysics, 290,* 1910-1917. doi: 10.1126/science.290.5498.1910

Yıldırım, C., Schildgen, T. F., Echtler, H., Melnick, D., Bookhagen, B., Çiner, A., …Strecker, M. R. (2013b). Tectonic implications of fluvial incision and pediment deformation at the northern margin of the Central Anatolian Plateau based on multiple cosmogenic nuclides. *Tectonics, 32,* 1107–1120. https://doi.org/10.1002/tect.20066

Yıldırım, C., Schildgen, T. F., Kıyak, N. G., Ballato, P., Melnick, D., Erginal, A. E., …Echtler, H. (2013a). Differential uplift along the northern margin of the Central Anatolian Plateau: inferences from marine terraces. *Quaternary Science Reviews, 81,* 12–28. https://doi.org/10.1016/j.quascirev.2013.09.011

Yıldırım, C., Schildgen, T. F., Echtler, H., Melnick, D., and Strecker, M. R. (2011). Late Neogene and active orogenic uplift in the Central Pontides associated with the North Anatolian Fault: Implications for the northern margin of the Central Anatolian Plateau, Turkey. *Tectonics, 30,* 1–24. https://doi.org/10.1029/2010TC002756

Yılmaz, Y., Tüysüz, O., Yiğitbaş, E., Genç, Ş. C., and Şengör, A. M. C. (1997). Geology and Tectonic Evolution of the Pontides. A.G. Robinson, ed., *Regional and petroleum geology of the Black Sea and surrounding region: AAPG Memoir 68,* 183-226

Zander, A., and Hilgers, A. (2013). Potential and limits of OSL, TT-OSL, IRSL and pIRIR290 dating methods applied on a Middle Pleistocene sediment record of Lake El'gygytgyn, Russia. *Climate of the Past, 9,* 719–733. https://doi.org/10.5194/cp-9-719-2013

CURRICULUM VITAE

Name Surname **:** Kevin Patrick MCCLAİN

Place and Date of Birth **:**

EDUCATION **:**

- **B.Sc.** **:** 2009, University of Oregon, Geography and GIS
- **M.Sc.** **:** 2014, Uppsala University, Earth Science

PUBLICATIONS, PRESENTATIONS AND PATENTS ON THE THESIS:

- **McClain, K. P.**, Yıldırım, C., Çiner, A., Şahin, S., Sarıkaya, M. A., Özcan, O., … Öztürk, T., 2020. Quaternary Rock Uplift Rates and Their Implications for the Western Flank of the North Anatolian Fault Restraining Bend; Inferences From Fluvial Terrace Ages. Tectonics, 39. DOI: 10.1029/2019TC005993
- **McClain, K. P**., Yıldırım, C., Çiner, A., Şahin, S., Sarıkaya, M. A., Özcan, O., … Öztürk, T., 2021. River, alluvial fan and landslide interactions in a tributary junction setting: implications for tectonic controls on Quaternary fluvial landscape development (Central Anatolian Plateau northern margin, Turkey). Geomorphology, 376. DOI: 10.1016/j.geomorph.2020.107567

OTHER PUBLICATIONS, PRESENTATIONS AND PATENTS:

- **McClain, K. P**., Yıldırım, C., Çiner, A., Şahin, S., Sarıkaya, M. A., Kıyak, N. G., Öztürk, T., (2015). Quantifying Fluvial Response to Tectonic Deformation and Climate, Central Pontides, Anatolian pLateau climate and Tectonic hazards (ALErT) Midterm Review Meeting
- **McClain, K. P**., Yıldırım, C., Çiner, A., Şahin, S., Sarıkaya, M. A., Özcan, O., Kıyak, N. G., Öztürk, T., 2016, Quantification of Fluvial Response to Tectonic Deformation and Climate Change in the Central Pontides; Inferences from OSL Dating of Fluvial Terraces, IPGP Doctoral Congress, Paris, France

- **McClain, K. P**., Yıldırım, C., Çiner, A., Şahin, S., Sarıkaya, M. A., Kıyak, N. G., Öztürk, T., 2016, ORTA PONTİDLER'DE AKARSULARIN TEKTONİK DEFORMASYON VE İKLİM DEĞİŞİMİNE TEPKİSİNİN DEĞERLENDİRİLMESİ; AKARSU SEKİLERİNİN OSL İLE YAŞLANDIRILMASINDAN ÇIKARIMLAR, 69. TÜRKİYE JEOLOJİ KURULTAYI, Ankara, Turkey
- **McClain, K.P**., Yıldırım, C., Çiner, A., Şahin, S., Sarıkaya, M. A., Kıyak, N. G., Öztürk, T., 2016, Quantification of fluvial response to tectonic deformation and climate change in the northern margin of the Central Anatolian Plateau; inferences from OSL dating of fluvial terraces, TURQUA 2016, Istanbul, Turkey
- **McClain, K. P**., Yıldırım, C., Çiner, A., Şahin, S., Sarıkaya, M. A., Kıyak, N. G., Öztürk, T., 2016, Quantification of fluvial response to tectonic deformation and climate in the Central Pontides, Turkey; inferences from OSL dating of fluvial terraces, American Geophysical Union Fall Meeting, San Francisco, CA, United States
- **McClain, K. P**., Yıldırım, C., Çiner, A., Şahin, S., Sarıkaya, M. A., Özcan, O., Kıyak, N. G., Öztürk, T., 2017, Quantification of fluvial response to tectonic deformation in the Central Pontides, Turkey; inferences from OSL dating of fluvial terraces, European Geosciences Union Spring Meeting, Vienna, Austria
- **McClain, K. P**., Yıldırım, C., Çiner, A., Şahin, S., Sarıkaya, M. A., Özcan, O., Kıyak, N. G., Öztürk, T., 2017, Quantification of fluvial response to tectonic deformation and climate in the Central Pontides, Turkey; inferences from OSL-dating of fluvial terraces, Anatolian pLateau climate and Tectonic hazards (ALErT) Closing Meeting, Bratislava, Slovakia
- **McClain, K. P**., Yıldırım, C., Çiner, A., Şahin, S., Sarıkaya, M. A., Özcan, O., Kıyak, N. G., Öztürk, T., 2018, Quantifying fluvial response to tectonic deformation and climate in the Central Pontides, Turkey; inferences from OSL-dating of fluvial terraces (updated results and interpretations), TURQUA, Istanbul, Turkey
- **McClain, K. P.**, Yıldırım, C., Çiner, A., Şahin, S., Sarıkaya, M. A., Özcan, O., Kıyak, N. G., Öztürk, T., 2019, Fluvial response to tectonic deformation in the western flank of the Turkish Central Pontides; inferences from OSL-ages, 72. TÜRKİYE JEOLOJİ KURULTAYI, Ankara, Turkey